Geomechanical Modeling Using A Damped Finite Difference Method And Seismic Imaging Using Secondary Scattered Waves

by
Rongrong Lin

A dissertation submitted to the Department of Earth and Atmospheric Sciences,
College of Natural Sciences and Mathematics
in partial fulfillment of the requirements for the degree of

DOCTOR OF PHILOSOPHY

in Geophysics

Chair of Committee: Yingcai Zheng

Committee Member: Robert Stewart

Committee Member: Aibing Li

Committee Member: Leon Thomsen

Committee Member: Xinding Fang

Committee Member: Haibin Xu

University of Houston
December 2020

ACKNOWLEDGMENTS

I am deeply grateful to Prof. Yingcai Zheng who is my advisor and Chairman of the committee. From him, I not only learned a wide spectrum of geophysical concepts and methods but also grasped important technical writing and communication skills which profoundly benefited me during my graduate study and prepared me better for my career in the future. His generous support and giving me the opportunity to participate in the DOE project is the key that I could finish this dissertation. He also recommended me for various valuable opportunities such as the company internships and the postdoc positions. I feel extremely lucky to have such an opportunity to work with him.

I would particularly like to thank my co-advisor, Prof. Leon Thomsen, who is one of the greatest geophysicists and has been generously helping me for almost ten years since my master's degree. My published SEG expanded abstract mentored by him on the methodology of extracting anisotropy parameters from seismic and well log information is by far my most cited paper and one of the proudest achievements of mine. My weekly Friday research progress meeting with him brings me insightful ideas into my research and many sections in this dissertation benefited from his bright minds.

I also want to express my sincere gratitude to Prof. Xinding Fang, who took me as a visiting student at SUSTech when I had a visa problem was stuck in China for many months. I received generous support from him and his students during my temporary stay. Without him, I could not possibly be able to learn the technique of efficient finite difference method in a short amount of time to initiate the research of this dissertation.

I would like to show my great appreciation to Prof. Aibing Li, who has been helping me since I started pursuing my master's degree at the University of Houston. As the department graduate advisor, she kindly and patiently answered my emails even before I formally enrolled in the graduate study. Her seismic inversion class built a solid foundation for my research and the discussion with her inspired me to try viscous attenuation instead of constant damping for my damped finite difference method in the dissertation.

My sincerest appreciation goes to Prof. Robert Stewart, who served on both my master's and Ph.D. committees. I gained a once in a lifetime experience in his acquisition class in which he took us to the field and show us how to do acquisition step by step. This broadened my horizon and further excited my interests in geophysics. He is smart with many bright ideas and the chapter in the dissertation that compares the finite difference and the finite element method on geomechanical modeling is inspired by him.

I am indebted to Dr. Haibin Xu from Shell as my external committee member. Dr. Xu is always very supportive and responsive. He took his valuable time and pointed me to the digital rock research. He also kindly answered my career questions and gave me constructive comments and warm encouragement.

I would like to give my greatest appreciation to my colleagues and friends in the EAS department of the University of Houston. Dr. Hao Hu generously helped me revise the paper and provided me useful codes for geophysical computation and visualization. Dr. Sharon Cornelius not only gave me insightful geophysical comments but also helped me in many aspects of life. Dr.

Jinny Sisson is very kind and supportive as the department supervisor of teaching assistants and made me enjoy working as a teaching assistant during my graduate study.

I would like to offer my special thanks to my colleagues and friends at work. My colleagues and friends in PGS whom I had met during my first geophysical internship in my Ph.D. study, were friendly and gave me many suggestions for my geophysical research. Before I became a Ph.D. student, Dr. Janusz Peron, my advisor in Halliburton when I participated in the part-time Ph.D. program, encouraged me to pursue a higher degree in my career.

Without the support and encouragement from my family, my Ph.D. study will not be possible. Special thanks go to my husband Dr. Chen Qi for both his professional advice and emotional support.

During my years of geophysics study and work, I experienced ups and downs in the oil and gas industry, let alone the current pandemic. There were times when I was anxious and confused about my future career. The encouragement and advice from my committee members and friends always reassured my faith and kept me on track of my career path.

Most of the chapters in this dissertation are from my publications, some of which are modified and expanded. Section 1.1 in Chapter 1, Chapter 2, Sections 3.1-3.4 in Chapter 3, Sections 4.2-4.3 in Chapter 4, and Section 5.1 in Chapter 5 are from my publication in the journal Pure and Applied Geophysics (Lin et al., 2019). Section 4.4 is from my publication in the journal Minerals (Lin and Thomsen, 2019). I am grateful for permission from the publishers to let me have the copyright. I also appreciate the contributions from my co-authors: Prof. Xinding Fang, Dr. Yuandi Gan, Prof. Yingcai Zheng, and Prof. Leon Thomsen.

ABSTRACT

Modeling dynamic and static responses of an elastic medium often employs different numerical schemes. The elastic properties obtained from the dynamic propagation method are usually frequency dependent. To get the static solution, I introduced a damping parameter to the dynamic modeling process. By introducing damping into the system, I showed how the widely used time-marching staggered finite difference (FD) approach in solving the elastodynamic wave equation can be used to model time-independent elastostatic problems. I verified the damped FD approach by comparing results against the analytical solutions for several models. I also validated my approach numerically for an inclusion model by comparing the results computed by the finite element (FE) method. The damped FD showed excellent agreement with both the analytical results and the FE results.

I then applied the geomechanical modeling to a deep earthquake problem. Recent work using earthquake radiation patterns showed that the subducting slabs hosting deep earthquakes are strongly anisotropic. Such anisotropy may be caused by aligned fluid or melt inclusions of carbonates. If it is the case, I showed that the shear modulus of the inclusion must be less than one-tenth of the matrix shear modulus in order to achieve the strong anisotropy observed. It infers that the inclusion is highly possible to be carbonatite melt or other aqueous fluids. These discoveries constrain the amount of subducted carbon into the Earth carried by slabs.

My second line of research is on seismic imaging. Steeply dipping faults, salt flanks, and subsalt sediments are important geological structures in energy exploration. Conventional seismic imaging in such areas is known to have challenges, due to poor illumination because of the use of

singly scattered waves/primary reflections. I proposed to use multiply scattered waves, especially the secondary scattered waves, in the reverse time migration (RTM), to enhance the seismic illumination for imaging the steep faults and subsalt areas. I applied the method on two synthetic models, a trapezoidal model and the Sigsbee2B model. These two synthetic examples show that the new method achieves better imaging of steep faults and subsalt areas than the traditional RTM.

TABLE OF CONTENTS

LIST OF FIGURES

CHAPTER 1 INTRODUCTION

This dissertation consists of two lines of research. The first one is on geomechanical modeling using a damped finite difference scheme with applications in understanding subducting slab anisotropy (Chapter 2 to Chapter 6). The second one is on how to improve subsalt imaging in particular for high angle faults using secondary scattered seismic waves (Chapter 7). In the following, I will present the background and motivation of each research topic.

1.1 Geomechanical modeling using a damped finite difference method

Geomechanical modeling plays a very important role in exploration geophysics for the lifecycle of oil and gas fields (Oristaglio, 2016), geothermal fluids, ground subsidence, as well as the wellbore stability in drilling. However, it is computationally challenging to compute stress and strain fields in complex geology for a large-scale field. The most widely used numerical method is the finite element method. One needs to mesh the model and invert for a matrix if using the finite element method. Both tasks are quite challenging. The goal of my research is to develop an efficient damped finite difference method to solve for large scale geomechanical problems. The damped finite difference method not only can lead to correct static solutions but also captures both fast (e.g., seismic wave propagation) and slow (viscoelastic deformation) dynamics. This can have a huge practical impact because finite difference model gridding is much easier than the finite element meshing and it is also straightforward to implement the parallel computing for finite difference.

Geomechanics studies the mechanical behavior of rocks in response to forces (Jaeger et al., 2009). A rock's response to applied stresses usually has three stages: linear elastic deformation, plastic deformation, and brittle failure. In this study, I will focus on the elastic regime and effective properties of a heterogeneous rock.

In many cases, we need to understand the effective properties of an elastic medium, which can be a heterogeneous or composite medium with several different constituent materials. For example, when the heterogeneity scale in a rock sample is much smaller than the wavelength, the sample can be viewed as an effectively homogeneous medium. To estimate the effective elastic moduli, we need to know the bulk static strain/deformation given the applied stresses. In this situation, the numerical modeling of the stresses and strains of the rock model is helpful.

Previously, many researchers have proposed to compute the effective moduli with the finite element method (e.g., Garboczi, 1998; Saxena and Mavko, 2016), which is a commonly used numerical modeling method in engineering problems for static stress-strain analyses owing to its geometrical flexibility and numerical accuracy. It can also solve dynamic problems such as fault rupture (Meng, 2017; Meng and Wang, 2018). The finite element method partitions a model into small meshing elements with nodes. Interpolation functions across nodes are used to convert the partial differential equations into a matrix equation system (e.g., Reddy, 2004). However, for static problems with a large degree of freedom, meshing the model into elements and solving the resulting matrix equation can be computationally challenging.

Time-marching finite difference methods are widely used in modeling dynamic seismic wave propagation and scattering (Kelly et al., 1976; Levander, 1988; Schuster, 2017; Virieux, 1984, 1986a). Some authors also used the finite difference method for modeling stresses and strains. Saenger et al., (2000) calculated the effective elastic moduli by propagating a dynamic pulse through a heterogeneous medium using a finite difference method and used the traveltimes of the P and S waves to obtain the effective elastic moduli. Since the group velocity of the elastic wave is a function of the dominant wavelength and the scale of heterogeneity, the effective elastic moduli estimated by this method is therefore frequency dependent. In other words, the results obtained using this method are not strictly static solutions.

Saenger *et al*., (2005; 2006) found during their finite difference viscoelastic wave modeling on digital rocks using Darcy's law that the waves will be highly attenuated by setting high anelastic coefficients, such as an anelastic tensor component equals to 99% of the input P-wave modulus. Since only the non-zero frequency waves will be attenuated, the modeling will end up with the static solution after a sufficient number of time steps (Saenger et al., 2006).

I am motivated to take advantage of the finite difference time-marching schemes in solving the damped elastodynamic equation and obtaining the static stress/strain field of the model without the effort of inverting the large matrix otherwise needed in an implicit finite element method for static problems. The damped finite difference method provides an additional tool for seismic wave modelers to solve geomechanical problems. In Chapter 2 , I will illustrate the concept of the damped elastodynamic equation and give a recipe on choosing the proper

damping parameter to damp out the kinetic energy in the elastic system and obtain the static solutions.

1.2 Seismic imaging using secondary scattered waves

My second line of research is in seismic imaging. Reflection seismic data contain all kinds of events, such as primary reflections, surface-related multiples, and interbed multiples. However, conventional seismic migration algorithms map the acquired seismic data to images as if all the events in the data were primary reflections (i.e., singly scattered). There are two consequences of doing so: 1) the multiples are mapped to the wrong locations as artifacts in images; 2) the primary-reflection geometry has limited illumination in the subsurface. Recently, significant progress has been made in multiple imaging and waveform inversion ((Liu et al., 2011; Liu et al., 2016; Malcolm et al., 2011) and showed that multiples have useful information. In the dissertation, I showed that if taking into account high-order scattering physics, one could achieve better illumination of subsalt imaging and were able to image possibly important high-angle faults. The reverse time migration (RTM) (Baysal et al., 1983; Mcmechan, 1983; Whitmore, 1984) is used as the imaging tool instead of the one-way methods used in previous times.

The conventional RTM image is created by assuming all events in the data are primary reflections or singly scattered events. Due to the geometry of the surface seismic survey where sources and receivers are located near the earth's surface, the primary reflections may not be able to reach the “shadow zones” where illumination is poor. Typical “shadow zones” include high-angle faults, steep salt flanks and subsalt sediments. An accurate image of these areas is very

important for identifying reservoirs and drilling prospects for oil and gas production. In the past, geophysicists showed that with secondary scattered waves (e.g., Dai and Schuster, 2013; Ding et al., 2019; He and Wu, 2009) and multiples (e.g., Liu et al., 2015; Lu et al., 2015; Malcolm et al., 2011; Malcolm et al., 2009), one can increase the illumination of seismic images. These waves have unique wave paths, which can reach shadow areas that primary reflections are not able to (Liu et al., 2011).

Using wave-generated secondary sources to increase illumination has been applied in different contexts by different authors. Most authors used high contrast reflecting boundaries as secondary "sources" (Dai and Schuster, 2013; Ding et al., 2019; Farmer et al., 2006; Jin et al., 2006; Kryvohuz and Kuehl, 2019; Malcolm et al., 2011; Tan and Huang, 2014). He and Wu, (2009) used natural point scatterers such as pinch outs and sharp edge points on salt boundaries. Some authors explicitly put these strong reflecting boundaries in the smoothed velocity model (e.g., Farmer et al., 2006; Jin et al., 2006; Tan and Huang, 2014) and others considered them as Born scattering sources (Dai and Schuster, 2013; Kryvohuz and Kuehl, 2019).

Different from the previous implementations, my proposed secondary scattering method in this dissertation uses point scatterers instead of continuous reflectors (or mirror source) as secondary sources and does not require the structure to have a true scatterer like a pinch out or a sharp edge point. Furthermore, the scatterers are created by density anomalies such that the traveltimes would not be affected.

1.3 Layout of the dissertation chapters

The dissertation has 7 chapters:

- In Chapter 1, I introduced about the ideas in the dissertation and their impacts.

- In Chapter 2 , I showed how to obtain the static solution by solving a dynamic equation, using a 1D example.
- In Chapter 3 , I described the methodology of the damped finite difference method for the measurements of static stress and strain fields with implementation details.
- In Chapter 4 , I verified the damped finite difference method's results with the analytical solutions for four models.
- In Chapter 5 , I compared and benchmarked the damped finite difference method with the finite element method.
- In Chapter 6 , I used the damped finite difference method to analyze the high anisotropy in the subducted slabs and its implication of deep carbon cycle.
- In Chapter 7 , I showed the methodology, results and conclusions of my second line of work: seismic imaging using secondary scattered waves.

CHAPTER 2 ONE-DIMENSIONAL EXAMPLE OF A SPRING-MASS SYSTEM

In Chapter 1 , I introduced the concept and advantages of solving for static stress/strain solutions using damped dynamic equations. In this chapter, I will use a 1D spring-mass system to illustrate and motivate the concept. I will show the validity of using viscous damping in a dynamic equation to solve for the static stress/strain solution.

2.1 Objective

The goal is to demonstrate how to obtain the static solution by solving a dynamic equation but with viscous damping using a 1D spring-mass system as an example.

2.2 Problem statement

Consider a massless spring of a natural length, L_0, with one end fixed at the ceiling and the other end free (Figure 1(a)). If a force (in this case, the gravity of a ball with mass m) is attached to the lower end of the spring (i.e., equivalent stress boundary condition) (Figure 1(b)), what is the axial strain?

2.3 Static solution

One can get the elongation (i.e., deformation) of the spring ΔL , using Hooke's law:

$$k\Delta L = mg, \tag{1}$$

where k is the spring constant and g is the gravitational acceleration. The axial strain ϵ is:

$$\epsilon = \frac{\Delta L}{L_0} = \frac{mg}{kL_0}. \tag{2}$$

Next, we will convert this problem into a dynamic oscillatory problem whose long-term solution approaches to the static solution.

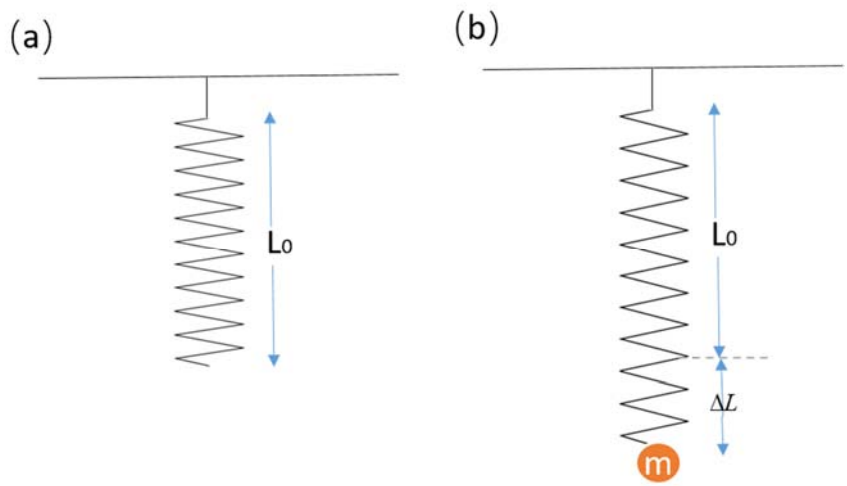

Figure 1. A free spring with no force applied (a) and with a mass *m* attached to the lower end (b).

2.4 Static solution in a viscous fluid

If one puts the spring system with the ball attached (Figure 2(a)) in a viscous fluid (Figure 2(b)) and does not consider the fluid buoyance, the amount of spring elongation is the same as if when no viscous fluid is present. When the ball is force balanced in the viscous fluid, there are only two forces: gravity and the elastic force from the spring, as in the case of Equation (1). Therefore, we will get the same strain solution.

However, there will be a viscous force when the ball is in motion and has a relative velocity with respect to the fluid.

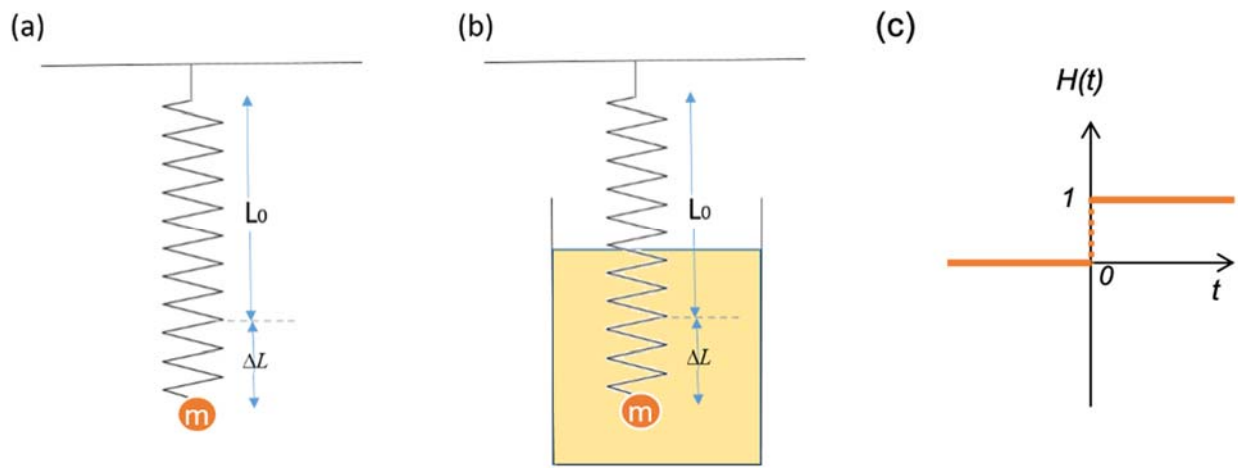

Figure 2. (a) spring with a ball and (b) spring with a ball in a viscous fluid. (c) the step function *H(t)* showing the time history of the applied force, as in Equation (3).

2.5 Dynamic solution in a viscous fluid

At time zero, a ball with mass m is suddenly hooked to the spring immersed in the viscous fluid with viscosity η (Figure 2(b)). The force history on the spring is a step function (Figure 2(c)). Immediately, the ball will start to oscillate and it will approach the final equilibrium position. How soon the equilibrium state can be reached depends on the viscosity. If the viscosity is very large, the mass sinks slowly and it will take a very long time to reach the final equilibrium position. If there is zero viscosity, the mass will oscillate forever around the equilibrium position. These two extreme situations imply the existence of a special viscosity value corresponding to an optimal damping case which can get to the equilibrium state in the shortest time.

The dynamic equation governing the displacement of the ball in a viscous fluid is

$$m\frac{dx(t)^2}{dt^2} + \eta\frac{dx(t)}{dt} + kx(t) = mgH(t), \tag{3}$$

where $x(t)$ is the time (t) dependent displacement, m is the mass of the ball, k is the spring constant, and g is the gravitational acceleration. $H(t)$ is a step function showing the force time history:

$$H(t) = \begin{cases} 0, t \leq 0 \\ 1, t > 0 \end{cases}. \tag{4}$$

The solution of Equation (3) is (Udias and Buforn, 2017):

$$x(t) = Aexp\left(-\frac{\omega_0}{2Q}t\right)sin(\omega t + \phi) + \frac{mg}{k}, \;\; t > 0, \tag{5}$$

and

$$\omega = \omega_0\sqrt{1 - \frac{1}{4Q^2}}, \tag{6}$$

$$Q = \frac{m\omega_0}{\eta}, \tag{7}$$

$$\omega_0 = \sqrt{k/m}, \tag{8}$$

where A is the amplitude, ϕ is the initial phase and ω_0 is the harmonic oscillation frequency corresponding to the zero viscosity (i.e., $\eta = 0$) case.

Equation (5) represents a damped oscillation. As time $t \to +\infty$, the mass will converge to the equilibrium displacement $x(t \to +\infty) = \frac{mg}{k}$, which gives exactly the same axial strain as in

the static case (Equation (1)). This example shows that the time-dependent dynamic solution converges to the static solution.

2.6 Numerical examples

In the following examples, I show the scenarios of dynamic solutions in two fluids of different viscosities.

Two identical springs of a spring constant $k = 40\ N/m$ and a natural length $L_0 = 0.08\ m$ are in two different viscous fluids (Figure 3). One fluid is of viscosity $2\ Pa \cdot s$, and the other is of viscosity $1.4\ Pa \cdot s$.

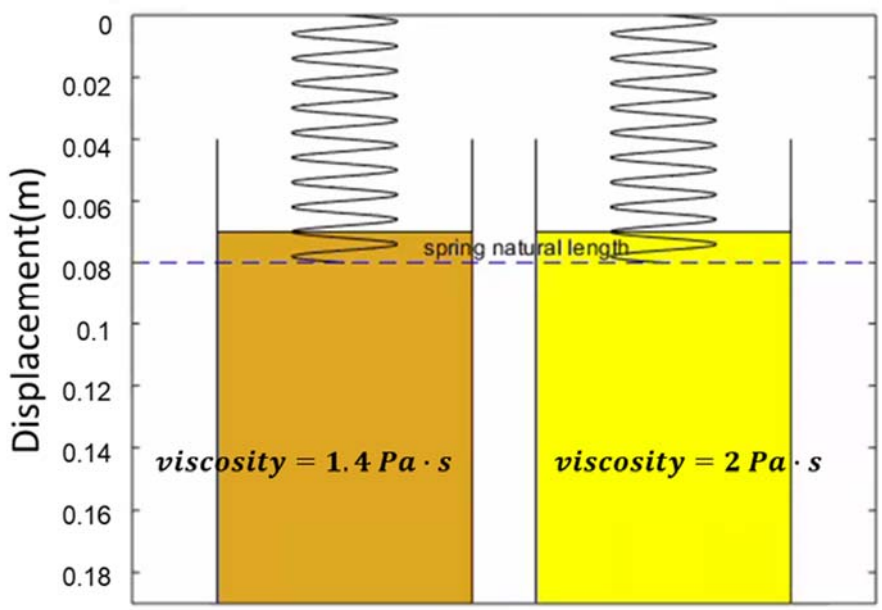

Figure 3. The initial states of the springs.

At time zero, two balls of the same mass $m = 0.2\ kg$ are hooked to the two springs, respectively. The gravity of the ball will act as a sudden external force on the spring, causing the spring to oscillate (See my movie at https://www.youtube.com/watch?v=_596xkYG7-c).

However, the viscous fluid will impose a resistant force on the balls to gradually slow down their oscillations.

The two different fluid viscosities act as different damping parameters on the spring-mass system. The ball in the fluid of viscosity 2 $Pa \cdot s$ will stop earlier than the one in the fluid of viscosity 1.4 $Pa \cdot s$. However, the two balls both stop at the same displacement position equivalent to the static solution of Equation (1).

With the values assigned to the parameters in Equation (1) , I get

$\Delta L = \frac{mg}{k} = \frac{0.2 \times 9.8}{40} = 0.049\ (m)$.

The final position of the balls will be at $L_0 + \Delta L = 0.129\ m$ (Figure 4).

Figure 4

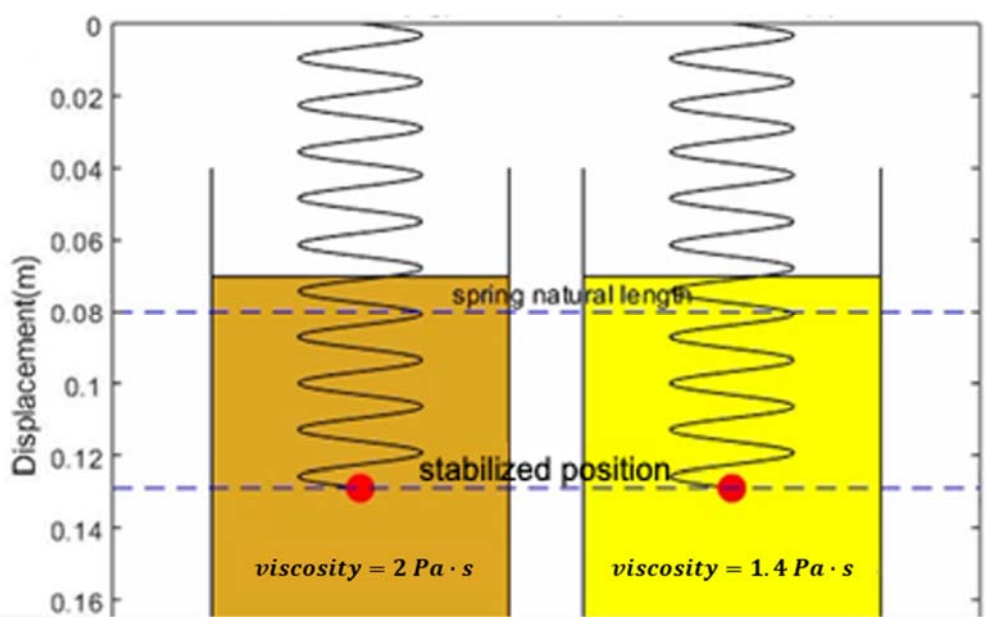

Figure 4. The final status of the springs.

2.7 Critical damping

In the above two examples, although both balls stop at the same position, the times to reach the equilibrium are different, due to different viscosities of the fluids. In the following analysis, I will introduce the concept of the critical damping. If the viscosity of the fluid is equal to the critical damping, the spring-ball system will approach its equilibrium status in the shortest time.

To study the damping factor, I consider a homogenous version (the right hand side of the equation is zero). In this case, the second order differential Equation (3) admits a solution in the form of:

$$x(t) = e^{\lambda t}. \tag{9}$$

Here I rename the viscosity η the damping parameter c. Substituting $x(t)$ in Equation (3) with Equation (9) results in a quadratic equation:

$$m\lambda^2 + c\lambda + k = 0, \tag{10}$$

and the roots of the equation are:

$$\lambda = \frac{-c \pm \sqrt{c^2 - 4mk}}{2m}. \tag{11}$$

When the damping parameter $c > 2\sqrt{mk}$, λ is always a negative real number and the system is called overdamped. When $c < 2\sqrt{mk}$, λ is a complex number with a negative real part corresponding to an exponential decay but a non-zero imaginary part corresponding to oscillation and the system is called underdamped. The critical damping occurs when $c = 2\sqrt{mk}$ and the ball will reach its equilibrium state in the shortest amount of time (Gregory, 2006).

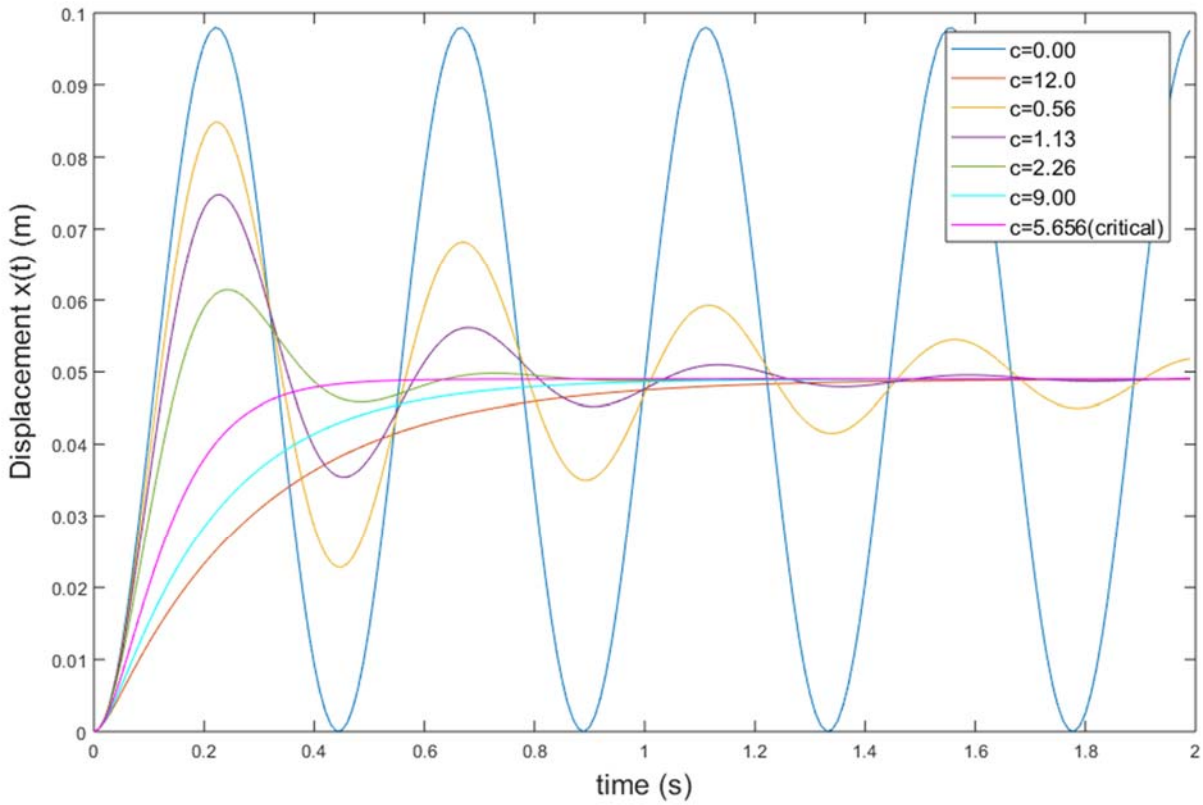

Figure 5. Spring displacements for different viscous damping parameters.

In Equation (11), when $c = 2\sqrt{mk}$, the displacement $x(t)$ decays the fastest. This damping parameter makes the system stabilize with the least amount of time, and therefore is called the critical damping parameter. From Figure 5 we know that when

$$c = 2\sqrt{km} = 2 \times \sqrt{40 \times 0.2} = 5.656,$$

the system reaches an equilibrium of $x = 0.049\ m$ with the least amount of time, taking about $0.6\ s$, while the other damping parameters all take a longer time than that.

When the damping parameter $c = 0$, there is no damping applied (Figure 5), which implies a harmonic period T of about $0.444\ s$. In this case, the spring oscillates at its natural frequency. The critical damping parameter $c_{critical}$ can be calculated using the following equation:

$$c_{critical} = 2\sqrt{km} = 2m\sqrt{\frac{k}{m}} = 2m\omega_n, \tag{12}$$

where ω_n represents the natural frequency, which in the above case is calculated as $\omega_n = \frac{2\pi}{T} = 14.14\ rad/s$.

2.8 Conclusions and generalizations

In this 1D example, I explained how a static solution can be obtained by solving a damped dynamic equation. At time zero, an external force is imposed on the system and is kept on ever since. It is a step function force. This sudden force will trigger the spring to oscillate. If viscous damping is applied, the kinetic energy will die out eventually and make the system stabilized at the same state as the original static problem. In 2D or 3D cases, similar ideas can be generalized. The applied forces will be acting on the elastic model boundaries in a step function manner. Before time zero, no forces are applied; at time zero, the forces are suddenly applied on the boundaries and cause oscillations of the particles in the model; after time zero, the forces are kept on and act as zero-frequency static forces. Since damping is applied in the system, the kinetic components will be damped out eventually and the system will stabilize at the static solution. The

driving function form does not matter as long as the forces become constants beyond a time point. In later chapters, I will solve the damped dynamic finite difference equations to obtain the static solutions.

CHAPTER 3 METHODOLOGY

A damped dynamic finite difference approach for modeling static stress-strain fields

In Chapter 2 , I demonstrated that we could obtain the elastostatic solution by solving a damped dynamic equation for the spring-mass system in a viscous fluid. Likewise, in a 2D or 3D case, we can view an elastic medium as a web of inter-connected mass points and springs. We can immerse this system in a viscous fluid and solve the dynamic problem. This viscous immersion can be realized by adding a damping term in a dynamic equation. This has an obvious advantage in numerical calculations since we can employ the time-marching finite difference method to solve for stress and strain. In 2D and 3D elastic cases where a large number of model grids are used, solving the elastodynamic equations in a time-marching fashion can be easier and more efficient than solving the static equations.

3.1 Static, dynamical, and damped dynamical equations

The governing equation for modeling static loading is

$$\nabla \cdot \boldsymbol{\sigma} = 0, \tag{13}$$

where $\sigma(x, y, z)$ is the time-independent stress tensor in the interior of the computational domain. Since $\sigma(x, y, z)$ represents a time-independent variable, Equation (13) could not be solved by the regular time-marching dynamic finite difference method directly. Instead, I solved the damped wave equation of the form (Morse and Feshbach, 1954, p.868):

$$\rho \frac{\partial \vec{v}}{\partial t} + \rho \vec{v}\, d = \nabla \cdot \boldsymbol{\sigma}, \tag{14}$$

where $\vec{v}(x, y, z, t)$ is the particle motion velocity field and $\sigma(x, y, z, t)$ is the stress tensor field. Both fields depend on time t and spatial coordinates x, y, and z. $\rho(x, y, z)$ is density, and d is a constant positive damping parameter. If $d = 0$, Equation (14) becomes the regular wave equation:

$$\rho \frac{\partial \vec{v}}{\partial t} = \nabla \cdot \boldsymbol{\sigma}. \tag{15}$$

Equation (14) is a time evolution equation for the particle velocity and stress fields. As time elapses, the kinetic energy in the system will be progressively reduced. When the kinetic energy damps out and particle velocities become zero, the left side of Equation (14) vanishes and the displacement field becomes the static field we want. The resultant stress field $\boldsymbol{\tau}$ is the static field that satisfies both the elastostatic Equation (13) and the boundary conditions.

3.2 Finite difference modeling for regular elastodynamic wave equations

Before introducing the damped finite difference method, I firstly review the regular staggered grid finite difference method, upon which the new damped finite difference method is based on.

Assume the medium is elastic and isotropic, the elastodynamic wave equation for a two dimensional (x, z) medium can be written as (e.g., Virieux, 1986a):

$$\begin{cases} \frac{\partial v_x}{\partial t} = b\left(\frac{\partial \sigma_{xx}}{\partial x} + \frac{\partial \sigma_{xz}}{\partial z}\right) \\ \frac{\partial v_z}{\partial t} = b\left(\frac{\partial \sigma_{xz}}{\partial x} + \frac{\partial \sigma_{zz}}{\partial z}\right) \\ \frac{\partial \sigma_{xx}}{\partial t} = (\lambda + 2\mu)\frac{\partial v_x}{\partial x} + \lambda\frac{\partial v_z}{\partial z} \\ \frac{\partial \sigma_{zz}}{\partial t} = (\lambda + 2\mu)\frac{\partial v_z}{\partial z} + \lambda\frac{\partial v_x}{\partial x} \\ \frac{\partial \sigma_{xz}}{\partial t} = \mu\left(\frac{\partial v_x}{\partial z} + \frac{\partial v_z}{\partial x}\right) \end{cases}, \tag{16}$$

where $b(x, z)$ is the reciprocal of density, $\lambda(x, z)$ and $\mu(x, z)$ are the Lamé constants, $v_x(x, z)$ and $v_z(x, z)$ represent velocity fields of the x and z components, respectively, $\sigma_{xx}(x, z)$ and $\sigma_{zz}(x, z)$ are the normal stresses and $\sigma_{xz}(x, z)$ is the shear stress.

The discretized form of Equation (16) using the centered finite difference leads to a staggered-grid scheme (Virieux, 1986a). The expressions for the discretized Equation (16) in terms of velocities v_x and v_z and stresses σ_{xx}, σ_{zz} and σ_{xz} with second-order accuracy in both space and time are :

$$U_{i+1/2,j}^{k+1/2} = U_{i+1/2,j}^{k-1/2} + B_{i+1/2,j}\frac{\Delta t}{\Delta x}\left(\Sigma_{i+1,j}^{k} - \Sigma_{i,j}^{k}\right) + B_{i+1/2,j}\frac{\Delta t}{\Delta z}\left(\Xi_{i+1/2,j+1/2}^{k} - \Xi_{i+1/2,j-1/2}^{k}\right), \tag{17}$$

$$V_{i,j+1/2}^{k+1/2} = V_{i,j+1/2}^{k-1/2} + B_{i,j+1/2}\frac{\Delta t}{\Delta x}\left(\Xi_{i+1/2,j+1/2}^{k} - \Xi_{i-1/2,j+1/2}^{k}\right) + B_{i,j+1/2}\frac{\Delta t}{\Delta z}\left(\mathrm{T}_{i,j+1}^{k} - \mathrm{T}_{i,j}^{k}\right), \tag{18}$$

$$\Sigma_{i,j}^{k+1} = \Sigma_{i,j}^{k} + (L+2M)_{i,j}\frac{\Delta t}{\Delta x}\left(U_{i+1/2,j}^{k+1/2} - U_{i-1/2,j}^{k+1/2}\right) + L_{i,j}\frac{\Delta t}{\Delta z}\left(V_{i,j+1/2}^{k+1/2} - V_{i,j-1/2}^{k+1/2}\right), \tag{19}$$

$$\mathrm{T}_{i,j}^{k+1} = \mathrm{T}_{i,j}^{k} + (L+2M)_{i,j}\frac{\Delta t}{\Delta \mathrm{z}}\left(V_{i,j+1/2}^{k+1/2} - V_{i,j-1/2}^{k+1/2}\right) + L_{i,j}\frac{\Delta t}{\Delta x}\left(U_{i+1/2,j}^{k+1/2} - U_{i-1/2,j}^{k+1/2}\right), \tag{20}$$

$$\Xi_{i+1/2,j+1/2}^{k+1} = \Xi_{i+1/2,j+1/2}^{k} + M_{i+1/2,j+1/2}\frac{\Delta t}{\Delta \mathrm{z}}\left(U_{i+1/2,j+1}^{k+1/2} - U_{i+1/2,j}^{k+1/2}\right) + M_{i+1/2,j+1/2}\frac{\Delta t}{\Delta x}\left(V_{i+1,j+1/2}^{k+1/2} - V_{i,j+1/2}^{k+1/2}\right), \tag{21}$$

where Σ represents the normal stress σ_{xx}, Ξ represents the shear stress σ_{xz}, T represents the normal stress σ_{zz}, U represents the velocity v_x, and V represents the velocity v_z. L and M represent the Lamé constants. Δt is the time grid step, Δx and Δz are grid steps in x-axis and z-axis directions, respectively, and B is the buoyancy of the model (Virieux, 1986a). The superscript means the time step, the subscripts are x and z grid numbers separated by a comma.

An illustration of the staggered-grid layout in a two dimensional medium is shown below (Figure 6).

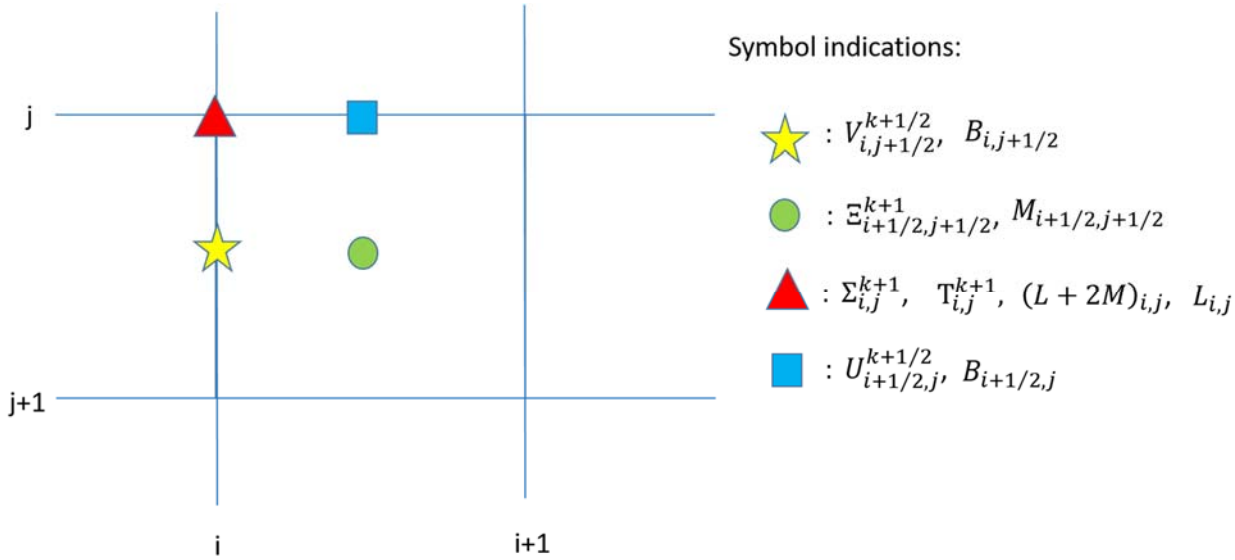

Figure 6. The 2D staggered-grid finite difference scheme.

3.3 Finite difference modeling of damped elastodynamic wave equations

3.3.1 Damped elastic equation in component form

I have done both 2D and 3D modeling. However, in the following theoretical analysis, for simplicity and comparison with the original elastodynamic wave equations, I only discuss two-dimensional (x, z) modeling as an example. The 3D cases will be shown in numerical examples.

Assume the model material is isotropic, Equation (14) can be expressed as the following first-order velocity-stress equations:

$$\begin{cases} \frac{\partial v_x}{\partial t} + d v_x = b\left(\frac{\partial \sigma_{xx}}{\partial x} + \frac{\partial \sigma_{xz}}{\partial z}\right) \\ \frac{\partial v_z}{\partial t} + d v_z = b\left(\frac{\partial \sigma_{xz}}{\partial x} + \frac{\partial \sigma_{zz}}{\partial z}\right) \\ \frac{\partial \sigma_{xx}}{\partial t} = (\lambda + 2\mu)\frac{\partial v_x}{\partial x} + \lambda \frac{\partial v_z}{\partial z} \\ \frac{\partial \sigma_{zz}}{\partial t} = (\lambda + 2\mu)\frac{\partial v_z}{\partial z} + \lambda \frac{\partial v_x}{\partial x} \\ \frac{\partial \sigma_{xz}}{\partial t} = \mu\left(\frac{\partial v_x}{\partial z} + \frac{\partial v_z}{\partial x}\right) \end{cases}, \tag{22}$$

where b is the reciprocal of density, λ and μ are the Lamé constants; v_x and v_z represent velocity fields of the x and z components, respectively, σ_{xx} and σ_{zz} are normal stresses and σ_{xz} is the shear stress. The damping parameter d is a constant that should be determined before formally running the modeling process.

3.3.2 Damped elastic equation in discretized form

Equation (22) can be solved using the staggered-grid finite difference method (e.g., Fang et al., 2014; Virieux, 1986a). The finite difference formulas for stresses σ_{xx}, σ_{zz} and σ_{xz} are the same as in the original elastodynamic wave equations case (Equation (19) to Equation (21)).

The finite difference formulas for velocities v_x and v_z with second-order accuracy in both space and time are expressed as:

$$U_{i+1/2,j}^{k+1/2} = \frac{1}{1+\frac{d\Delta t}{2}}\left[\left(1-\frac{d\Delta t}{2}\right)U_{i+1/2,j}^{k-1/2} + B_{i+1/2,j}\frac{\Delta t}{\Delta x}\left(\Sigma_{i+1,j}^{k} - \Sigma_{i,j}^{k}\right) + B_{i+1/2,j}\frac{\Delta t}{\Delta z}\left(\Xi_{i+1/2,j+1/2}^{k} - \Xi_{i+1/2,j-1/2}^{k}\right)\right], \tag{23}$$

$$V_{i,j+1/2}^{k+1/2} = \frac{1}{1+\frac{d\Delta t}{2}}\left[\left(1-\frac{d\Delta t}{2}\right)V_{i,j+1/2}^{k-1/2} + B_{i,j+1/2}\frac{\Delta t}{\Delta x}\left(\Xi_{i+1/2,j+1/2}^{k} - \Xi_{i-1/2,j+1/2}^{k}\right) + B_{i,j+1/2}\frac{\Delta t}{\Delta z}\left(\mathrm{T}_{i,j+1}^{k} - \mathrm{T}_{i,j}^{k}\right)\right], \tag{24}$$

where Σ represents the normal stress σ_{xx}, Ξ represents the shear stress σ_{xz}, T represents the normal stress σ_{zz}, U represents velocity v_x and V represents velocity v_z. Δt is the time grid step, Δx and Δz are grid steps in the x-axis and z-axis directions, respectively, and B is the buoyancy of the model (Virieux, 1986a). The superscript means time step and the two subscripts are the x and z grid numbers separated by a comma.

The 3D form of the staggered-grid finite difference equations can be easily derived following the above 2D discretized equations, by adding another parameter in the *y* direction. An illustration of the 3D staggered-grid stencil is shown in Figure 7.

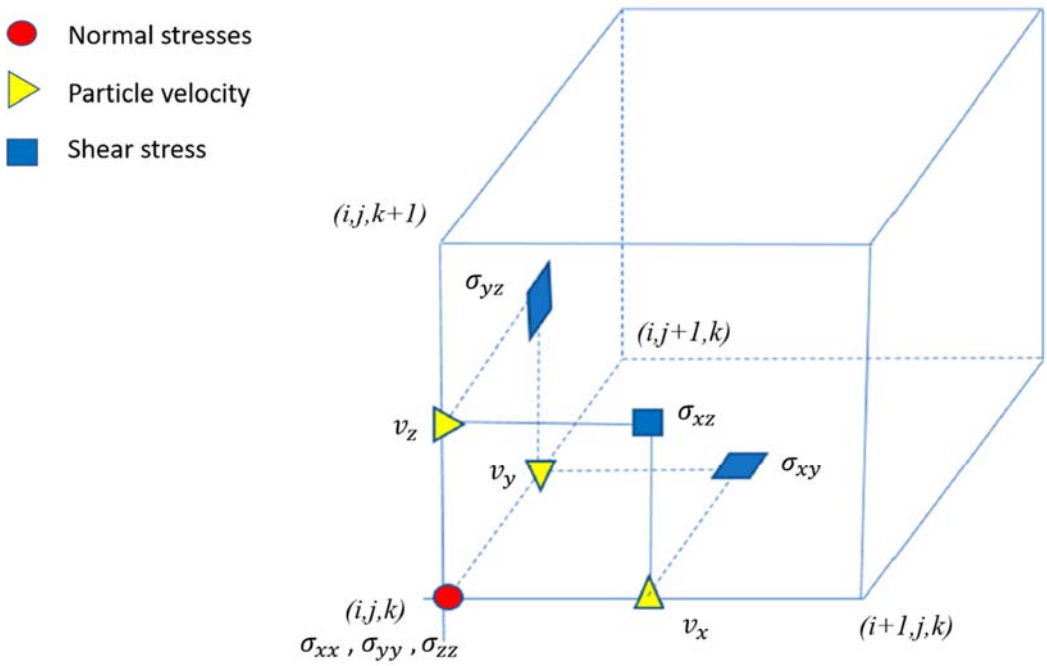

Figure 7. The finite difference staggered-grid stencil for 3D medium.

The static stress or strain boundary conditions are imposed on the boundaries of the model at time zero. They produce elastic waves (deformations) that contain both static and dynamic components. The static and dynamic elastic energy can be respectively characterized by the model's strain energy and kinetic energy (Aki and Richards, 1980) over time. To obtain the static response, we need to choose an appropriate value for the damping parameter, d, to damp out the kinetic energy efficiently. Once the system reaches an equilibrium, the 3D stress and strain fields can be used to derive the effective elastic moduli of the model.

3.4 Choice of the optimal damping parameter

It is heuristic to study a 1D damped system firstly. For a damped harmonic oscillator as I have discussed for Equation (3), there exists a critical damping coefficient $c_{critical}$ which will make the oscillation system reach equilibrium with minimal amount of time. Based on Equation (3), the critical damping coefficient $c_{critical}$ can be solved as (see Chapter 1)

$$c_{critical} = 2m\sqrt{k/m} = 2m\omega_n, \tag{25}$$

where ω_n is the natural frequency or resonance frequency of the oscillator corresponding to no damping. Since we can view the elastic medium as a web of inter-connected mass points and springs, each mass point can be seen as a damped harmonic oscillator. The relationship between the natural frequency of the system and critical damping coefficient should persist in the 2D model as described in Equation (22). The following 2D example will show the relationship between the natural frequency and the critical damping parameter.

Firstly, the natural frequency of a homogenous model was analyzed by numerical modeling using the finite difference method. I set the damping parameter d in Equation (14) to be zero and observed the motion of the nodes in the model under prescribed stresses as boundary conditions. I used a $200\ m$ by $200\ m$ homogeneous 2D model with the P-wave velocity $V_P = 4382\ m/s$, the S-wave velocity $V_S = 2530\ m/s$, and the density $\rho = 3000\ kg/m^3$. Spatial steps in x and z directions are $\Delta x = \Delta z = 2\ m$, and the time step is $\Delta t = 0.15\ ms$. The Δx, Δz and Δt are chosen to satisfy the numerical stability condition for the explicit scheme, $V_P \frac{\Delta t}{\Delta x} < \frac{1}{\sqrt{2}}$ (Virieux, 1986a). The model is prescribed with normal stresses $\sigma_{xx} = 1\ MPa$ and $\sigma_{zz} = 1\ MPa$

on all four boundaries. I analyzed the x direction particle displacement (Figure 9) of the three selected nodes at coordinates $(4\ m, 4\ m), (98\ m, 98\ m)$ and $(180\ m, 180\ m)$ (Figure 8).

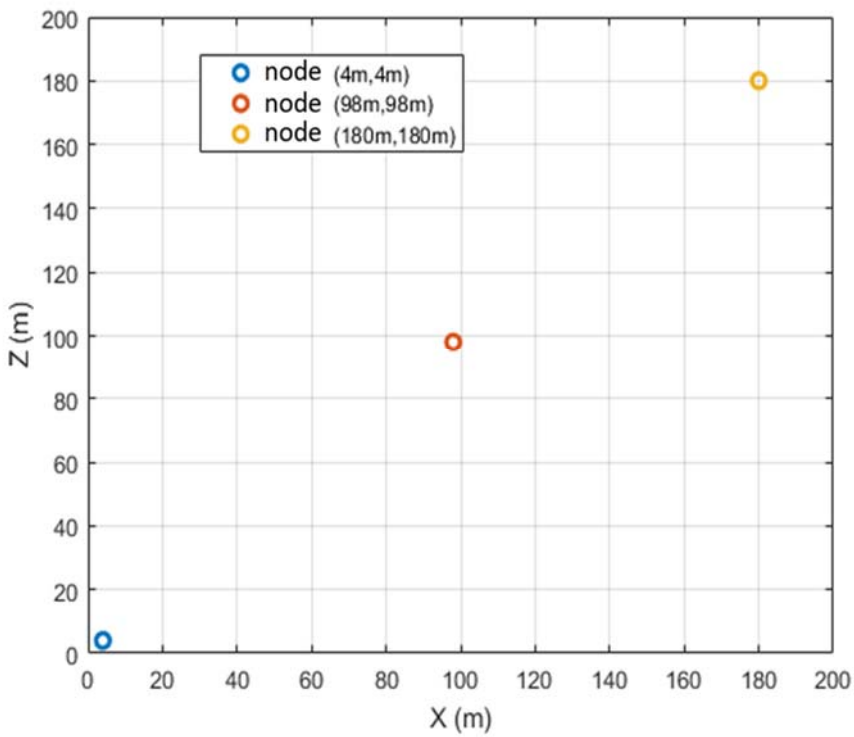

Figure 8. Illustration of the 2D model domain and the three picked nodes. Their locations are at coordinates $(4\ m, 4\ m), (98\ m, 98\ m)$, and $(180\ m, 180\ m)$.

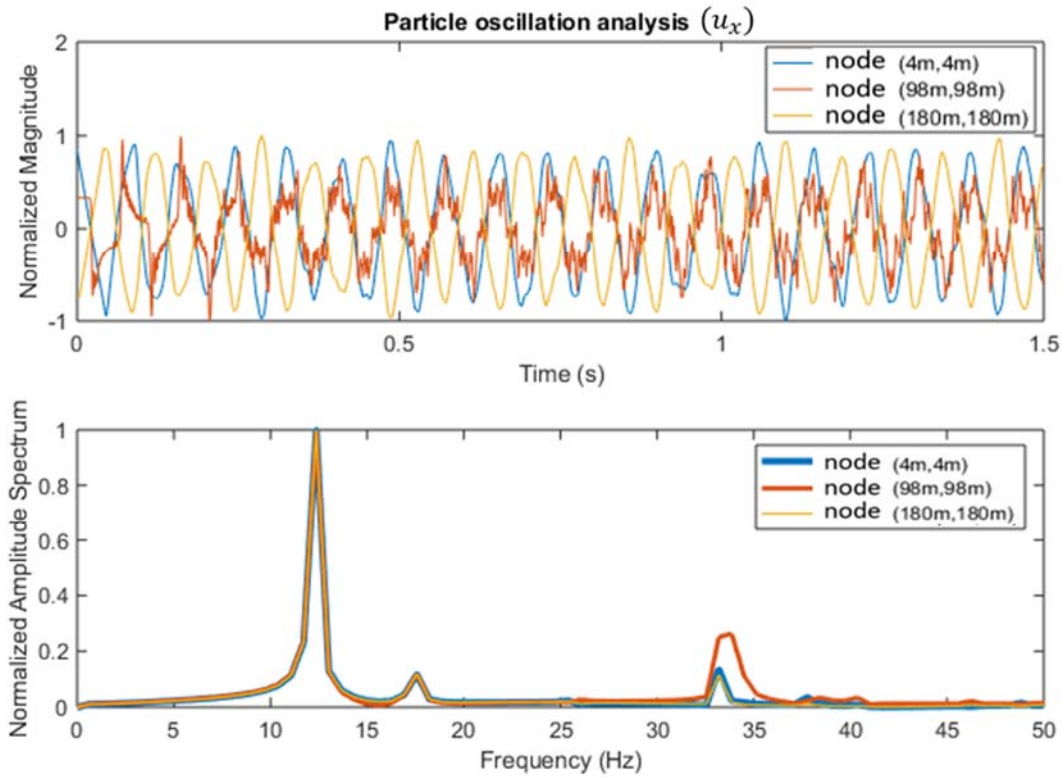

Figure 9. Particle displacements in the x direction and the corresponding amplitude spectra. It implies that a consistent harmonic oscillation frequency may be obtained for the estimate of the damping coefficient. The displacement along x direction (u_x) of nodes at three picked locations are plotted on the top panel. The other nodes in the model are not plotted here but their displacements obey the same pattern. The displacements along z direction (u_z) are not displayed but they behave the same as u_x.

I Fourier transformed the time-domain waveforms to the frequency domain. We can see in Figure 9, that the resonance frequency having the largest energy is $12.37\ Hz$ for the homogeneous isotropic model. It will be used as the natural frequency of the model. I then plug this frequency into Equation (25) to calculate the critical damping coefficient. From Equation (25), the normalized damping parameter in Equation (14) takes the form of:

$$d = \frac{C_{Critical}}{m} = 2\omega_n = 2 \times 2\pi \times f_n. \tag{26}$$

Since the damping parameter d is used in the form of $d\Delta t$ in Equation (23) and Equation (24), it is convenient to denote $D = d\Delta t$. The parameter d has the unit of rad/s, but D is unitless. In the following, I use $D = d\Delta t$ instead of d.

The time evolution of the total strain energy and kinetic energy in the system for different damping parameters are computed (Figure 10). The model is said to reach the static equilibrium when the strain energy converges to a stable value and the kinetic energy drops below a certain small threshold. With a damping parameter $D = 0.0233$, the system reaches the equilibrium using the shortest amount of time. As expected, the strain energy converges to the same value regardless of the damping parameters as long as it is positive. The number of time steps needed under different damping parameters are also analyzed (Figure 11)and it shows the existence of an optimal damping value.

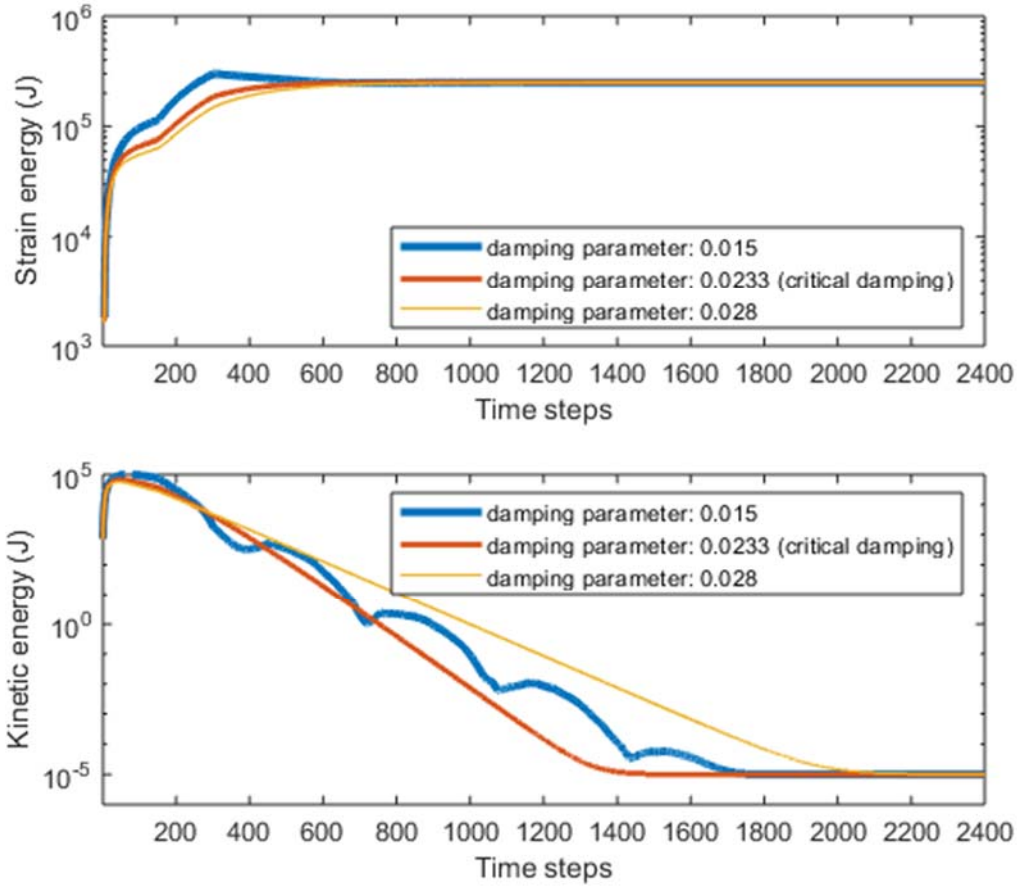

Figure 10. Strain and kinetic energy for the entire model versus the number of time steps in the finite difference modeling. The energy is displayed in the log scale. Here, I set the equilibrium threshold for the kinetic energy as $10^{-5}\,J$. Curves in different colors show the energy evolution with different damping parameters, D. The model reaches the equilibrium after 1400, 1780, and 2100 time steps for damping parameters D set to 0.0233, 0.015, and 0.028, respectively. The strain energy stabilizes at $2.552 \times 10^5\,J$ regardless of the choice of the damping parameter.

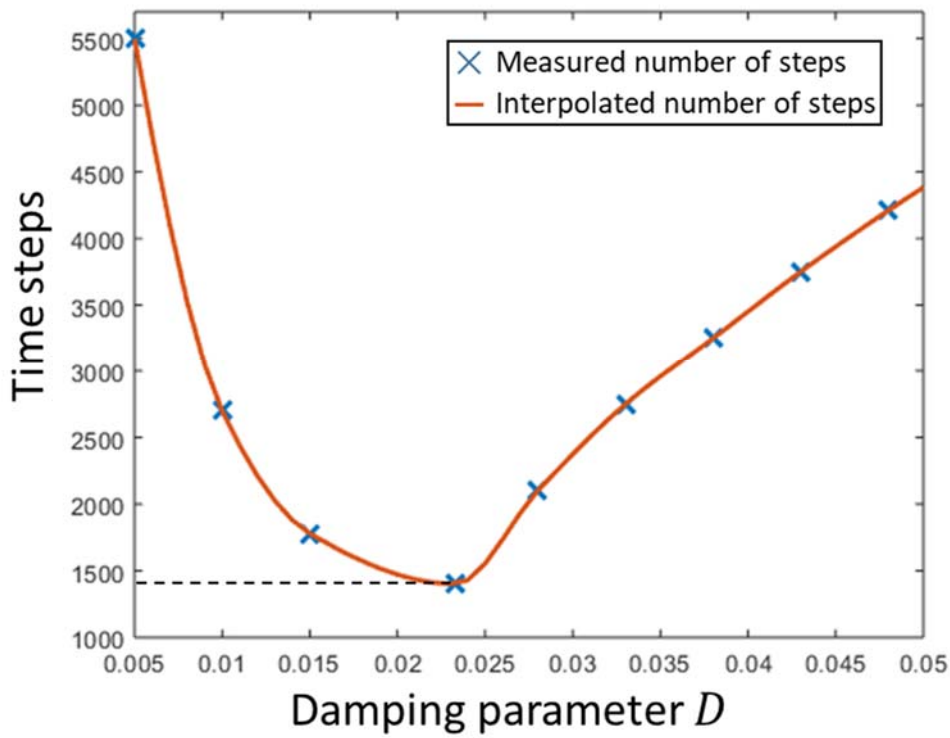

Figure 11. The number of time steps required for the system to reach equilibrium for different damping parameters. The optimal damping occurs when the damping parameter D close to 0.023 using nearly 1400 time steps.

Additionally, if we use a bigger Δt, the number of time steps to reach the equilibrium will be surely reduced, as long as it satisfies the numerical stability condition for the explicit scheme that $V_P \frac{\Delta t}{\Delta x} < \frac{1}{\sqrt{2}}$. For example, under the same damping parameter d, when $\Delta t = 0.3\ ms$, the number of time steps to reach the equilibrium is half of that of the case $\Delta t = 0.15\ ms$. Furthermore, if I use bigger spatial steps Δx and Δz, a bigger Δt can be tolerated.

One thing to notice is that the natural frequency is independent of Δx, Δz, and Δt. The natural frequency is related to the model geometry and material properties.

3.4.1 Natural frequency and standing waves

The natural frequency of the model is related to the standing waves. The forces (with a time history of step function) applied on the model boundaries generate seismic waves that bounce back and forth within the model to produce reflections and resonance. Standing waves form because of interference of waves propagating in opposite directions. For the condition that the four boundaries of the 2D square model are fixed/rigid (zero displacement), the fundamental frequency of the resonance is

$$f = \frac{v}{2L}, \tag{27}$$

where v is the wave propagation velocity, L is the edge length of the square model (Blackstock, 2000). Since in this case only normal stresses are applied, the velocity v is approximated by the P-wave velocity of the homogeneous and isotropic model. Therefore, the fundamental frequency is approximated as $f = \frac{4382}{2\times200} = 10.96\ Hz$, which is close to the $12.37\ Hz$ obtained from the numerical analysis (Figure 9). This approximation offers a more practical and much faster way to estimate the critical damping parameter without the effort to run the time-consuming numerical calculation.

Although the fundamental natural frequency I derived from Equation (27) is not the exact one, the damping performance is still satisfactory. For this model, the damping parameter I got from the approximated fundamental frequency $10.96\ Hz$ is $D = 0.0206$, and the number of time steps it takes to reach the equilibrium is 1500 (Figure 11). This means there is flexibility in choosing the damping parameter. Using the optimal D will allow the dynamic model to reach its

static equilibrium in the least amount of time. However, using a sub-optimal value D will still allow us to obtain the same static equilibrium state in a satisfactory efficiency without doing the time-consuming spectral analysis.

3.4.2 Damping factor of an inhomogeneous model

When the model is inhomogeneous, the procedures to obtain the damping parameter are the same as the homogeneous case. We can estimate the resonance frequency of the inhomogeneous medium simply using Equation (27). However, the velocity should be the averaged P-wave velocity over the compositions of the inhomogeneous model. A 500 by 500 grid (in both x and z direction spatial steps 2 m) porous sandstone model with porosity 0.24 is used as an example. The rock matrix of this model is set to be quartz and the pores are saturated with water (Figure 12). To estimate the average velocity of the model, we used an empirical porosity-velocity relation suggested by Raymer et al., (1980):

$$V = (1 - \emptyset)^2 V_0 + \emptyset V_{fl}, \tag{28}$$

where V, V_0 and V_{fl} are the velocities of the rock, the mineral matrix and the pore fluid, respectively, and $\emptyset$ is the porosity of the model. In this model, $\emptyset = 0.24$, the P-wave velocity of quartz is $V_0 = 6018.8$ m/s, and the P-wave velocity of water is $V_{fl} = 1500$ m/s. Substitute these parameters into Equation (28) I get $V = 3836.5$ m/s. Using Equation (27), the approximate fundamental frequency is calculated as 1.92 Hz.

To verify the fundamental frequency calculated via Equation (27) and (28), I applied the normal stress of $\sigma_{xx} = 1\ MPa$ and $\sigma_{zz} = 1\ MPa$ on all four boundaries since time zero (i.e. step

function time history), as in the previous homogeneous example. I numerically modeled the displacement fields and analyzed the oscillation and amplitude spectra (Figure 13) for selected nodes (Figure 12). From the analysis (Figure 13), the average resonance frequency of the model is approximately 2 Hz , which is close to the approximate 1.92 Hz.

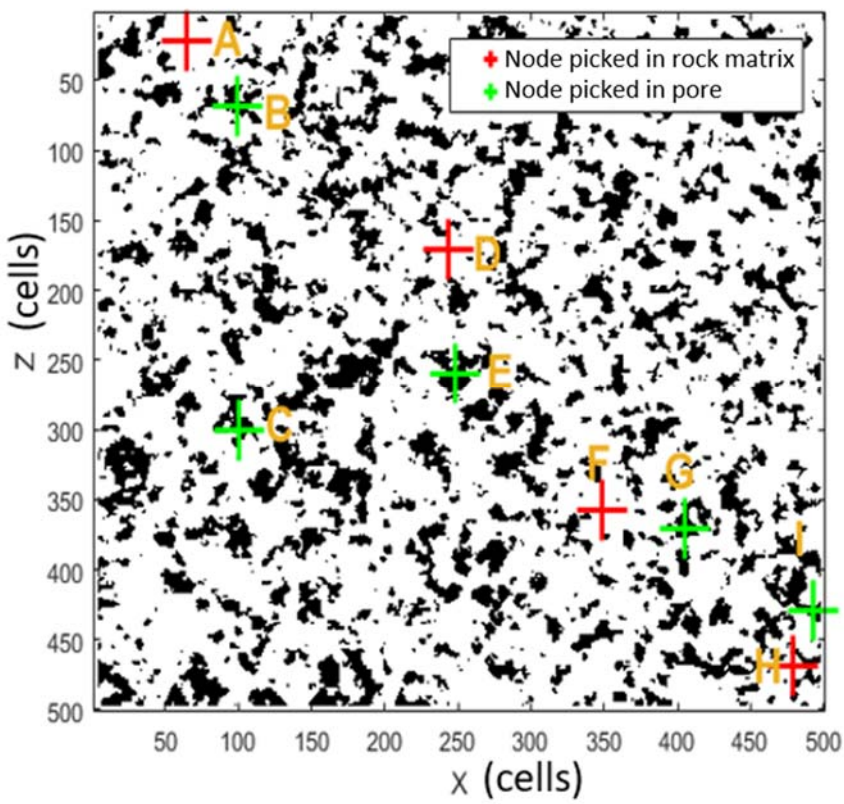

Figure 12. The numerical model of the 2D porous sandstone and its nine picked nodes. The black color represents pores and the white color represents matrix. The picked nodes are the crosses marked by letter A to I at different locations.

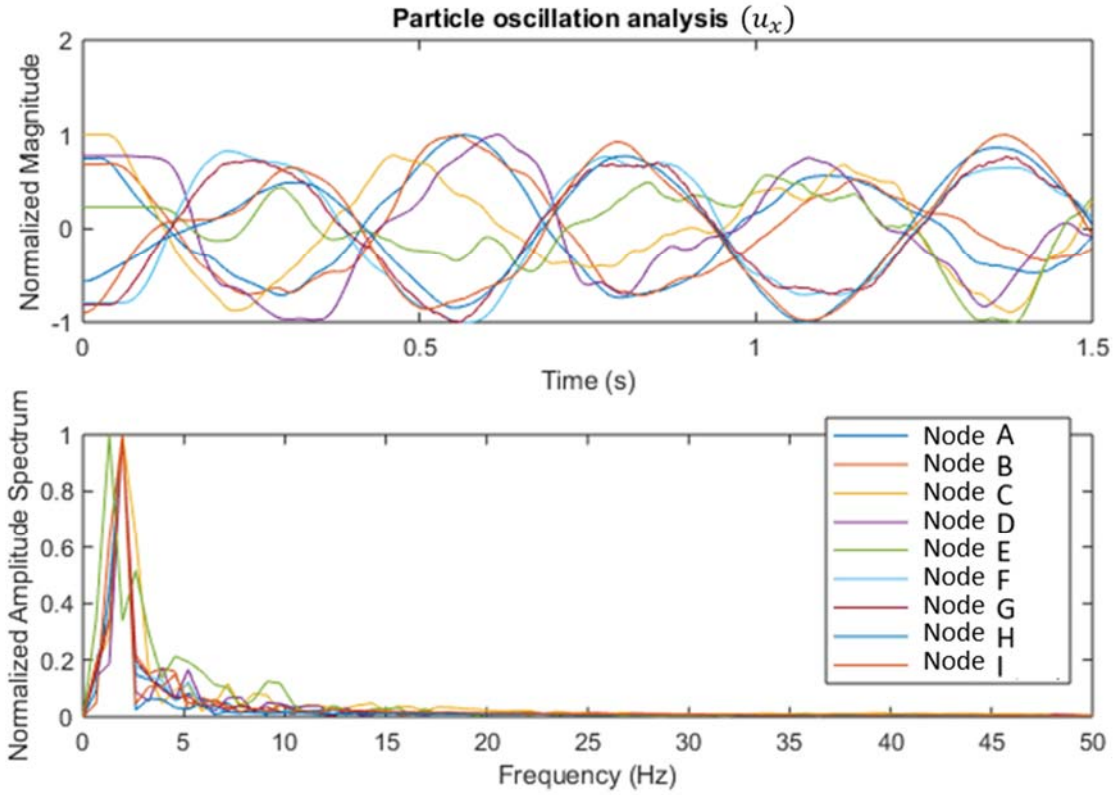

Figure 13. Displacements and the corresponding amplitude spectra at the chosen nodes in Figure 12. The top panel shows the displacement along x direction, the bottom panel shows the amplitude spectra.

3.5 Damping based on the viscoelastic attenuation theory

In Sections 3.1 to 3.3, I discussed how to add a constant damping parameter to the particle velocity term in the wave equation. In the following, I will discuss how to use the viscoelastic Q model, instead of simply adding a damping constant to the velocity term. I hope I can convince readers that adding damping to the elastodynamic equations will result in the same static solution, no matter what form the damping is in.

Liu et al., (1976) published the "standard linear solid" viscoelastic theory based upon a modification to Hooke's law to include the stress-rate and strain-rate terms:

$$\sigma + \tau_1 \dot{\sigma} = M_L(\varepsilon + \tau_2 \dot{\varepsilon}), \tag{29}$$

where (σ, ε) are stress and strain, and the dot (.) indicates the time derivative. M_L is the relaxed low-frequency limit of the modulus, (τ_1, τ_2) are relaxation times for stress and strain, respectively. The Second Law of Thermodynamics implies $\tau_1 < \tau_2$ (Liner, 2012).

Assuming that the material is isotropic, with Equation (22) and Equation (29), we can construct the 2D elastodynamic equations with viscous attenuation added:

$$\begin{cases} \frac{\partial v_x}{\partial t} = b\left(\frac{\partial \sigma_{xx}}{\partial x} + \frac{\partial \sigma_{xz}}{\partial z}\right) \\ \frac{\partial v_z}{\partial t} = b\left(\frac{\partial \sigma_{xz}}{\partial x} + \frac{\partial \sigma_{zz}}{\partial z}\right) \\ \frac{\partial u_x}{\partial t} = v_x \\ \frac{\partial u_z}{\partial t} = v_z \\ \tau_1 \frac{\partial \sigma_{xx}}{\partial t} = (\lambda + 2\mu)\left(\tau_2 \frac{\partial v_x}{\partial x} + \frac{\partial u_x}{\partial x}\right) + \lambda\left(\tau_2 \frac{\partial v_z}{\partial z} + \frac{\partial u_z}{\partial z}\right) - \sigma_{xx} \\ \tau_1 \frac{\partial \sigma_{zz}}{\partial t} = (\lambda + 2\mu)\left(\tau_2 \frac{\partial v_z}{\partial z} + \frac{\partial u_z}{\partial z}\right) + \lambda\left(\tau_2 \frac{\partial v_x}{\partial x} + \frac{\partial u_x}{\partial x}\right) - \sigma_{zz} \\ \tau_1 \frac{\partial \sigma_{xz}}{\partial t} = \mu\left(\tau_2 \frac{\partial v_x}{\partial z} + \tau_2 \frac{\partial v_z}{\partial x} + \frac{\partial u_x}{\partial z} + \frac{\partial u_z}{\partial x}\right) - \sigma_{xz} \end{cases}, \tag{30}$$

where b is the reciprocal of density, λ and μ are the low-frequency Lamé constants, v_x and v_z represent the velocity fields in the x and z directions, respectively. u_x and u_z represent the displacement fields in the x and z directions, respectively. σ_{xx} and σ_{zz} are normal stresses and σ_{xz} is the shear stress.

Equation (30) has all the time derivatives on the left side of the equations. Applying a time-marching finite difference scheme, we can numerically solve for the velocity, displacement and stress fields, given a certain model with boundary conditions. From the displacement fields, we can then get the strain fields.

Since we are targeting static stress-strain analysis, forces with a step function history will be prescribed on the model boundaries. They produce elastic deformations that contain both static and dynamic components. The static and dynamic elastic energy can be respectively characterized by the model's strain energy and kinetic energy (Aki and Richards, 1980) that evolve over time. The terms , τ_1 and τ_2 dictate how fast the kinetic energy dissipates. Furthermore, for a given model with certain boundary conditions, no matter what values are selected for τ_1 and τ_2, the final static stress-strain fields should be the same when the system reaches equilibrium.

To demonstrate how this method can give the static solutions of stresses and strains, I applied it to the same simple isotropic homogeneous 2D model used in Section 3.4. The model is a 200 m by 200 m homogeneous 2D model with P-wave velocity V_P=4382 m/s, S-wave velocity V_S=2530 m/s, and density ρ =3000 kg/m^3. Spatial steps in x and z directions are $\Delta x = \Delta z = 2\ m$, and the time step is $\Delta t = 0.15\ ms$. The model is prescribed with normal stresses $\sigma_{xx} = 1\ MPa$ and $\sigma_{zz} = 1\ MPa$ on all of its four boundaries at time zero. I used the staggered-grid finite difference method to do the numerical modeling of Equation (30).

In selection for the τ_1 and τ_2 values, it is not obvious what the lower and upper relaxation times should be. Liu et al., (1976) provided expressions for f_{peak} and Q_{peak}, which are related to

the characteristic times τ_1 and τ_2 (Equation (31) and Equation (32)). f_{peak} is the frequency with maximum attenuation, and Q_{peak} is the Q value for maximum attenuation. The relationship between τ_1, τ_2 and f_{peak}, Q_{peak} are :

$$f_{peak} = \frac{1}{2\pi\sqrt{\tau_1\,\tau_2}}, \tag{31}$$

$$Q_{peak} = \frac{2\sqrt{\tau_1\,\tau_2}}{\tau_2 - \tau_1}. \tag{32}$$

If we set a group of f_{peak} and Q_{peak}, we can derive the τ_1 and τ_2 from Equation (31) and Equation (32). The other reason that we should care about the Q_{peak} value is that attenuation is stronger if the Q value is smaller. Therefore a smaller Q_{peak} will make the system take less time to damp out the kinetic energy and reach equilibrium, which can speed up the modeling process.

I tested several groups of f_{peak} and Q_{peak} values to investigate their impacts on the number of times steps needed for the system to reach equilibrium. For the values assigned to f_{peak} and Q_{peak} , we do not investigate the physical meanings implied for the viscoelastic attenuation system. Instead, the values are just for numerical testing, making sense mathematically. I first randomly set f_{peak} =12 Hz, and tested Q_{peak} values of 1.185, 2 and 3, respectively. A comparison of the evolution of the total strain energy and kinetic energy in the system for different parameters were computed (Figure 14). The model is said to reach a static equilibrium when the strain energy converges to a stable value and the kinetic energy drops below

a certain small threshold. With f_{peak} fixed at 12 Hz, when using Q_{peak}=1.185, it damps out the kinetic energy with the least amount of time, with 2000 time steps. The other Q_{peak} values (bigger than 1.185) both took longer for the system to reach equilibrium. As expected, the strain energy converges to the same final value $2.552 \times 10^5\ J$ regardless of Q_{peak}. Also, the final strain energy is the same as the case when I used the constant damping method in Section 3.3 (Figure 10).

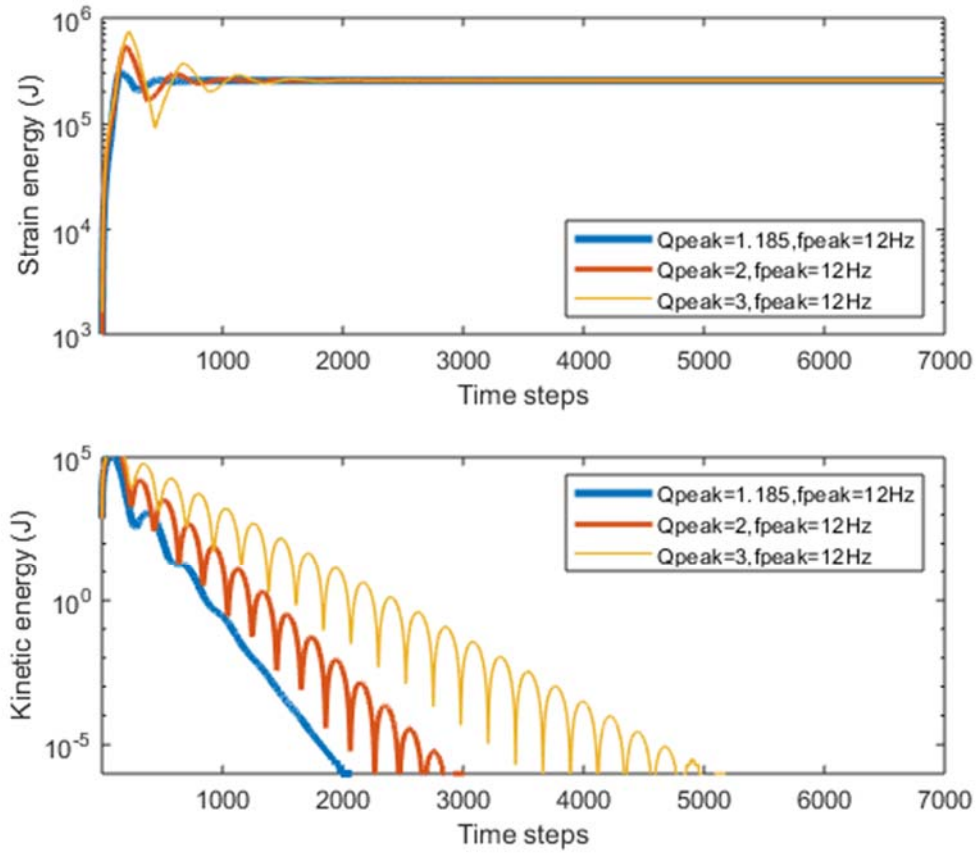

Figure 14. Strain and kinetic energy for the entire model versus the number of time steps for $f_{peak} = 12Hz$. The energy is displayed in the log scale. Here I set the equilibrium threshold for the kinetic energy as 10^{-6} J. The strain energy stabilizes at $2.552 \times 10^5\ J$ regardless of the Q_{peak} parameter.

Next, I set Q_{peak}=1.185 and tested different f_{peak} values. For the three f_{peak} values I tested (Figure 15), $f_{peak} = 18\ Hz$ took the least amount of time for the system to stabilize, with about 1400 time steps. While $f_{peak} = 9\ Hz$ took about 2800 time steps, $f_{peak} = 21\ Hz$ took about 1800 time steps, both slower than the case of $f_{peak} = 18\ Hz$. As expected, the strain energy converges to the same value $2.552 \times 10^5\ J$ regardless of what value the f_{peak} is, which is the

same final strain energy when I applied the constant damping method. One other thing to notice is that the least number of time steps achieved are both 1400 for this viscoelastic attenuation method and the constant damping method in Section 3.4 (see Figure 10).

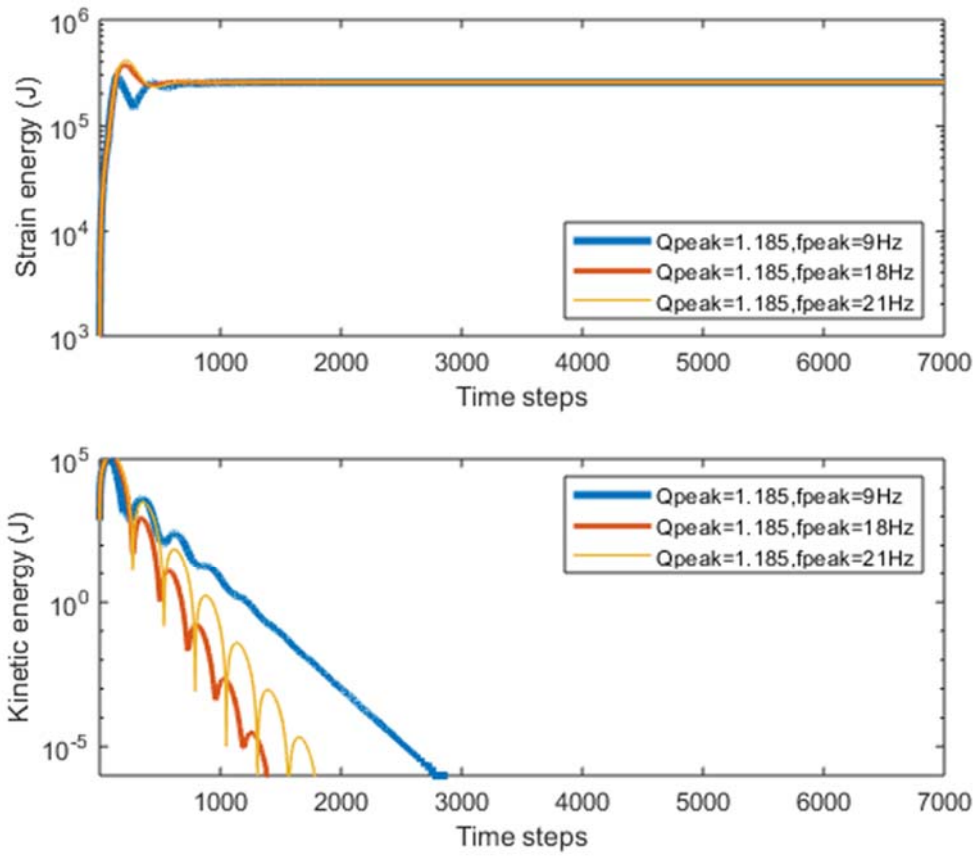

Figure 15. Strain and kinetic energy for the entire model versus the number of time steps for Q_{peak}=1.185. The energy is displayed in the log scale. Here I set the equilibrium threshold for the kinetic energy as 10^{-6} J. The strain energy stabilizes at $2.552 \times 10^5\ J$ regardless of the f_{peak} parameter.

In summary, this viscoelastic attenuation finite difference method works equally effectively as the constant damping finite difference method. Both methods can get the same static stress-strain solutions from the elastodynamic equations effectively given proper damping/attenuation parameters are set. They both have their own advantages. The damping constant finite difference method has advantages such as its form is simpler than the viscoelastic finite difference method, with only one damping parameter. Also, the constant damping parameter is easier to set, with its physical relation to the standing waves. However, the advantage of the viscoelastic finite difference method is that it is from a physical point of view, unlike the velocity damping method.

CHAPTER 4 VERIFICATION WITH ANALYTICAL MODELS

In Chapter 3, I introduced two methods of modeling static stress-strain fields from elastodynamic equations: the constant velocity damping method and the viscoelastic model. From this chapter on, I will focus on the velocity damping method, for its simplicity and friendly parameter-setting. In later chapters (Chapter 4-7), the constant damping method will be referred to as the damped finite difference method.

In this chapter, I will show that the damped finite difference method can get the same static stress-strain solutions as the analytical solutions. The examples I used include a homogeneous isotropic model, a circular borehole model, a laminated model, and the Hashin and Shtrikman model. For all of these models, the numerical modeling results showed excellent agreement with the analytical solutions.

4.1 Homogeneous and isotropic models

I began with an isotropic homogeneous 2D model (Figure 8) that was also discussed in Section 3.3. The model size is $200\ m$ by $200\ m$ with a P-wave velocity $V_P = 4382\ m/s$, S-wave velocity $V_s = 2530\ m/s$, and density $\rho = 3000\ kg/m^3$. Based on these parameters, one can get the shear modulus $\mu = \rho V_S^2 = 19.2027\ GPa$, and the first Lamé parameter $\lambda = \rho V_p^2 - 2\mu = 19.2004\ GPa$, The spatial step sizes in x and z directions are $\Delta x = \Delta z = 2\ m$, and the time step

is $\Delta t = 0.15\ s$. In the following modeling, the damping parameter $D = 0.0206$ was used the same as in Section 3.4.1.

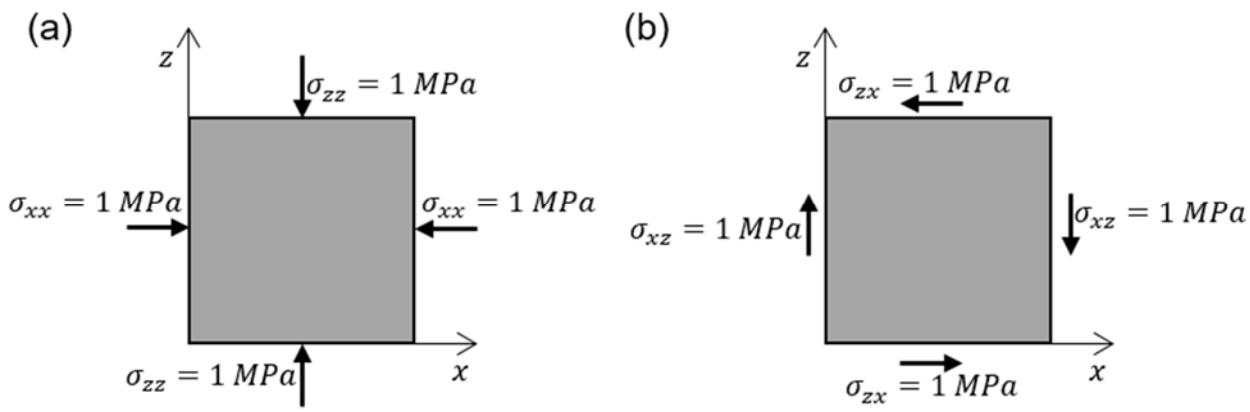

Figure 16. Two scenarios of boundary conditions applied to the 2D model.

To get the effective medium Lamé parameters (the first Lamé parameter λ and the shear modulus μ), based on Hooke's law:

$$\begin{cases} \sigma_{xx}=(\lambda+2\mu)\varepsilon_{xx}+\lambda\varepsilon_{zz} \\ \sigma_{zz}=(\lambda+2\mu)\varepsilon_{zz}+\lambda\varepsilon_{xx}, \\ \sigma_{xz}=2\mu\varepsilon_{xz} \end{cases} \tag{33}$$

one needs the static stress-strain relationships under two scenarios of boundary conditions: the model under only normal stresses (Figure 16(a)) and the model under only shear stresses (Figure 16(b)). Take the first scenario as an example, I firstly prescribed the model with normal stresses $\sigma_{zz} = 1\ MPa$ on top and bottom boundaries and $\sigma_{xx} = 1\ MPa$ on left and right boundaries (Figure 16(a)). Then I computed the stress fields and the particle velocity fields using the damped finite difference method. Finally, I time integrated the particle velocity fields to obtain the

displacement fields $\boldsymbol{u}$, and the corresponding strain field was calculated using Equations (34) to (36):

$$\varepsilon_{xx} = \frac{\partial u_x}{\partial x}, \tag{34}$$

$$\varepsilon_{zz} = \frac{\partial u_z}{\partial z}, \tag{35}$$

$$\varepsilon_{xz} = \frac{1}{2}\left(\frac{\partial u_x}{\partial z} + \frac{\partial u_z}{\partial x}\right), \tag{36}$$

where ε_{xx} and ε_{zz} are normal strains, ε_{xz} is the shear strain.In the above equations, u_x is the displacement along the x direction, $and\ u_z$ is the displacement along the z direction.

4.1.1 Surface average and volume average

Since the model is treated as a whole for the effective medium moduli calculation, the stresses and strains need to be averaged in the model. We consider two types of averaging methods: volume average and surface average. In 3D cases, an arithmetic average over each node in the model is referred to as the volume average. For example, by averaging the strain ε_{xz} of each node in the model we get the volume-averaged ε_{xz}. On the other hand, treating the whole model as one voxel and taking into consideration of only values on the model surfaces is referred to as the surface average. For example, surface-averaged ε_{zz} for the model is calculated as:

$$\varepsilon_{zz} = \frac{u_z^{bottom} - u_z^{top}}{L}, \tag{37}$$

where u_z^{bottom} is the displacement u_z on the lower boundary of z direction, and u_z^{top} is the displacement u_z on the upper boundary of z direction, L is the distance from upper boundary to the lower boundary of z (See Figure 17 (b) for a 2d illustration).

The concept of surface average comes from the physical test of real rocks. In a physical test on a real rock, the stress is applied externally, and the deformation is measured also on the exterior surface. For example, in an effectively homogeneous model, the effective bulk modulus K can be measured from the surface average of compressional stress/strain for a cubic sample with edge L as:

$$K_{Surf} = -p\left\langle \frac{normal\ displacement}{L} \right\rangle_{surf}^{-1}, \tag{38}$$

where p is the applied pressure, and $\langle \quad \rangle_{surf}$ indicates a result obtained from surface average. Similarly, the shear modulus μ can be measured from the surface average of shear stress/strain as:

$$\mu_{Surf} = \tau_{shear}\left\langle \frac{shear\ displacement}{L} \right\rangle_{surf}^{-1}, \tag{39}$$

where τ_{shear} is the applied shear stress.

However, for the same model, the effective bulk modulus K can also be calculated as:

$$K_{Vol} = -\frac{\langle pressure \rangle_{vol}}{\langle dilatation \rangle_{vol}}, \tag{40}$$

where $\langle \quad \rangle_{vol}$ indicates an average over the volume. Similarly, the shear modulus may be calculated as:

$$\mu_{Vol} = \frac{\langle shear\ stress \rangle_{vol}}{\langle shear\ strain \rangle_{vol}}, \tag{41}$$

These volume averages are different in principle from the surface averages. However, both of these two averages are theoretically correct. In the special case of homogeneous and isotropic models, the stresses and strains are independent of spatial coordinates, the value obtained from the volume average should be equal to that from the surface average. If the volume-averaged stress or strain is different from the surface-averaged, it means the model is not homogeneous and isotropic. In the following 2D models, to keep consistency in terminology, I still use volume average although it should be area average, and surface average although it is actually edge average.

One needs to take special handling of boundary values when staggered grids are used in the modeling. In the staggered grid finite difference shown in Figure 6 and Figure 7, the particle velocity fields are not aligned with the model boundaries. For example, the particle velocity field v_z is off the z-direction boundaries of the model by half a grid. Therefore in the 3D case, the bottom slice (for the 2D case, the bottom line) of the v_z field is outside of the bottom boundary of the model and should be fixed to be zero in the damped finite difference modeling. Since displacement is the time integral of velocity, the bottom slice of the displacement field u_z is also

zero. In summary, when one uses the volume average and surface average to calculate the effective medium moduli, the zero-valued boundaries need to be excluded. In the following figures, the zero-valued boundaries are removed.

4.1.2 Calculation of effective medium moduli for a 2D model

To obtain the displacement fields u_x and u_z, I did time integration for the particle velocity fields v_x and v_z. The final displacement fields for the first set of boundary condition (Figure 16(a)) are shown in Figure 17.

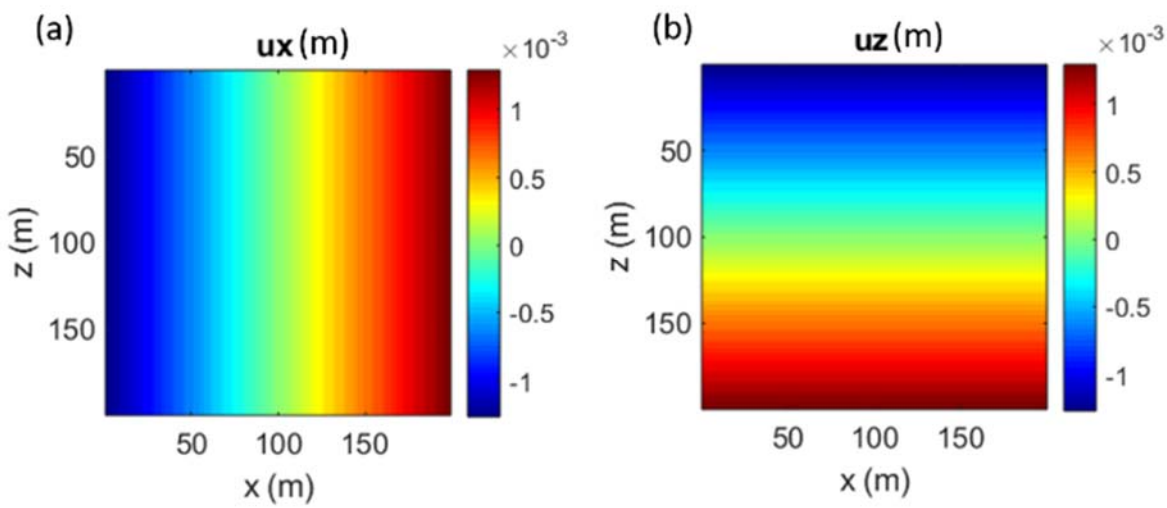

Figure 17. Displacement fields for the 2D homogeneous model when normal stresses were applied. Spatial distribution of horizontal displacement u_x (a) and vertical displacement u_z (b) when static equilibrium was reached. The model was applied with normal stresses on the four boundaries.

Observing Figure 17, the displacement u_x is linear along the x direction, and the displacement u_z is linear along the z direction. Both displacements ranged from -0.001289 to

$0.001289\ m$. The effective model edge length was 99 grids or $198\ m$. Based on Equation (34) and Equation (35), the surface-averaged normal strains for this 2D model were:

$$\varepsilon_{xx} = \varepsilon_{zz} = \frac{0.001289-(-0.001289)m}{198m} = 1.302\text{e-}5.$$

Since the displacements were linear in space, the volume-averaged strains were identical to the surface-averaged strains. At the equilibrium state, each grid point had the same stress as the boundary points. The normal stresses σ_{xx} and σ_{zz} were $1\ MPa$ and the shear stress was $0\ Pa$.

The first set of boundary conditions shown in Figure 16(a) calculated the normal strain under normal stress for deriving the effective bulk modulus. To obtain the shear modulus, I need the static shear strain under the second set of boundary conditions by applying constant shear stress σ_{xz}=1 MPa on all its four boundaries (Figure 16(b)). From the displacement fields for the shear case (Figure 18), I obtained $u_x$and u_z both ranging from -0.002552 to $0.002552\ m$. The effective model edge length was 98 grids or $196\ m$. According to Equation (36), The surface-averaged shear strain for this 2D model was:

$$\varepsilon_{xz} = \frac{1}{2}\left(\frac{0.002552-(-0.002552)}{196} + \frac{0.002552-(-0.00252)}{196}\right) = 2.604 \times 10^{-5}.$$

Since the displacements were linear in space, the volume-averaged strains were identical to the surface-averaged strains.

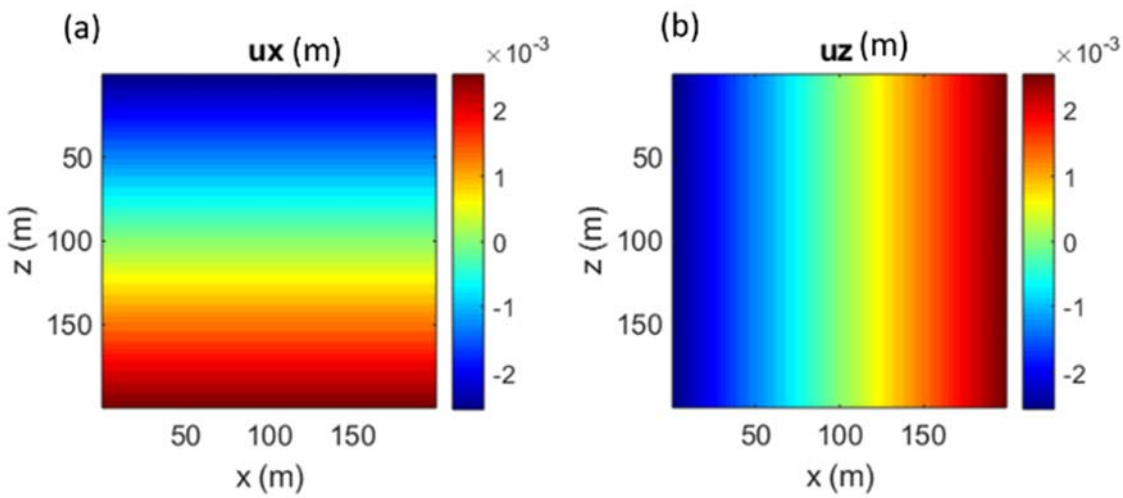

Figure 18. Displacement fields for the 2D homogeneous model when shear stresses were applied. Spatial distribution of horizontal displacement u_x (a) and vertical displacement u_z (b) when static equilibrium was reached. The model was applied with constant shear stresses on the four boundaries.

Based on the isotropic Hooke's law for the 2D case (Equation (33)), one can get shear modulus $\mu = 19.2012\ GPa$, and the first Lamé parameter $\lambda = 19.2012\ GPa$. The differences between the calculated elastic moduli and the input moduli were within 0.08%.

4.1.3 3D model effective medium moduli calculation

To verify the damped finite difference method for 3D models, I extended the 2D model to a 100×100×100 grid cube and kept all the other parameters (rock physics properties, spatial steps, time step, and damping parameter) unchanged. I then numerically computed the effective Young's modulus E along with the effective bulk modulus K, and compared them with the theoretical values.

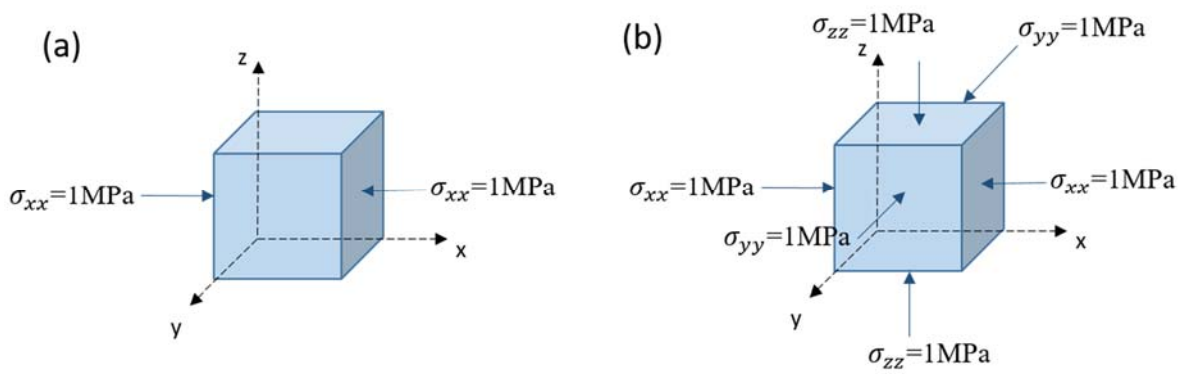

Figure 19. Illustrations showing the two cases of applied stresses for the measurements of E and K. (a) The stress $\sigma_{xx} = 1\ MPa$ was applied on each x direction model boundary surface for measuring the Young's modulus E; (b) The stresses $\sigma_{xx} = \sigma_{yy} = \sigma_{zz} = 1\ MPa$ were applied on the model boundaries for measuring the bulk modulus K.

To simulate the static measurement of Young's modulus E in the lab, I applied the normal stress $\sigma_{xx} = 1\ MPa$ on the two boundary surfaces perpendicular to the x axis while keeping the other boundary surfaces as free surfaces (Figure 19(a)). The displacement fields u_x, u_y and u_z calculated from the damped finite difference method are displayed in Figure 20. The volume-averaged strains I got from the damped finite difference method were $\varepsilon_{xx} = 2.0830656 \times 10^{-5}$, $\varepsilon_{zz} = \varepsilon_{yy} = -5.2073485 \times 10^{-5}$. Again, since the model was isotropic and homogeneous, the volume-averaged strains were equal to the surface-averaged strains. Young's modulus is defined as the ratio of axial stress to axial strain in a uniaxial stress state. Therefore the Young's modulus from my numerical modeling was $E = \sigma_{xx}/\varepsilon_{xx} = 48.0061684\ GPa$.

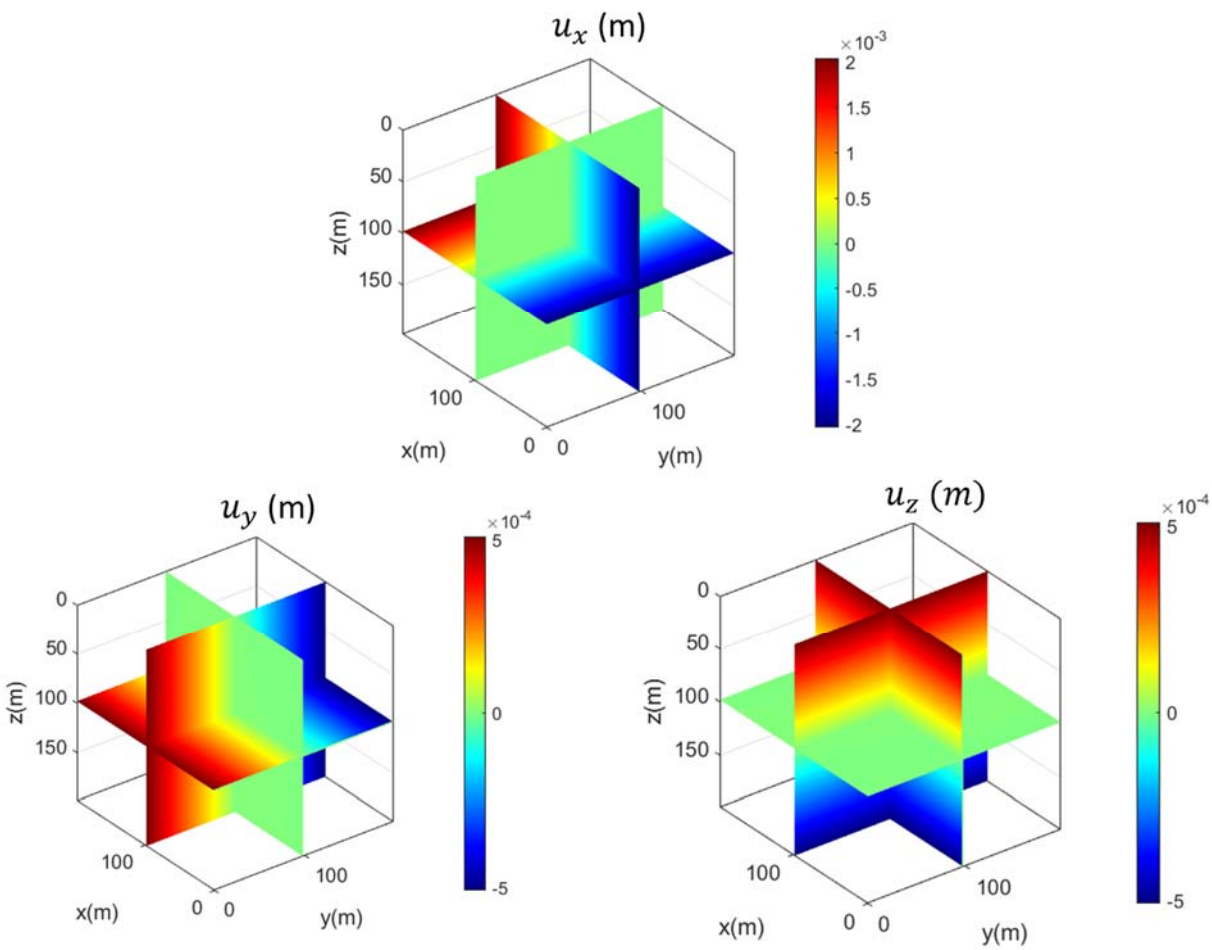

Figure 20. The displacement fields from applying the boundary condition of $\sigma_{xx} = 1\ MPa$.

To simulate the static measurement of bulk modulus K in the lab, I applied the boundary conditions with normal stresses $\sigma_{xx} = \sigma_{yy} = \sigma_{zz} = 1\ MPa$, and shear stresses $\sigma_{xy} = \sigma_{xz} = \sigma_{yz} = 0\ MPa$ on the corresponding six boundary surfaces (Figure 19(b)). The displacement fields u_x, u_y and u_z calculated from the damped finite difference method are displayed in Figure 21. The volume-averaged strains I got from the damped finite difference method were $\varepsilon_{xx} = \varepsilon_{zz} =$

$\varepsilon_{yy} = 1.041596 \times 10^{-5}$. The bulk modulus is defined as applied pressure divided by the relative deformation, therefore, according to Equation (42):

$$K = \frac{1}{3}(\sigma_{xx} + \sigma_{yy} + \sigma_{zz})/(\varepsilon_{xx} + \varepsilon_{yy} + \varepsilon_{zz}), \tag{42}$$

the bulk modulus from my numerical modeling was 32.0021715 GPa.

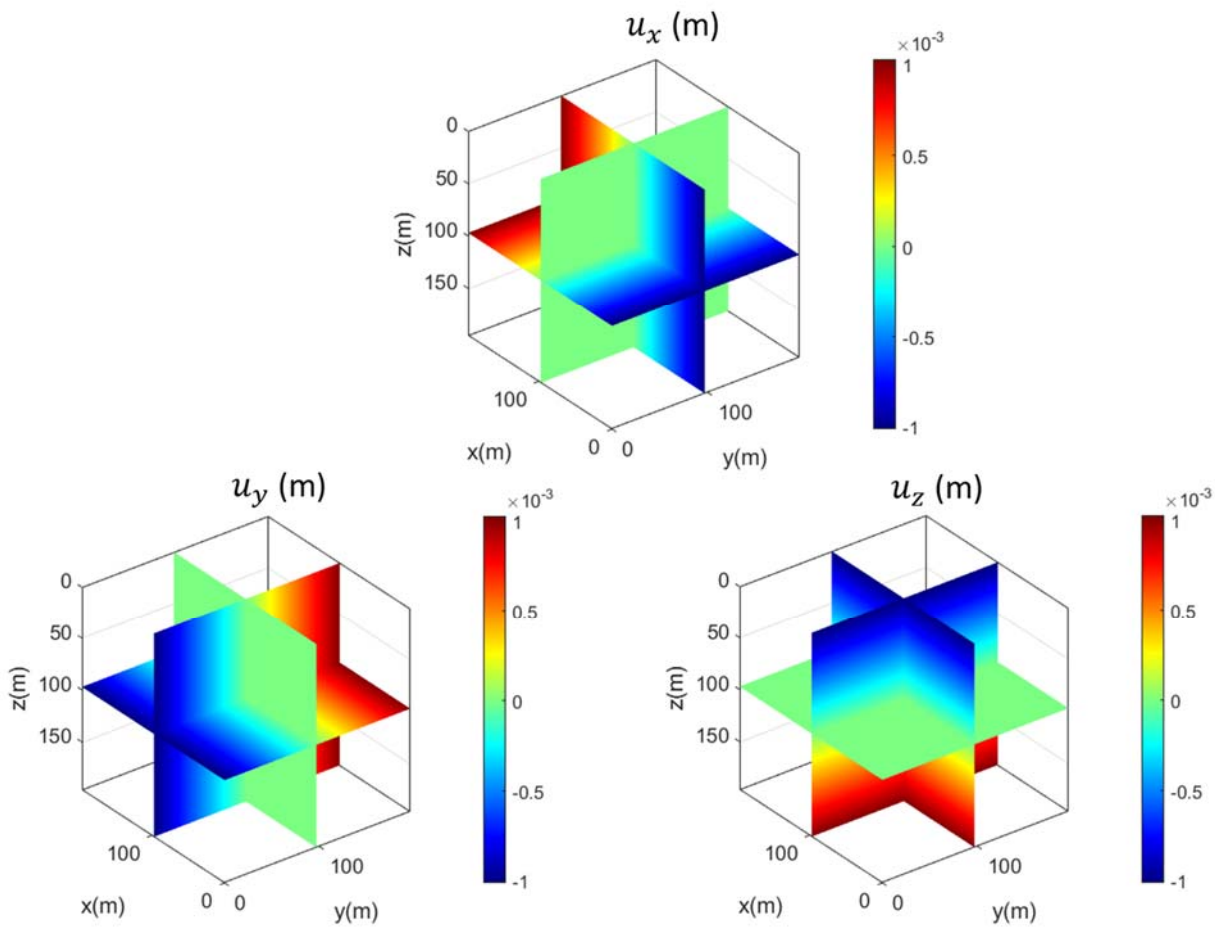

Figure 21. The displacement fields from applying the boundary condition of $\sigma_{xx} = \sigma_{yy} = \sigma_{zz} = 1\ MPa$.

Based on the P-wave and S-wave velocities and densities of the true model, I calculated that the P-wave modulus was $M = \rho V_P^2 = 57.605772\ GPa$, and the shear modulus was $G = \rho V_s^2 = 19.2027\ GPa$. With the relationship that

$$E = \frac{G(3M - 4G)}{M - G}, \tag{43}$$

$$K = M - \frac{4}{3}G, \tag{44}$$

one could get the Young's modulus $E = 48.006168\ GPa$, and the bulk modulus $K = 32.002172\ GPa$. The close match between the elastic moduli calculated from the numerical modeling and the analytical calculation again proves the validity of the damped finite difference method.

4.2 Circular borehole model

In this section, I compared the analytical stress fields on the cross-sectional plane of a circular borehole, with those modeled from the damped finite difference method. The stresses on the cross-sectional plane of a circular borehole (Figure 22) under the compression of far-field stresses and internal fluid pressure can be expressed as (Fjaer, 2008):

$$\sigma_r = \frac{\sigma_H + \sigma_h}{2}\left(1 - \frac{R_w^2}{r^2}\right) + \frac{\sigma_H - \sigma_h}{2}\left(1 + 3\frac{R_w^4}{r^4} - 4\frac{R_w^2}{r^2}\right)cos2\theta + P_w\frac{R_w^2}{r^2}, \tag{45}$$

$$\sigma_\theta = \frac{\sigma_H + \sigma_h}{2}\left(1 + \frac{R_w^2}{r^2}\right) - \frac{\sigma_H - \sigma_h}{2}\left(1 + 3\frac{R_w^4}{r^4}\right)cos2\theta - P_w\frac{R_w^2}{r^2}, \tag{46}$$

$$\tau_{r\theta} = -\frac{\sigma_H - \sigma_h}{2}\left(1 - 3\frac{R_w^4}{r^4} + 2\frac{R_w^2}{r^2}\right)sin2\theta, \tag{47}$$

where σ_r and σ_θ are radial and tangential normal stresses, respectively; $\tau_{r\theta}$ is the shear stress; σ_H and σ_h respectively represent the far-field maximum and minimum horizontal stresses; R_w is the borehole radius; P_w is the borehole fluid pressure; r represents the distance measured from the borehole center; θ is the azimuth angle measured counter-clockwise from the x-axis.

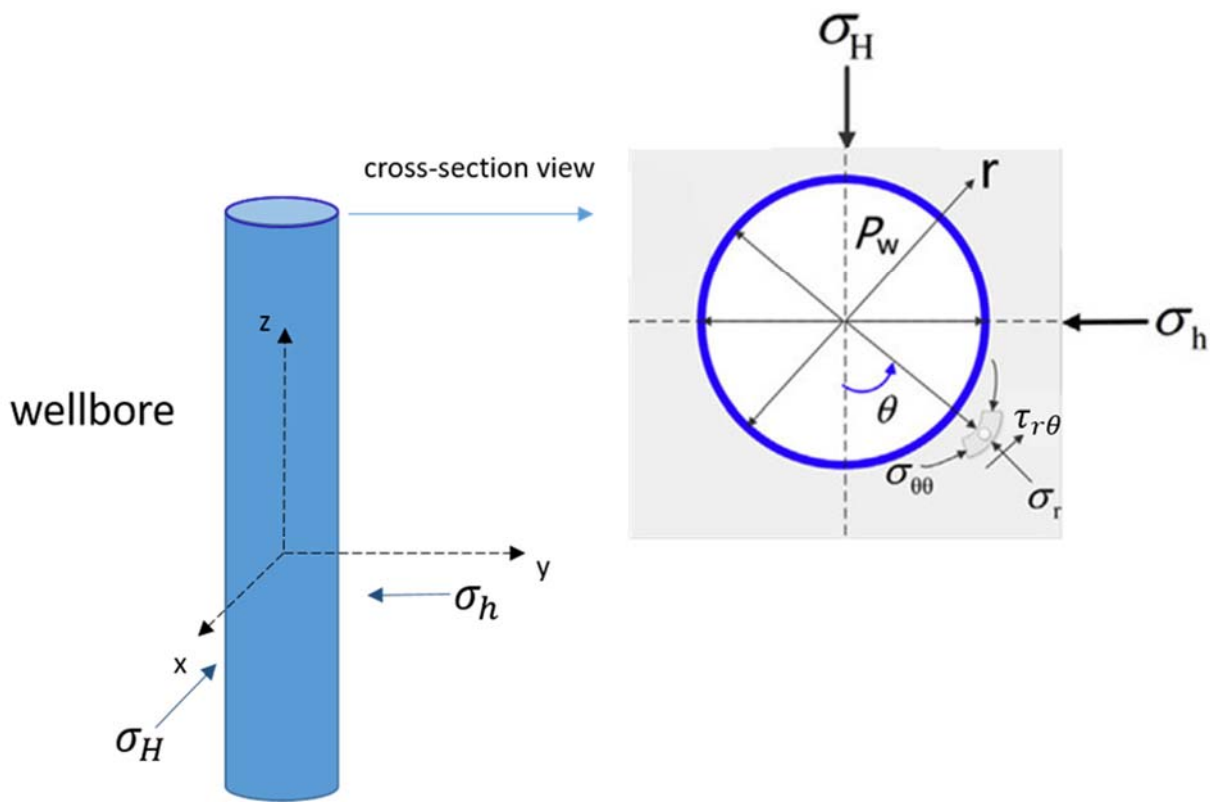

Figure 22. Circular borehole stresses in polar coordinates (Adapted from (Liu et al., 2018) Fig.2).

To compare with the analytical solutions which are given in polar coordinates, the coordinate conversion is needed. The following equations were used to convert the results calculated from the damped finite difference method from Cartesian coordinates (x, y) to cylindrical polar coordinates stresses σ_r , σ_θ and $\tau_{r\theta}$:

$$\sigma_r = \frac{1}{2}(\sigma_x + \sigma_y) + \frac{1}{2}(\sigma_x - \sigma_y)cos2\theta + \tau_{xy}sin2\theta \ , \tag{48}$$

$$\sigma_\theta = \frac{1}{2}(\sigma_x + \sigma_y) - \frac{1}{2}(\sigma_x - \sigma_y)cos2\theta - \tau_{xy}sin2\theta \ , \tag{49}$$

$$\tau_{r\theta} = \frac{1}{2}(\sigma_y - \sigma_x)sin2\theta + \tau_{xy}cos2\theta. \tag{50}$$

I used a 10 m by 10 m square model with a wellbore of radius 10 cm in the center of the model. Then I set the maximum horizontal stress σ_H and minimal horizontal stress σ_h in the region 40 MPa and 30 MPa respectively.The borehole fluid pressure P_w is 20 MPa. The normal and shear stress fields calculated by the analytical solution (Equation (45) to (50)) are displayed in panel (a) of Figure 23 to Figure 25.

To apply the damped finite difference modeling, I firstly assigned the borehole fluid pressure to the area within the wellbore, making $\sigma_x = P_w$ and $\sigma_y = P_w$ in the wellbore area of the 10 m by 10 m model. Then I assumed the model boundaries were at an infinite far distance and prescribed the four model boundaries with $\sigma_x = \sigma_H$ and $\sigma_y = \sigma_h$. I ran the finite difference modeling with parameters $\Delta x = \Delta z = 0.4\ cm$, and $\Delta t = 6 \times 10^{-7}\ s$. The P-wave velocity $V_P = 1500\ m/s$, the S-wave velocity $V_S = 0\ m/s$ and the density $\rho = 1000\ kg/m^3$ were assigned to the grid points inside the wellbore, and the P-wave velocity $V_P = 4382\ m/s$, the S-wave velocity $V_S = 2530\ m/s$ and the density $\rho = 3000\ kg/m^3$ were given to the grid points outside of the wellbore. Damping parameter $D = 0.0017$ was obtained using Equation (27). The normal and shear stress fields calculated by the damped finite difference method are displayed in panel (b) of Figure 23 to Figure 25.

Panel (c) of Figure 23 to Figure 25 shows the relative difference between the analytical result and the damped finite difference result for different stress components. The difference was calculated as $\Delta d = (A - B)/A$, where A represents the analytical result and B represents the damped finite difference results. It is observed that the damped finite difference modeling results on stress calculation match well with the analytical results with maximum relative difference Δd less than 1%, which might be regarded as the numerical error.

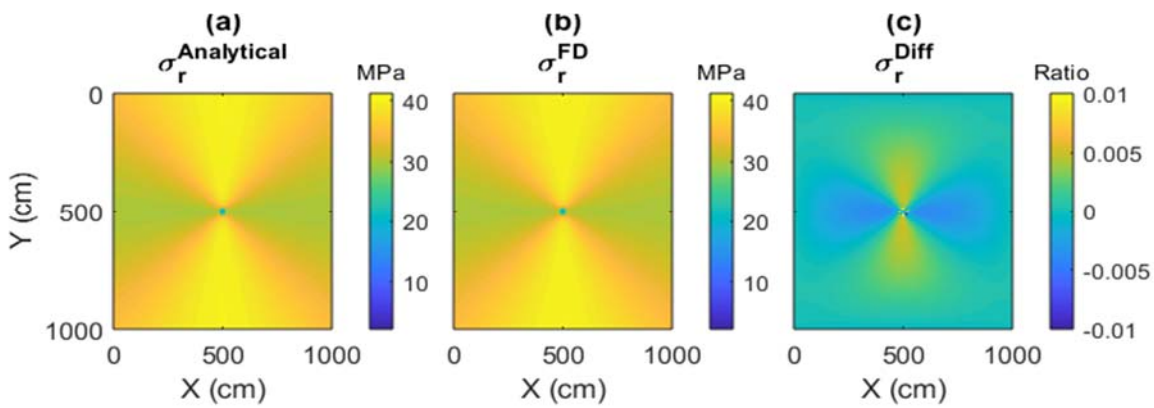

Figure 23. Comparison of the radial normal stress fields obtained by the analytical and the finite difference method. (a) σ_r calculated from the analytical solution and (b) the finite difference method as well as (c) the corresponding relative difference.

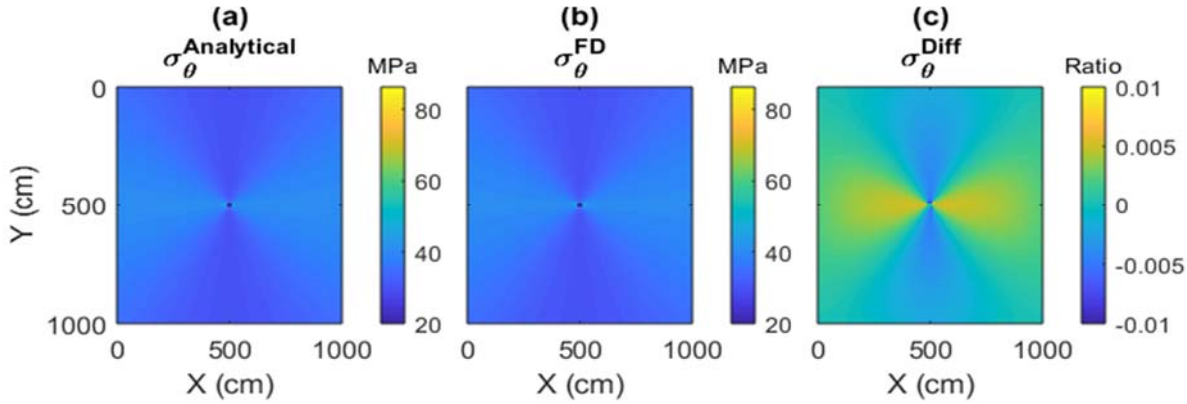

Figure 24. Comparison of the tangential normal stress fields obtained by the analytical and the finite difference method. (a) σ_θ calculated from the analytical solution and (b) the finite difference method as well as (c) the corresponding relative difference.

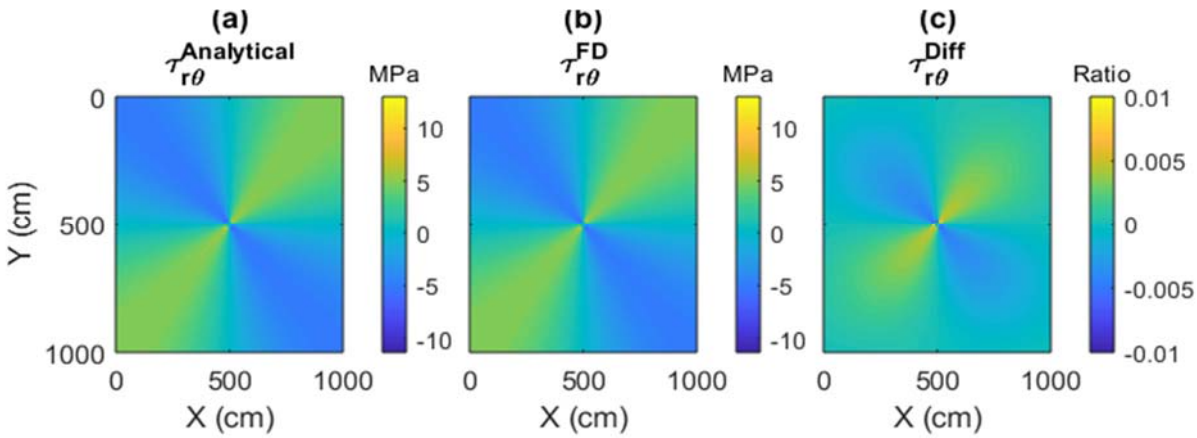

Figure 25. Comparison of the shear stress fields obtained by the analytical and the finite difference method. (a) $\tau_{r\theta}$ calculated from the analytical solution and (b) the finite difference method as well as (c) the corresponding relative difference.

4.3 A laminated model in 3D space

A laminated model (Figure 26) that consists of a thin-layered sequence of dolomite and shale was used to verify the applicability of the proposed damped finite difference method for static stress-strain modeling and effective moduli estimation. The properties of dolomite and shale are as follows (Mavko et al., 2020):

Dolomite: $V_P = 5200$ *m/s*, $V_S = 2700$ *m/s*, $\rho = 2450$ *kg/m*^{3};

Shale: $V_P = 2900$ *m/s*, $V_S = 1400$ *m/s*, $\rho = 2340$ *kg/m*^{3}.

I use the model of a 3D cube with an edge length of 100 grids in each dimension. Each thin bed of dolomite or shale took 1 grid thickness and occupies 50% of the total volume. The spatial steps in x, y and z directions were $\Delta x = \Delta y = \Delta z = 1\ m$, and the time step was $\Delta t = 0.075\ ms$. The primary damping parameter chosen for this model was $D = 0.01$, based on Equation (26) and Equation (27).

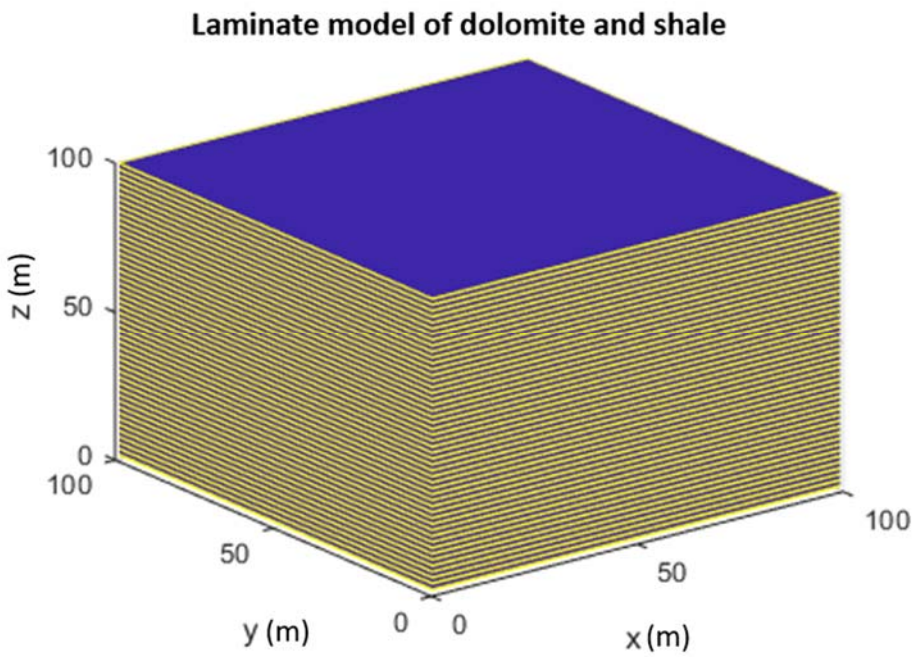

Figure 26. A laminate model for a thin-layered sequence of 50% dolomite and 50% shale. The blue color indicates dolomite and the yellow indicates shale.

The laminated structure results in transverse isotropy with the effective stiffness tensor given analytically as (Backus, 1962):

$$\begin{bmatrix} A & B & F & 0 & 0 & 0 \\ B & A & F & 0 & 0 & 0 \\ F & F & C & 0 & 0 & 0 \\ 0 & 0 & 0 & E & 0 & 0 \\ 0 & 0 & 0 & 0 & E & 0 \\ 0 & 0 & 0 & 0 & 0 & M \end{bmatrix}, \tag{51}$$

with

$$\begin{gathered} A = \langle 4\rho V_s^2 \left(1 - \frac{V_S^2}{V_p^2}\right)\rangle + \langle 1 - 2\frac{V_S^2}{V_p^2}\rangle^2 \langle \left(\rho V_p^2\right)^{-1}\rangle^{-1}, \\ B = \langle 2\rho V_s^2 (1 - \frac{2V_S^2}{V_p^2})\rangle + \langle 1 - 2\frac{V_S^2}{V_p^2}\rangle^2 \langle (\rho V_p^2)^{-1}\rangle^{-1}, \\ C = \langle (\rho V_p^2)^{-1}\rangle^{-1}, \\ E = \langle (\rho V_s^2)^{-1}\rangle^{-1}, \\ F = \langle 1 - 2\frac{V_S^2}{V_p^2}\rangle \langle \left(\rho V_p^2\right)^{-1}\rangle^{-1}, \\ M = \langle \rho V_s^2 \rangle, \\ B = A - 2M, \end{gathered} \tag{52}$$

where the brackets ⟨ ⟩ represent volume averaging of the properties weighted by their volume fractions, which are both 0.5 for dolomite and shale. The laminated model (Figure 26) used in the modeling contained 50 horizontal layers of dolomite-shale interbeds.

Using the damped finite difference method, I computed the stress ($\boldsymbol{\sigma}$) and strain ($\boldsymbol{\varepsilon}$) tensors at each grid in the model. Then I used Hooke's law to find the elastic moduli A, M, C, E, and F:

$$\begin{bmatrix} \sigma_{xx} \\ \sigma_{yy} \\ \sigma_{zz} \\ \sigma_{yz} \\ \sigma_{xz} \\ \sigma_{xy} \end{bmatrix} = \begin{bmatrix} A & A-2M & F & 0 & 0 & 0 \\ A-2M & A & F & 0 & 0 & 0 \\ F & F & C & 0 & 0 & 0 \\ 0 & 0 & 0 & E & 0 & 0 \\ 0 & 0 & 0 & 0 & E & 0 \\ 0 & 0 & 0 & 0 & 0 & M \end{bmatrix} \begin{bmatrix} \varepsilon_{xx} \\ \varepsilon_{yy} \\ \varepsilon_{zz} \\ \varepsilon_{yz} \\ \varepsilon_{xz} \\ \varepsilon_{xy} \end{bmatrix}. \tag{53}$$

When solving for the elastic moduli with the damped finite difference method, two modelings were taken using two sets of the different boundary conditions to solve Equation (53):

(1) with the boundary conditions $\sigma_{xx} = \sigma_{yy} = \sigma_{zz} = \sigma_{xy} = \sigma_{xz} = \sigma_{yz} = 1\ MPa$, the volume-averaged strains I obtained from the damped finite difference method were $\varepsilon_{xx} = 1.1603 \times 10^{-5}$, $\varepsilon_{zz} = 2.1510 \times 10^{-5}$, $\varepsilon_{yy} = 1.1603 \times 10^{-5}$, $\varepsilon_{yz} = 1.3702 \times 10^{-4}$, $\varepsilon_{xy} = 8.9524 \times 10^{-5}$, and $\varepsilon_{xz} = 1.3702 \times 10^{-4}$. The volume-averaged stresses were of the same value as the boundary conditions.

(2) with the boundary conditions $\sigma_{xx} = \sigma_{xy} = \sigma_{xz} = \sigma_{yz} = 1\ MPa$, $\sigma_{zz} = 3\ MPa$, $\sigma_{yy} = 2\ MPa$, the volume-averaged strains I got from the damped finite difference method were $\varepsilon_{xx} = -2.2313 \times 10^{-5}$, $\varepsilon_{zz} = 9.9310 \times 10^{-5}$, $\varepsilon_{yy} = 2.2569 \times 10^{-5}$, $\varepsilon_{yz} = 1.37023 \times 10^{-4}$, $\varepsilon_{xy} = 8.9524 \times 10^{-5}$, and $\varepsilon_{xz} = 1.3703 \times 10^{-4}$. The volume-averaged stresses were of the same value as the boundary conditions.

Using the stresses and strains modeled from the damped finite difference method, I solved for Equation (53) and obtained $A = 40.3200\ GPa$, $M = 11.1640\ GPa$, $F = 15.0320\ GPa$, $C =$

$30.1744\ GPa$ and $E = 7.2985\ GPa$. Comparing the numerical results with the Backus average (Backus, 1962) results: $A = 40.6300\ GPa$, $M = 11.2235\ GPa$, $F = 15.0917\ GPa$, $C = 30.3450\ GPa$ and $E = 7.2986\ GPa$, I found that the relative errors are between 0.001% to 0.76%, which again proves the validity of the damped finite difference method.

4.3.1 The edge effect

The stiffness tensor I got from the modeling of the laminated model matches well with the analytical predictions. However, the relative error was larger than that of the homogeneous and isotropic model case. This section investigated the origin of such an error.

To begin with, I plotted the stress and strain fields from the modeling case (1), with the boundary conditions $\sigma_{xx} = \sigma_{yy} = \sigma_{zz} = \sigma_{xy} = \sigma_{xz} = \sigma_{yz} = 1\ MPa$ applied. Observing from Figure 27 to Figure 30, the edge effects on the stress, strain and displacement gradient fields were obvious. For example, the σ_{zz} in Figure 27, the ε_{xx} and ε_{yy} in Figure 29, and the displacement gradients $\partial u_y/\partial$x and $\partial u_x/\partial$y in Figure 30 . The edge effects on the displacement gradients directly affect the accurate calculation of the strains according to Equation (54):

$$\begin{cases} \varepsilon_{xx} = \dfrac{\partial u_x}{\partial x} \\ \varepsilon_{zz} = \dfrac{\partial u_z}{\partial z} \\ \varepsilon_{yy} = \dfrac{\partial u_y}{\partial y} \\ \varepsilon_{xz} = \dfrac{1}{2}\left(\dfrac{\partial u_x}{\partial z} + \dfrac{\partial u_z}{\partial x}\right) \\ \varepsilon_{xy} = \dfrac{1}{2}\left(\dfrac{\partial u_x}{\partial y} + \dfrac{\partial u_y}{\partial x}\right) \\ \varepsilon_{yz} = \dfrac{1}{2}\left(\dfrac{\partial u_y}{\partial z} + \dfrac{\partial u_z}{\partial y}\right) \end{cases}. \tag{54}$$

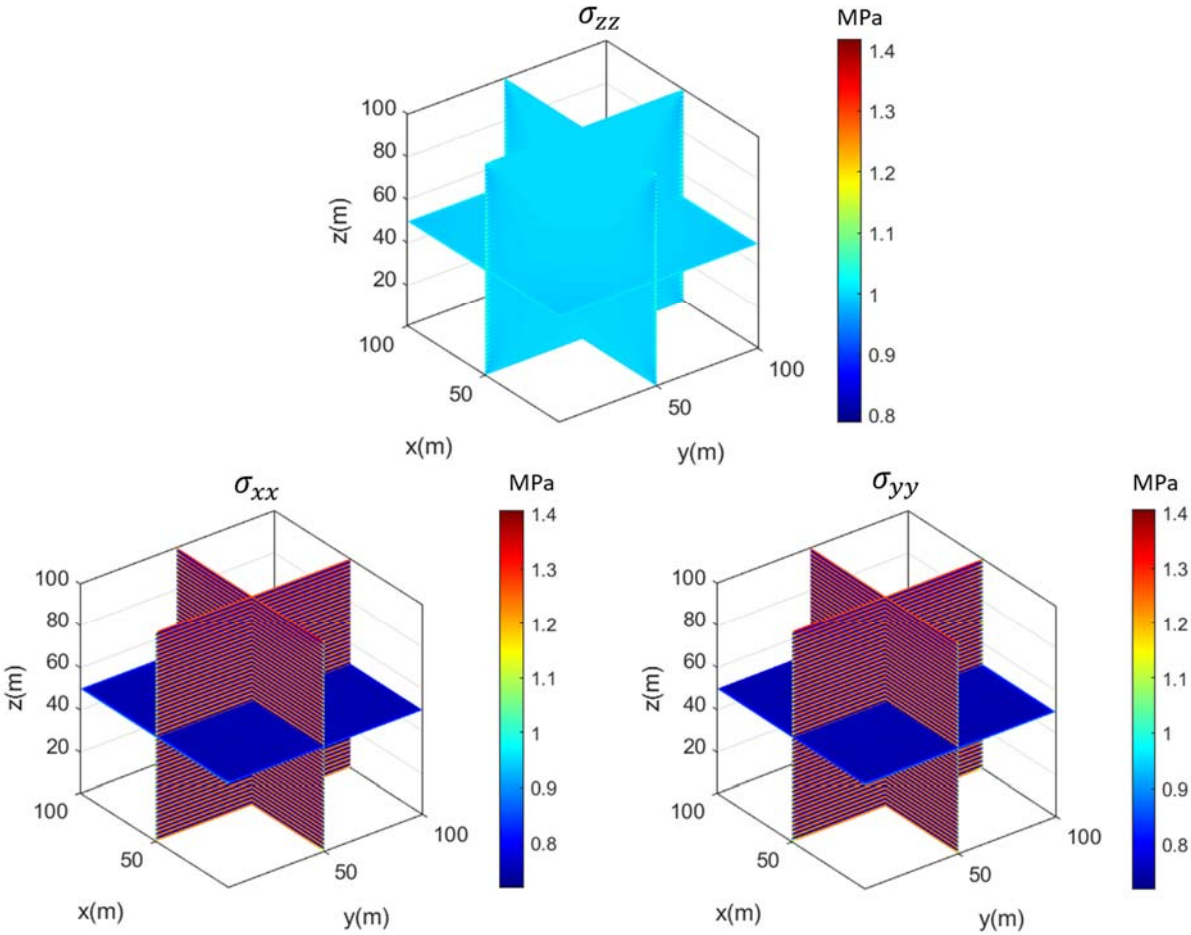

Figure 27. Normal stress fields for the laminated model.

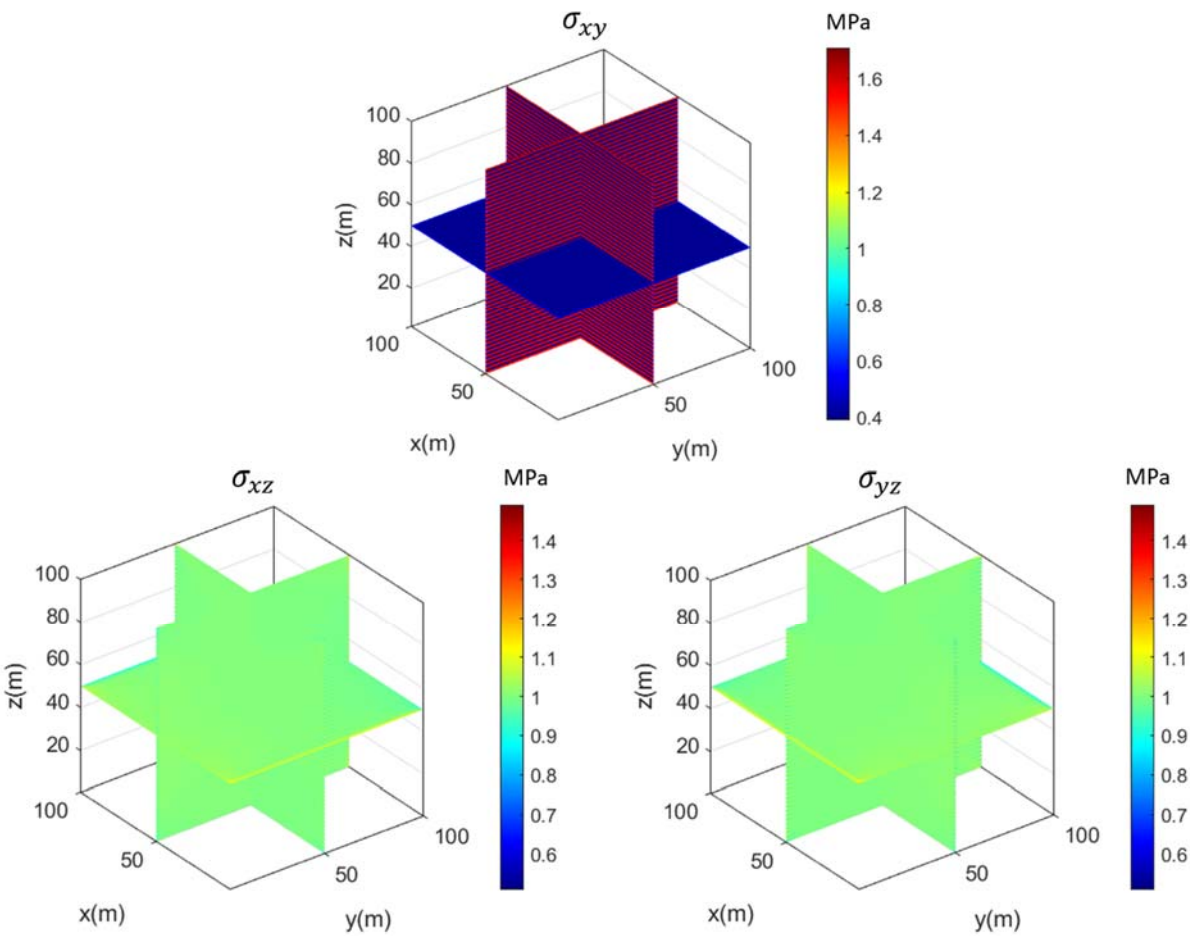

Figure 28. Shear stress fields for the laminated model.

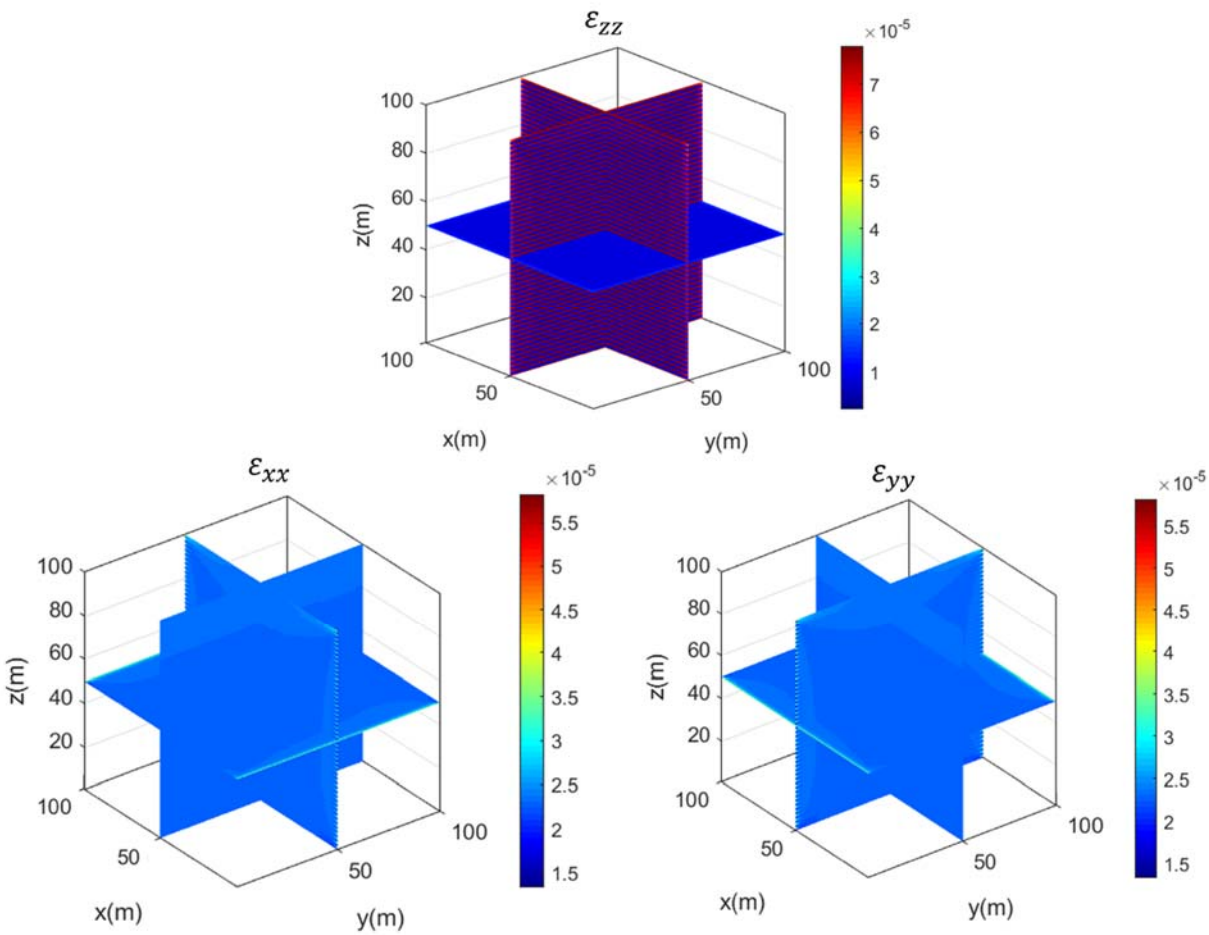

Figure 29. Normal strain fields for the laminated model.

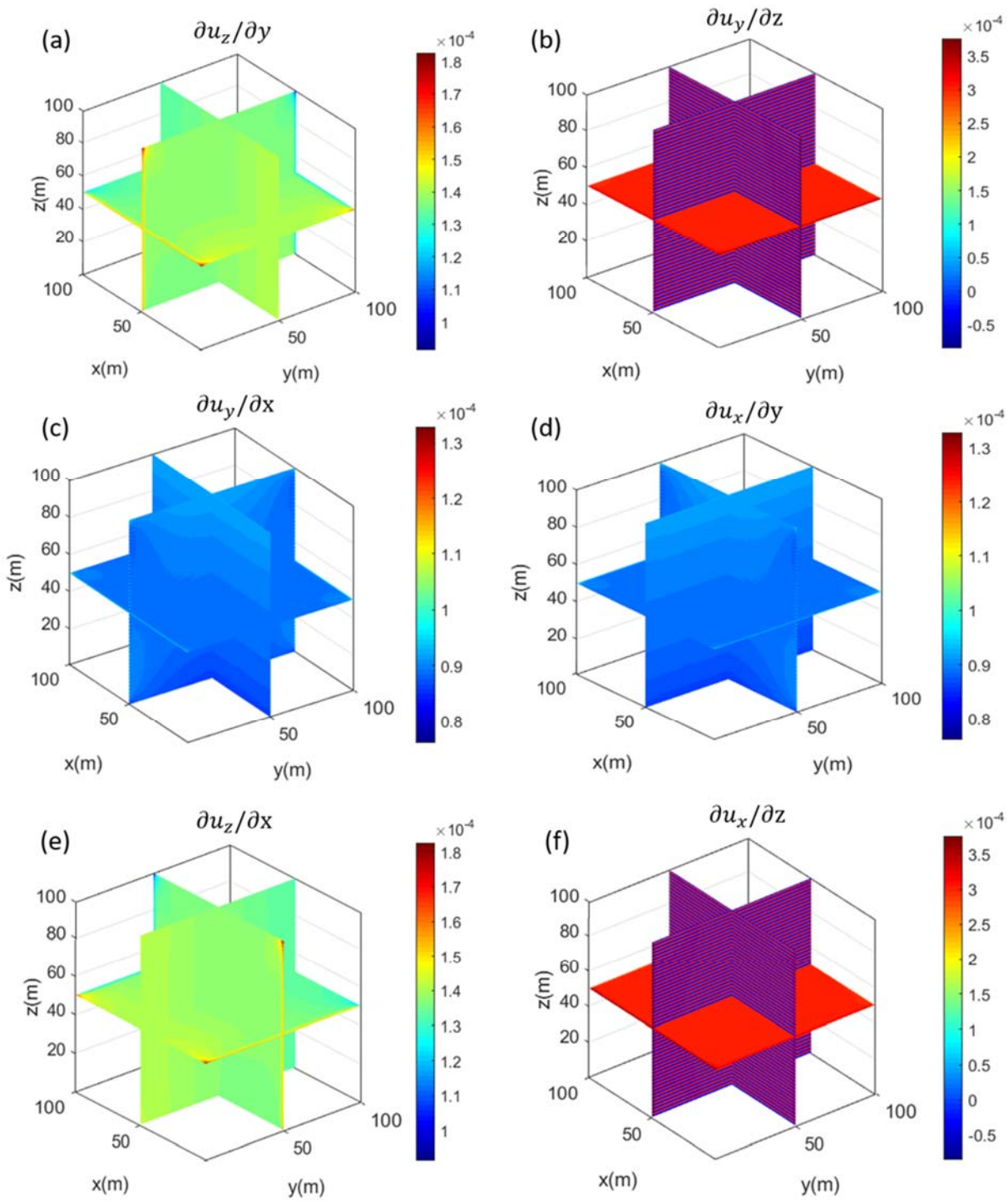

Figure 30. Displacement gradients used in the calculation of shear strains.

Since Backus' average implicitly assumes an infinite lateral extent, the edge effects might well explain the larger relative errors observed in the laminated modeling case. To mitigate the edge effects, I excluded the region close to the boundary surfaces and calculated the effective moduli using only the inner part of the stress and strain fields (used only the middle 40×40×40 grid area). The calculated moduli were much closer to Backus' average results and the experiment concluded my hypothesis of the edge effects. In this case, the volume-averaged stresses and strains were:

In modeling (1), the innermost volume-averaged strains were $\varepsilon_{xx} = 1.1434 \times 10^{-5}$, $\varepsilon_{zz} = 2.1559 \times 10^{-5}$, $\varepsilon_{yy} = 1.1434 \times 10^{-5}$, $\varepsilon_{yz} = 1.3705 \times 10^{-4}$, $\varepsilon_{xy} = 8.9088 \times 10^{-5}$, $\varepsilon_{xz} = 1.3705 \times 10^{-4}$; the innermost volume-averaged stresses were $\sigma_{xx} = 9.9778 \times 10^{5}\ Pa$, $\sigma_{zz} = 9.9920 \times 10^{5}\ Pa$, $\sigma_{yy} = 9.9778 \times 10^{5}\ Pa$, $\sigma_{yz} = 1.0005 \times 10^{6}\ Pa$, $\sigma_{xy} = 9.9951 \times 10^{5}\ Pa$, $\sigma_{xz} = 1.0005 \times 10^{6}\ Pa$.

In modeling (2), the innermost volume-averaged strains were $\varepsilon_{xx} = -2.1963 \times 10^{-5}$, $\varepsilon_{zz} = 9.8675 \times 10^{-5}$, $\varepsilon_{yy} = 2.2361 \times 10^{-5}$, $\varepsilon_{yz} = 1.3705 \times 10^{-4}$, $\varepsilon_{xy} = 8.9090 \times 10^{-5}$, $\varepsilon_{xz} = 1.3705 \times 10^{-4}$; the innermost volume-averaged stresses were $\sigma_{xx} = 1.0036 \times 10^{6}\ Pa$, $\sigma_{zz} = 3.0003 \times 10^{6}\ Pa$, $\sigma_{yy} = 1.9983 \times 10^{6}\ Pa$, $\sigma_{yz} = 1.0005 \times 10^{6}\ Pa$, $\sigma_{xy} = 9.9951 \times 10^{5}\ Pa$, $\sigma_{xz} = 1.0005 \times 10^{6}\ Pa$.

Using these stresses and strains, I solved for Equation (53) and obtained $A = 40.6227\ GPa$, $M = 11.2196\ GPa$, $F = 15.0921\ GPa$, $C = 30.3446\ GPa$ and $E = 7.3005\ GPa$. The errors compared with the Backus' average were much reduced than when I used the whole

model's stresses and strains in the effective medium moduli calculation. Two tables showing the different results from these two approaches are displayed below (Table 1 and Table 2).

Stresses and Strains	The first modeling		The second modeling	
	Using the whole volume	Using the center volume	Using the whole volume	Using the center volume
σ_{xx}	$1 \times 10^6\ Pa$	$9.9978 \times 10^5\ Pa$	$1 \times 10^6\ Pa$	$1.0036 \times 10^6\ Pa$
σ_{yy}	$1 \times 10^6\ Pa$	$9.9920 \times 10^5\ Pa$	$2 \times 10^6\ Pa$	$3.0003 \times 10^6\ Pa$
σ_{zz}	$1 \times 10^6\ Pa$	$9.9978 \times 10^5\ Pa$	$3 \times 10^6\ Pa$	$1.9983 \times 10^6\ Pa$
σ_{xy}	$1 \times 10^6\ Pa$	$1.0005 \times 10^6\ Pa$	$1 \times 10^6\ Pa$	$1.0005 \times 10^6\ Pa$
σ_{xz}	$1 \times 10^6\ Pa$	$9.9951 \times 10^5\ Pa$	$1 \times 10^6\ Pa$	$9.9951 \times 10^5\ Pa$
σ_{yz}	$1 \times 10^6\ Pa$	$1.0005 \times 10^6\ Pa$	$1 \times 10^6\ Pa$	$1.0005 \times 10^6\ Pa$
ε_{xx}	1.1603×10^{-5}	1.1434×10^{-5}	-2.2313×10^{-5}	-2.1963×10^{-5}
ε_{zz}	2.1510×10^{-5}	2.1559×10^{-5}	9.9310×10^{-5}	9.8675×10^{-5}
ε_{yy}	1.1603×10^{-5}	1.1434×10^{-5}	2.2569×10^{-5}	2.2361×10^{-5}
ε_{yz}	1.3702×10^{-4}	1.3705×10^{-4}	1.37023×10^{-4}	1.3705×10^{-4}
ε_{xy}	8.9524×10^{-5}	8.9088×10^{-5}	8.9524×10^{-5}	8.9090×10^{-5}
ε_{xz}	1.3702×10^{-4}	1.3705×10^{-4}	1.3703×10^{-4}	1.3705×10^{-4}

Table 1. Modeling results comparison from different approaches for the laminated model.

Elastic constants (unit: GPa)	Calculated using the whole volume	Calculated using the center volume	Backus's average prediction
A	40.3200	40.6227	40.6300
M	11.1640	11.2196	11.2235
F	15.0320	15.0921	15.0917
C	30.1744	30.3446	30.3450
E	7.2985	7.3005	7.2986

Table 2. Elastic constants calculated from different approaches.

Besides the solution of excluding the edges in the calculation of effective medium, another solution is to use periodic boundary conditions instead of the prescribed boundary conditions of constant stresses. To be specific, one can use periodic boundary conditions in the x and y directions, to mimic an infinite extension of the model on lateral directions. The implementation of the periodic boundary conditions is out of the scope of this dissertation, therefore it is not discussed here.

4.4 Hashin - Shtrikman model

The overall elasticity of a realistic rock is, in general, not theoretically calculable because the microgeometry is so complicated. Instead, theoretical upper and lower bounds on the bulk elastic moduli have been proposed, such as the strict bounds on the overall elasticity derived by Hashin and Shtrikman (Hashin and Shtrikman, 1961). In the section, I developed two special cases, the

"K-test" and the "μ -test" from the Hashin-Shtrikman bounds to verify the damped finite difference method.

4.4.1 The "K-test" and the "μ-test"

For solid composites of two isotropic constituents (with bulk moduli K_i and shear moduli μ_i and volume fractions f_i), the lower (−) and upper (+) H–S (Hashin - Shtrikman) bounds for the bulk modulus K and the shear modulus μ are

$$K_- \equiv K_1 + \frac{f_2}{\dfrac{1}{K_2 - K_1} + \dfrac{f_1}{K_1 + 4\mu_1/3}} \leq K \leq K_2 + \frac{f_1}{\dfrac{1}{K_1 - K_2} + \dfrac{f_2}{K_2 + 4\mu_2/3}} \equiv K_+, \tag{55}$$

$$\mu_- \equiv \mu_1 + \frac{f_2}{\dfrac{1}{\mu_2 - \mu_1} + \dfrac{f_1}{H_1}} \leq \mu \leq \mu_2 + \frac{f_1}{\dfrac{1}{\mu_1 - \mu_2} + \dfrac{f_2}{H_2}} \equiv \mu_+ \tag{56}$$

In Equation (56), the combination of moduli

$$H_i = \frac{5\mu_i(K_i + 4\mu_i/3)}{2(K_i + 2\mu_i)}, \tag{57}$$

for each constituent appears in the bounds for the shear modulus. Here, it is assumed (following Equation (55)) that $K_1 \leq K_2$ and also that $\mu_1 \leq \mu_2$; this correlation is common. If it should happen that $K_1 \geq K_2$ while $\mu_1 \leq \mu_2$, then the roles of K_+ and K_-, defined in Equation (55), are reversed. If it should happen that $K_1 \leq K_2$ while $\mu_1 \geq \mu_2$, then the roles of μ_+ and μ_-, defined in Equation (56), are reversed. The bounds on the bulk modulus (Equation (55)) may be combined to show the difference:

$$K_+ - K_- = \frac{4 f_1 f_2 \left(\Delta K\right)^2}{3\left(K_1 + 4\mu_1/3 + f_1 \Delta K\right)\left(K_2 + 4\mu_2/3 - f_2 \Delta K\right)} \Delta\mu \quad , \tag{58}$$

where $\Delta K \equiv K_2 - K_1$ and $\Delta\mu \equiv \mu_2 - \mu_1$. Hence, the bounds on K coincide exactly in the special case where the two minerals have identical shear modulus ($\Delta\mu = 0$), in which case the bulk modulus is given exactly by

$$K_{HS} \equiv K_-^* = K_+^* = \frac{(4 f_1 K_1 \mu + 4 f_2 K_2 \mu + 3 K_2 K_1)}{(3 f_1 K_2 + 3 f_2 K_1 + 4\mu)} \quad , \tag{59}$$

where μ is the common shear modulus, of the two constituents and the aggregate for any random microgeometry of the two isotropic constituents.

The generalization of Equation (55) for composites of more than two isotropic constituents was given by Hashin and Shtrikman (Hashin and Shtrikman, 1961). For such composites, the upper and lower bounds on *K* coincide, yielding a unique result, if the shear moduli are equal for all constituents. Of course, few if any physical aggregates have constituents with identical shear moduli. However, although Equation (59) is not a useful result for physical aggregates, it is a very useful result for numerical analyses, since it poses a necessary criterion for the validity of any digital rock physics numerical algorithm when equal isotropic shear moduli are assigned to the grains; this may be called the "*K*-test".

Similarly, the bounds on the shear modulus in Equation (56) may be combined to show the difference:

$$\mu_+^* - \mu_-^* = \frac{f_1 f_2 (\Delta\mu)^2}{(H_1 + f_1\Delta\mu)(H_2 - f_2\Delta\mu)}\left[H_2 - H_1 - \Delta\mu\right] . \tag{60}$$

Hence, the bounds on the shear moduli coincide exactly, in the special case when:

$$H_2 - \mu_2 = H_1 - \mu_1 . \tag{61}$$

For composites of more than two isotropic constituents, the upper and lower bounds on μ coincide, yielding a unique result, if the condition of Equation (61) holds for all constituents. The condition of Equation (61) serves as a calculation of any one of the four constituent moduli, when the other three are specified. For example, it implies that

$$K_2 = \frac{4\mu_2(H_1 - \mu_1 - 2\mu_2/3)}{(3\mu_2 - 2H_1 + 2\mu_1))} . \tag{62}$$

For composites of two constituents which confirm Equation (61), the shear modulus is given exactly by

$$\mu_{HS} = \mu_- = \mu_+ = \frac{f_1\mu_1 H_2 + f_2\mu_2 H_1}{f_1 H_1 + f_2 H_2} , \tag{63}$$

independent of the microgeometry of the two isotropic constituents. Of course, few if any physical aggregates have constituents which confirm Equation (61). However, although Equation (62) and Equation (63) are not a useful result for physical aggregates, they are a very useful result for numerical analyses, since they pose another necessary criterion for the validity of any digital rock physics numerical algorithm; this may be called the "μ -test".

4.4.2 Validation on non-porous rocks

The Hashin–Shtrikman (H-S) tests were applied to the damped finite difference algorithm. To avoid problems caused by mismatches between the numerical grid and the model grid, the calculation was performed for the model shown in Figure 31, with cubic grains. The model was a $50 \times 50 \times 50$ cube, with a spatial step of $2\ m$. In the model, the cells were randomly assigned to one or another of two isotropic constituents. The two grains were of 50%/50% mix. Although the model is inhomogeneous, it can be treated as an effectively homogeneous medium and apply the H-S test.

The spatial step in x, y and z directions were $\Delta x = \Delta y = \Delta z = 2\ m$, and the time step was $\Delta t = 0.15\ ms$. For the H–S "K-test", the elastic parameters were set as K_1 = 13.564 GPa, K_2 = 8.564 GPa, μ_1 = μ_2 = 4.586 GPa, f_1 = f_2 = 0.5. In terms of velocities and density, they were:

Material 1: $V_P = 2900$ *m/s*, $V_S = 1400$ *m/s*, $\rho = 2340$ *kg/m*^{3};

Material 2: $V_P = 2750.7$ *m/s*, $V_S = 1537.6$ *m/s*, $\rho = 1940$ *kg/m*^{3}.

The primary damping parameter I used for this model was $D = 0.026$.

Although this is not a realistic model, with this geometry, any inaccuracies in the calculation can be attributed to other features of the algorithm. To ensure uniform application of external stress, the model shown was surrounded by a uniform jacket (four cells thick) with the properties of water (for applied pressure) or of an average solid (for applied shear stress).

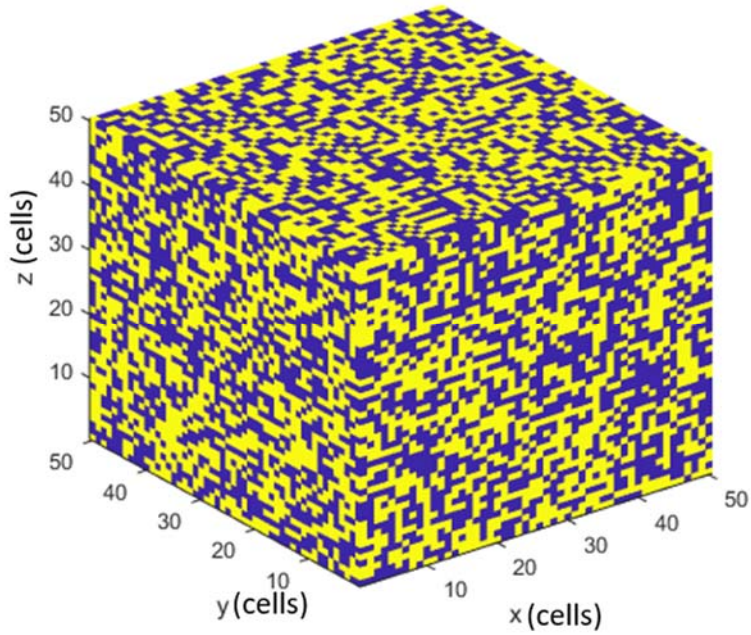

Figure 31. A model with cubic grains of two isotropic constituents, randomly distributed. The two grains were of 50%/50% mix. The boundaries of the grains were exactly aligned with the Cartesian numerical grid (50 × 50 × 50 cells) so that the contents within each cell were uniform.

For this model, the theoretical H–S value from Equation (59) is K_{HS} = 10.700 GPa. The modeling of the effective bulk modulus was conducted through prescribing all the boundaries with $\sigma_{xx} = \sigma_{yy} = \sigma_{zz} = 1\ MPa$. The displacement fields, strain fields and the stress fields from the damped finite difference modeling are displayed below in Figure 32.

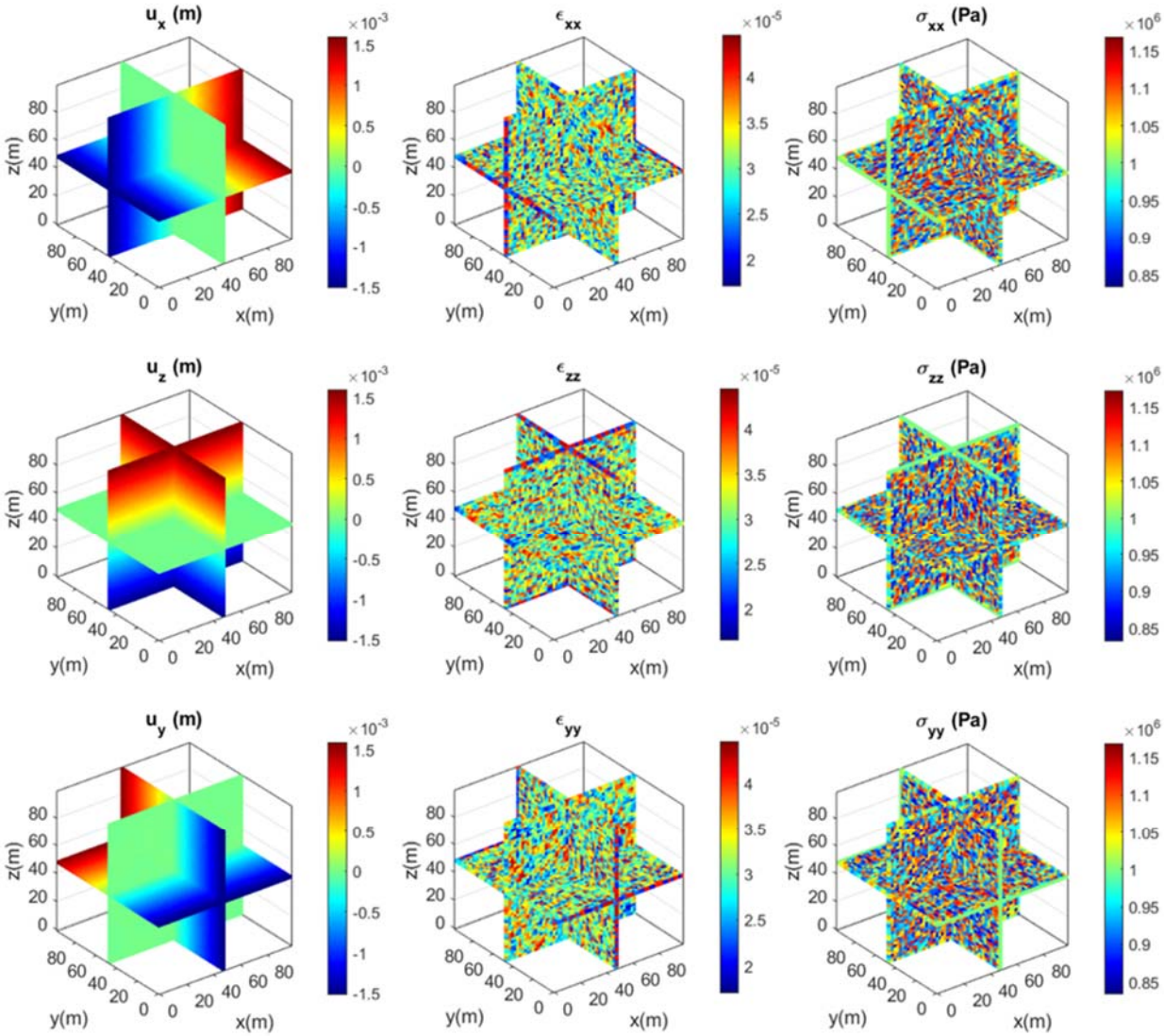

Figure 32. Displacement, strain, and stress fields from the modeling of bulk modulus for the nonporous model displayed in Figure 31.

The volume-averaged normal strains were $\varepsilon_{xx} = \varepsilon_{zz} = \varepsilon_{yy} = 3.1198 \times 10^{-5}$. The surface-averaged normal strains were $\varepsilon_{xx} = \varepsilon_{zz} = \varepsilon_{yy} = 3.1185 \times 10^{-5}$. Both the volume-averaged and surface-averaged normal stresses were $\sigma_{xx} = \sigma_{yy} = \sigma_{zz} = 1\ MPa$. The surface-average incompressibility (from Equation (38)) was K_{Surf} =10.689 GPa (an error of −0.1%); the volume-average incompressibility (from Equation (40)) was K_{Vol} = 10.685 GPa (an error of −0.1%).

The error between the numerical solution and the theoretical value may be a numerical error introduced by finite difference with insufficient spatial sampling. However, in this situation, an upsampling of grids did not further reduce the error. The model was interpolated to 200 × 200 × 200 cells with a smaller spatial step of 0.5 m. In this case, each cubical grain was represented by 64 cells, instead of by 1 cell. The volume-averaged normal strains were $\varepsilon_{xx} = \varepsilon_{zz} = \varepsilon_{yy} = 3.1182 \times 10^{-5}$. The surface-averaged normal strains were $\varepsilon_{xx} = \varepsilon_{zz} = \varepsilon_{yy} = 3.1179 \times 10^{-5}$. Both the volume-averaged and surface-averaged normal stresses were $\sigma_{xx} = \sigma_{yy} = \sigma_{zz} = 1\ MPa$. According to Equation (42), the surface-average incompressibility was K_{Surf} = 10.691 GPa (an error of −0.1%), The volume-average incompressibility was K_{Vol} = 10.690 GPa (an error of −0.1%). In this instance (with the numerical grid aligned with the model), the increased resolution made little difference in terms of accuracy.

Then, with the same model geometry (200 × 200 × 200 cells), the cells were assigned, for the H–S "μ -test", the elastic parameters of K_1 = 8.564 GPa, μ_1 = 3.236 GPa, μ_2 = 3.886 GPa,

K_2 = 4.012 GPa (from Equation(62)), f_1 = f_2 = 0.5. For this model, the theoretical H–S value from Equation (63) was μ_{HS} = 3.546 GPa.

In terms of velocities and density, they were:

Material 1: $V_P = 2576.6$ *m/s*, $V_S = 1291.6$ *m/s*, $\rho = 1940$ *kg/m*^{3};

Material 2: $V_P = 2177$ *m/s*, $V_S = 1415.4$ *m/s*, $\rho = 1940$ *kg/m*^{3}.

The model size was 200 × 200 × 200 cells, with $\Delta x = \Delta y = \Delta z = 0.5\ m$. The time step was $\Delta t = 0.0375\ ms$. The primary damping parameter I used for this model was $D = 0.003$.

The modeling of the effective shear modulus was conducted by prescribing all the boundaries with shear stresses $\sigma_{xy} = \sigma_{yz} = \sigma_{xz} = 1\ MPa$. The displacement fields, the strain fields and the stress fields from the damped finite difference modeling are displayed below in Figure 33.

In this case, the volume-averaged normal strains were $\varepsilon_{xy} = \varepsilon_{xz} = 2.7077 \times 10^{-4}$, $\varepsilon_{yz} = 2.7076 \times 10^{-4}$. The surface-averaged normal strains were $\varepsilon_{xy} = \varepsilon_{yz} = 2.7215 \times 10^{-4}$, $\varepsilon_{xz} = 2.7216 \times 10^{-4}$. The volume-averaged shear stresses were $\sigma_{xy} = \sigma_{yz} = 9.6007 \times 10^5\ Pa, \sigma_{zz} = 9.6004 \times 10^5\ Pa$. The surface-averaged shear stresses were $\sigma_{xy} = \sigma_{yz} = \sigma_{xz} = 9.645\ \times 10^5\ Pa$ .The surface-average shear modulus (from Equation (39)) was μ_{surf}= 3.544 GPa (precise to three significant figures). The volume-average shear modulus (from Equation (41)) was μ_{vol} = 3.546 GPa (precise to four significant figures).

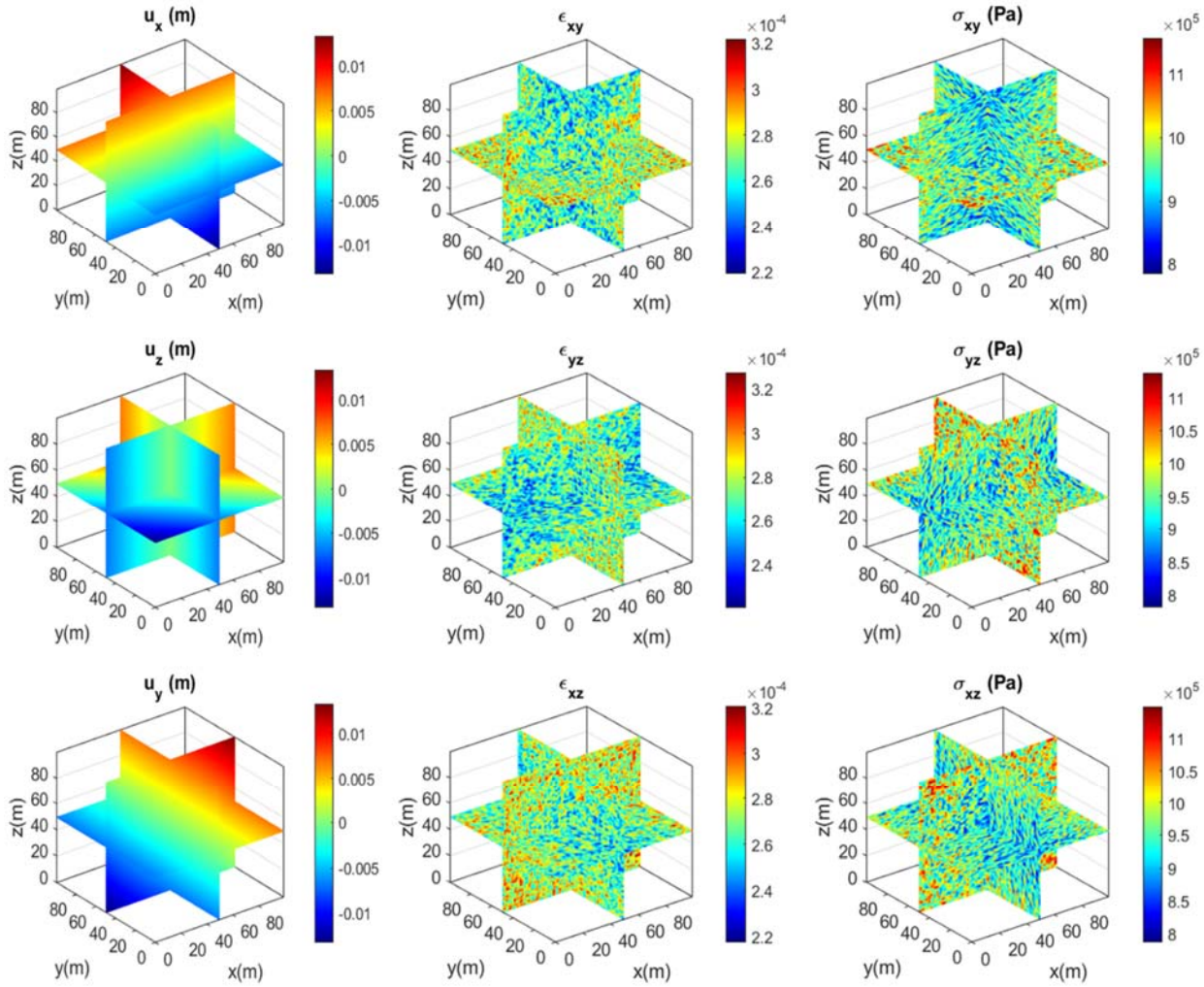

Figure 33. Displacement, strain and stress fields from the modeling of shear modulus for the nonporous model displayed in Figure 31.

4.4.3 Validation on porous rocks

Love (Love, 2013) proved that, for any shape of a homogeneous isotropic solid, its elastic response to a uniform increase of pore pressure (on all of its surfaces, internal and external) is independent of that shape, with each linear dimension decreasing proportionally, so that its shape is preserved. Hence the bulk modulus of the solid shape is the intrinsic bulk modulus of that solid. The proof is valid for any homogeneous isotropic shape if the pore space is fully connected hydraulically so that the fluid pressure is uniform.

This theorem may be applied to a representative volume element of a porous rock in a (hydraulically open) "unjacketed compression" experiment, wherein the increase in external pressure on a rock is balanced by an equal increase in internal pore pressure. If the porosity is fully connected on the time scale of the compression, the pore pressure will be uniform throughout, regardless of the complexity of the geometry. In such a test, the solid is compressed on all sides with the same additional pressure, and Love's theorem applies.

A straightforward extension of Love's proof to the case of a heterogeneous isotropic solid then concludes that, in an unjacketed test on such a rock with fully connected porosity, the solid modulus is approximately the intrinsic average modulus of the grains, as calculated above.
To numerically test the procedures above, the damped finite difference method was applied to the model of Figure 34. The previous model (Figure 31) was penetrated by straight interconnected channels of water ($K_{water} = 2.25\ GPa$, $V_P = 1500\ m/s$, $V_S = 0\ m/s$, $\rho = 1000\ kg/m^3$) as depicted; the porosity was about 35%. The figure shows the inhomogeneous case, with the solid matrix

composed 50/50 of the two minerals specified in the "*K*-test" above. Again, this model is not realistic, however, with this geometry, any inaccuracies in the calculation can be attributed to other features of the algorithm. Since a shell of water surrounded this model completely, and the pressure was applied to the exterior of this fluid shell, the solid grains were exposed on all sides to the same pressure.

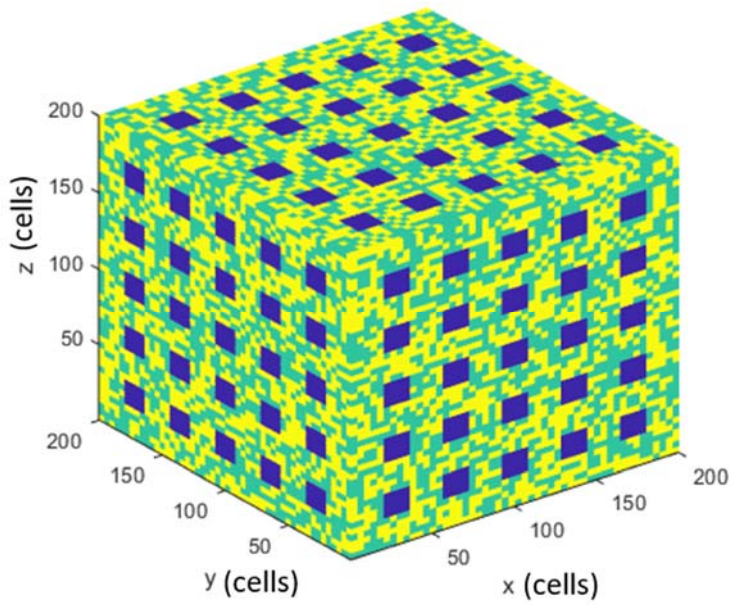

Figure 34. The heterogeneous model penetrated with straight channels of water. Without the channels, it is the same as the model in Figure 31. The channels were all aligned with the numerical grid (200 × 200 × 200 cells).

For a model like that of Figure 34, I tested Love's theorem by immersing the model in water. In numerical modeling, that means I wrapped the model with a layer of water. The water layer I wrapped was of 10 grids on each surface. The water channels that penetrated the model were all connected with each other and were all connected with the water wrapper. When applied

the normal stresses on the water wrapper, according to the definition of bulk modulus (Equation (42)), one-third of the ratio of the normal stresses and the normal strains of the solid part should be equal to the solid's effective bulk modulus.

I first tested the solid part with homogeneous solid, the model was like that of Figure 34, but the properties of material 1 were identical to those of material 2, with solid incompressibility $K_2 = K_1 = 13.564$ GPa. Normal stresses $\sigma_{xx} = \sigma_{yy} = \sigma_{zz} = 1\ MPa$ were applied on the model boundaries. The displacement fields, strain fields and the stress fields from the damped finite difference modeling are displayed below in Figure 32.

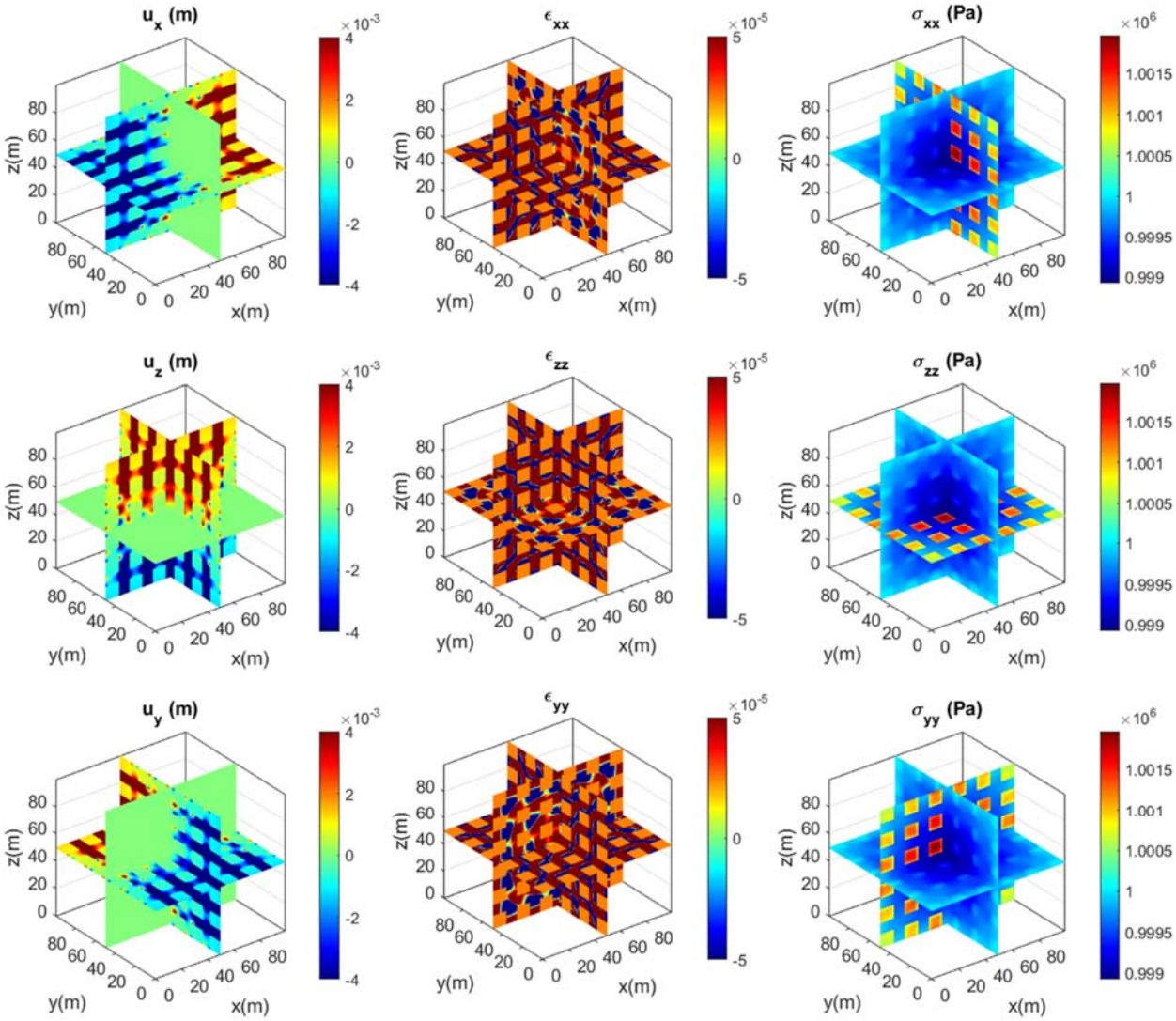

Figure 35. The displacement fields, strain fields, and stress fields from the modeling of bulk modulus for the water channel model in Figure 31, but with homogeneous solid.

For the solid part, the volume-averaged normal strains were $\varepsilon_{xx} = \varepsilon_{zz} = \varepsilon_{yy} = 2.4575 \times 10^{-5}$. The surface-averaged normal strains were $\varepsilon_{xx} = \varepsilon_{zz} = \varepsilon_{yy} = 2.4613 \times 10^{-5}$. Both the volume-averaged and surface-averaged normal stresses were $\sigma_{xx} = \sigma_{yy} = \sigma_{zz} = 1$ MPa. According to Equation (42), the surface-average incompressibility (simulating an unjacketed experiment) was $K_{Surf=13.543}$ GPa (an error of −0.2%). The calculated solid-volume-average incompressibility was $K_{Vol} = 13.564$ GPa (precise to five significant figures).

For the inhomogeneous model of Figure 34, with the inhomogeneous solid, the same procedures were repeated. The displacement fields, strain fields, and stress fields from the damped finite difference modeling are displayed below in Figure 36.

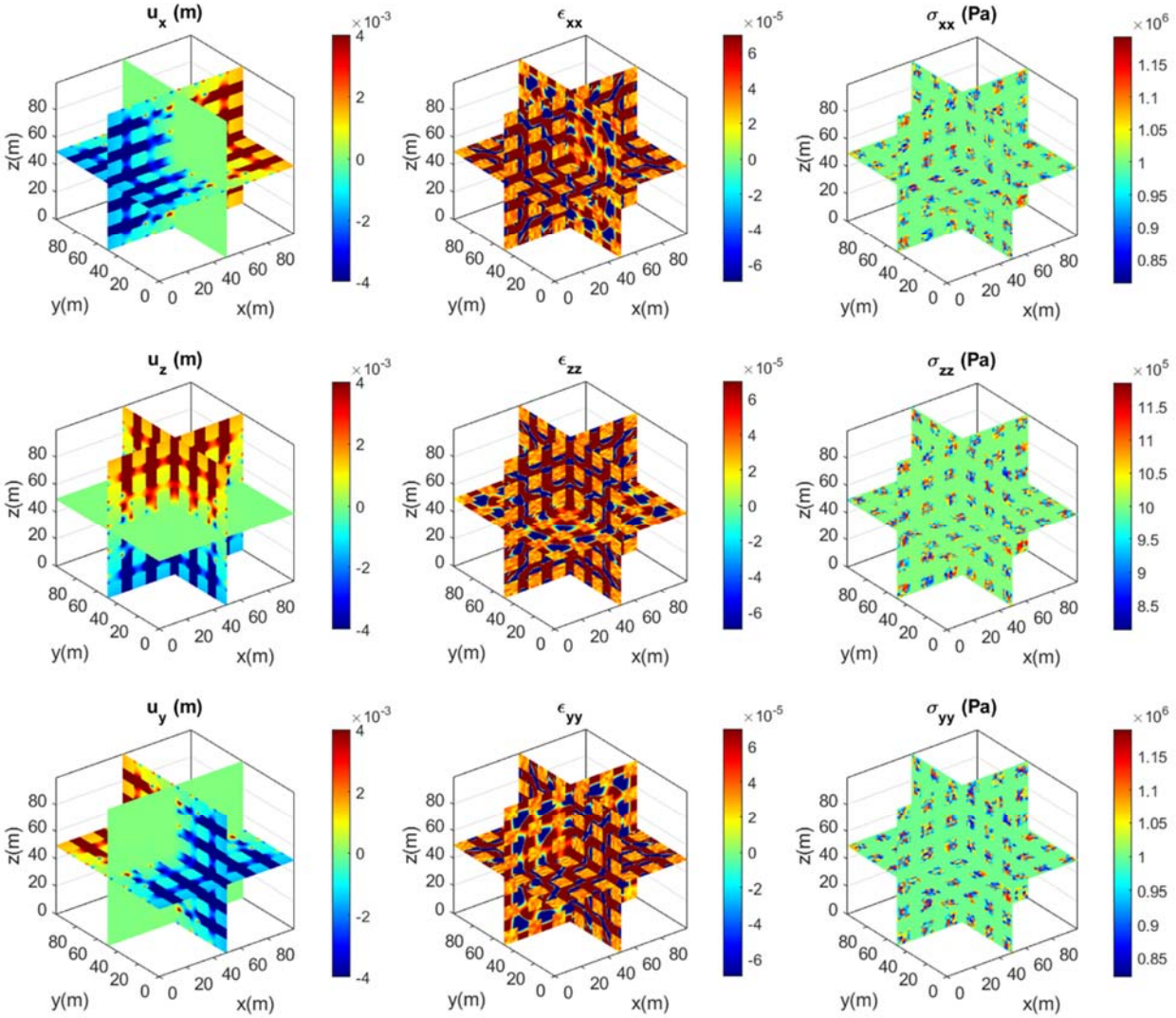

Figure 36. The displacement fields, strain fields, and stress fields from the modeling of bulk modulus for the water channel model in Figure 31, with inhomogeneous solid.

For the solid part, the volume-averaged normal strains were $\varepsilon_{xx} = \varepsilon_{zz} = \varepsilon_{yy} = 3.1299 \times 10^{-5}$. The surface-averaged normal strains were $\varepsilon_{xx} = \varepsilon_{zz} = \varepsilon_{yy} = 3.1322 \times 10^{-5}$. Both the volume-averaged and surface-averaged normal stresses were $\sigma_{xx} = \sigma_{yy} = \sigma_{zz} = 1$ MPa. According to Equation (42), the surface-average incompressibility (simulating an unjacketed experiment) of the solid portion only was K_{Surf} = 10.642 GPa, (an error of −0.5%). The volume-average incompressibility of the solid portion only was K_{Vol} = 10.650 GPa, (an error of −0.5%). These differences are a measure of the accuracy of the extension of Love's theorem to the case of inhomogeneous solid, as well as the accuracy of the damped finite difference algorithm.

There is no equivalent process for determining the average shear modulus μ_s of the grains of the porous rock. If the H–S "μ -test" were applied to a composite with one constituent fluid (μ_1= 0), the required K_2 from Equation (62) would be negative (hence un-physical), so the H–S "μ -test" is not applicable.

CHAPTER 5 COMPARISON WITH FINITE ELEMENT METHOD

In Chapter 4, I used various analytical models to verify the accuracy and validity of the damped finite difference method. In this Chapter, I will compare the damped finite difference method with the finite element method which has been widely used in static stress and strain modeling. I used an open source finite element code and focused on the comparison of accuracy and computational performance. From both the 2D and 3D examples, I found that the finite element code consumes more memory than the finite difference method, while their computation time is similar. Furthermore, in the demonstrated 3D example, I found that to achieve the same accuracy, the finite element method needs a finer grid than the finite difference method.

5.1 Comparison of results for a 2D model

I used an open-source finite element code which has been widely used in digital rock studies (Garboczi, 1998) to compare accuracy and computational efficiency with the damped finite difference method. The finite element code solves for static stress and strain fields using an iterative algorithm with conjugate gradient relaxation.

I tested a 2D $100\ cm$ by $100\ cm$ model of shale with a $20\ cm$ by $20\ cm$ cubic inclusion of dolomite in the middle of the model (Figure 37). The elastic properties of dolomite and shale are:

Dolomite: $V_P = 5200$ *m/s*, $V_S = 2700$ *m/s*, $\rho = 2450$ *kg/m*^{3};

Shale: $V_P = 2900$ *m/s*, $V_S = 1400$ *m/s*, $\rho = 2340$ *kg/m*^{3}.

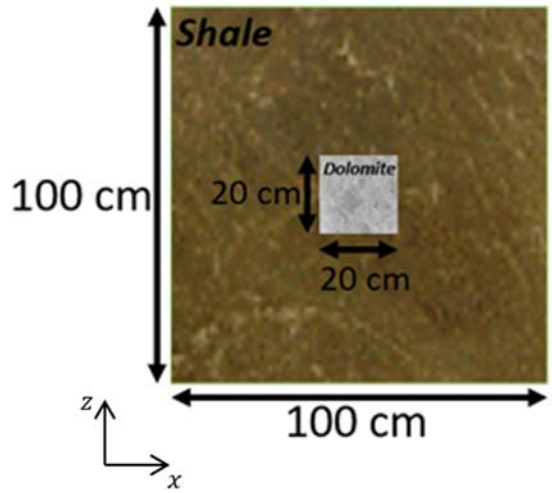

Figure 37. Illustration of the 2D model of shale with the inclusion of dolomite.

The strain and stress fields were calculated using finite difference and finite element methods with the boundary conditions of $\sigma_{xx} = \sigma_{zz} = \sigma_{xz} = 1\ MPa$. Both methods generated similar results (Figure 38, Figure 39, and Figure 40) with the max relative difference less than 1% (especially around the inclusion boundaries) which might be attributed to the different numerical schemes.

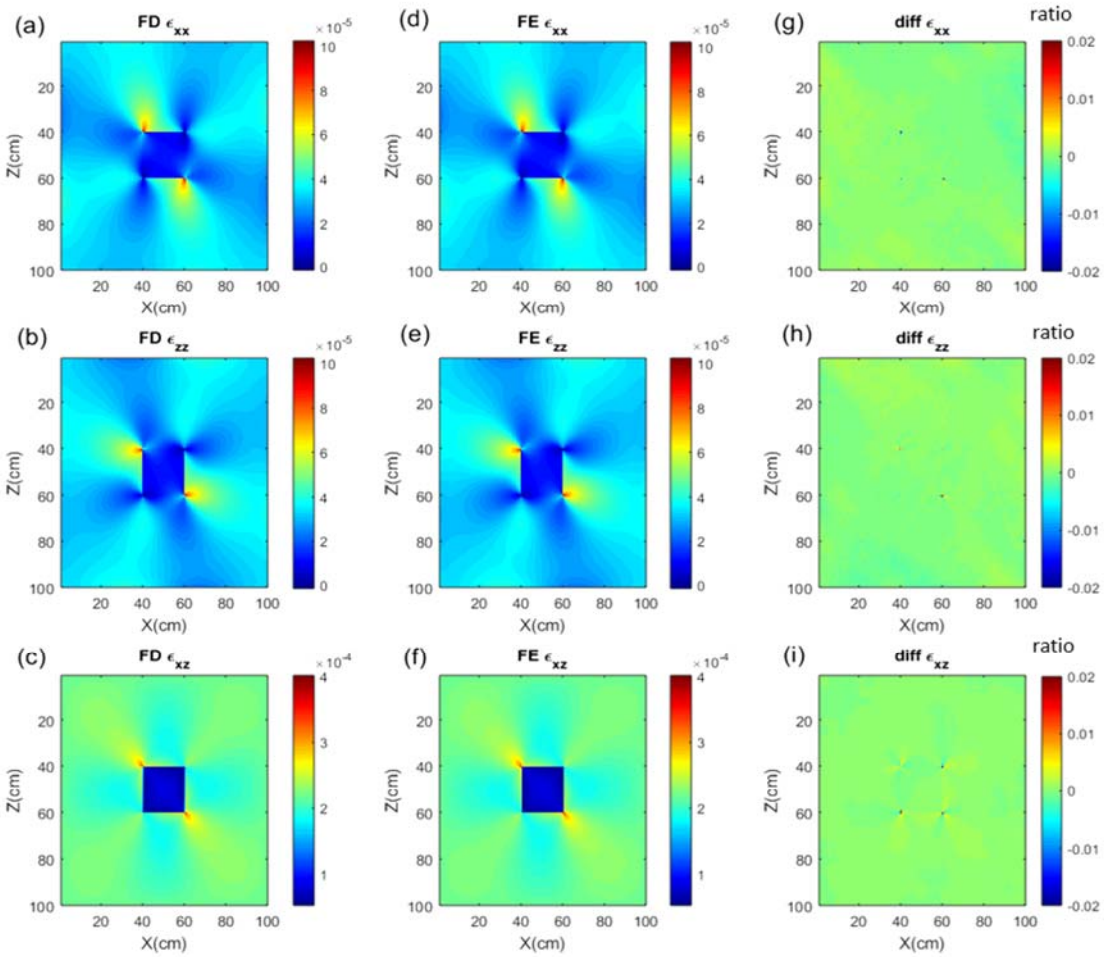

Figure 38. Comparison of the strain fields modeled from the damped finite difference method and the finite element method. Under the same stress boundary conditions, the strain fields calculated by the finite difference method (a, b and c) are similar to the ones calculated by the finite element method (d, e and f). The max relative difference is less than 1% which mainly focuses around the inclusion boundaries (g, h and i).

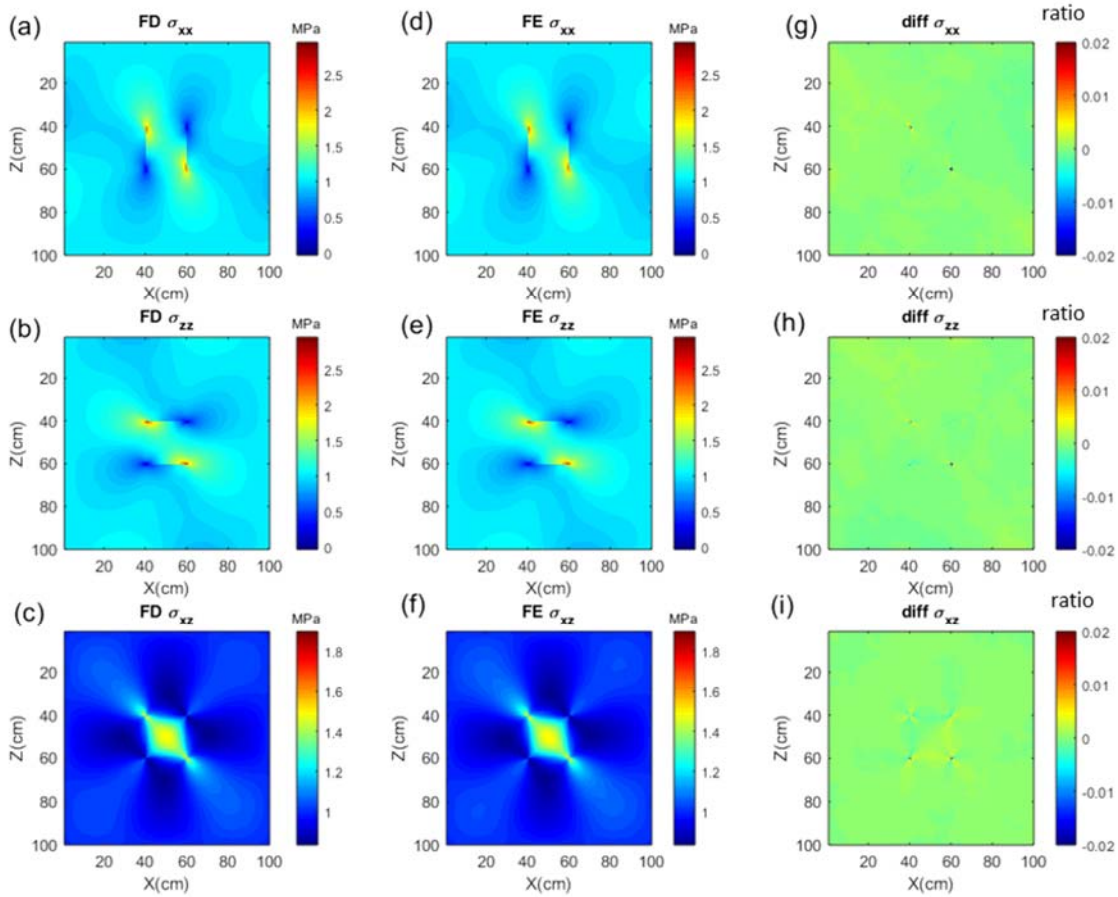

Figure 39. Comparison of the stress field modeled from the damped finite difference method and the finite element method. Under the same stress boundary conditions, the stress fields calculated by the finite difference method (a, b and c) are similar to the ones calculated by the finite element method (d, e and f). The max relative difference is less than 1% which mainly focuses around the inclusion boundaries (g, h and i).

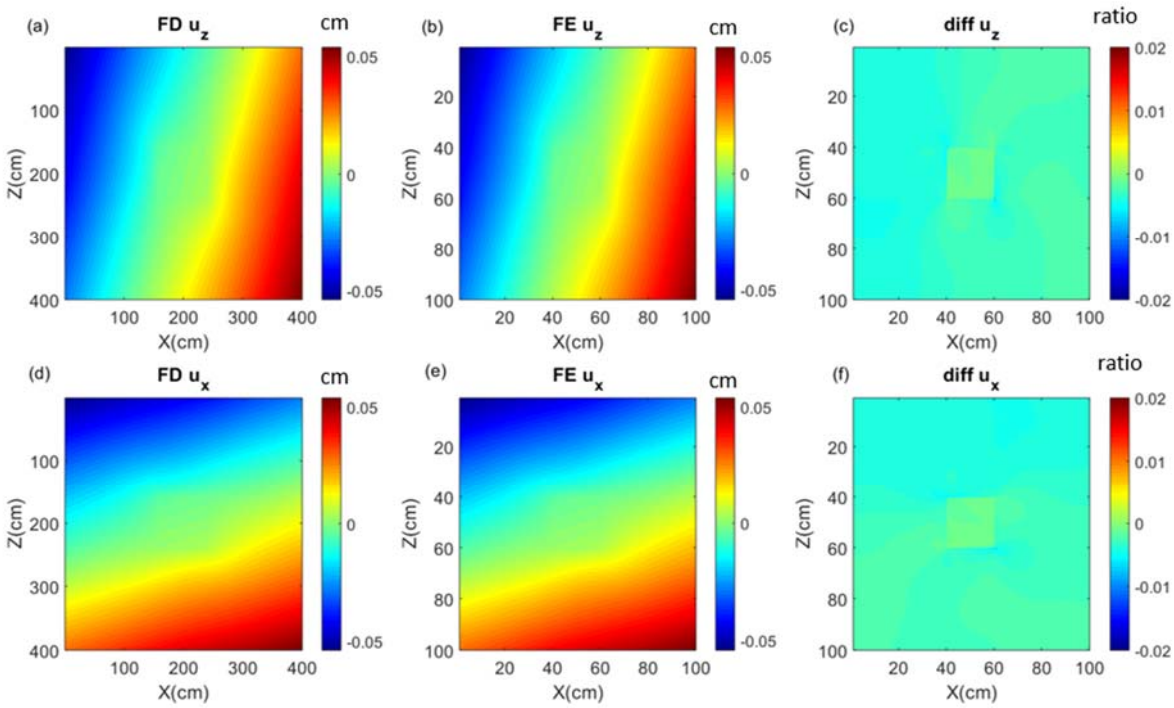

Figure 40. Comparison of the displacement field modeled from the damped finite difference and the finite element method. Under the same stress boundary conditions, the displacement fields calculated by the finite difference method (a and d) are similar to the ones calculated by the finite element method (b and e). The maximum relative difference is less than 1% (c and f).

Following the numerical comparison, I compared the performance of the two methods running on the same workstation. To benchmark two methods, I used a 400 cells by 400 cells model with the spatial step $\Delta x = \Delta z = 0.25\ cm$. For the damped finite difference code, I used the time step $\Delta t = 3.47 \times 10^{-5}\ s$ and damping parameter $D = 0.0064$. It took 19.5 seconds CPU time and 14 MB memory. The finite element code took 20.1 seconds and 20 MB. Since the finite element code is optimized with the conjugate gradient method, the computing time advantage of the damped finite difference method was not obvious on such a small model. However, the memory usage was 30% less for the damped finite difference method than the finite element method. Generally, the finite element methods use more memory than the finite difference methods for their needs for storing neighbor information specially needed for boundaries (Garboczi, 1998). Additionally, there is much room to optimize the finite difference method significantly in particular for computing large 3D models in a parallel computing architect.

5.2 Comparison of results for a 3D model

As Garboczi (1998) pointed out, if the resolution were infinite, then the results obtained from the finite difference and the finite element methods would be the same. However, in real situations, the resolution is not infinite, and the sampling rate, or grid size, is always an important factor to consider in numerical modeling for the limited computational resources and time.

Moczo et al., (2010) did a study on the accuracy of the finite difference and the finite element methods on seismic wave propagation modeling. They found that the errors from the finite element methods on both amplitude and angle depend heavily on the sampling rate, while

the finite difference method is not that sensitive to the sampling rate. In other words, to achieve the same accuracy, the finite element method needs a finer grid than the finite difference method.

In the following, I used the Hashin-Shtrikman "K-test" described in Section 4.4 to investigate the accuracy of both methods under different grid configurations.

The model shown in Figure 31 was used for the test with two different grid configurations: the first one with the spatial grid step of $\Delta x = \Delta y = \Delta z = 2\ m$, and the second one with the spatial grid step of $\Delta x = \Delta y = \Delta z = 0.5\ m$. The computed stress, strain, and displacement fields of the damped finite difference and the finite element method under the first grid configuration were computed, and the results are displayed in Figure 41 to Figure 43.

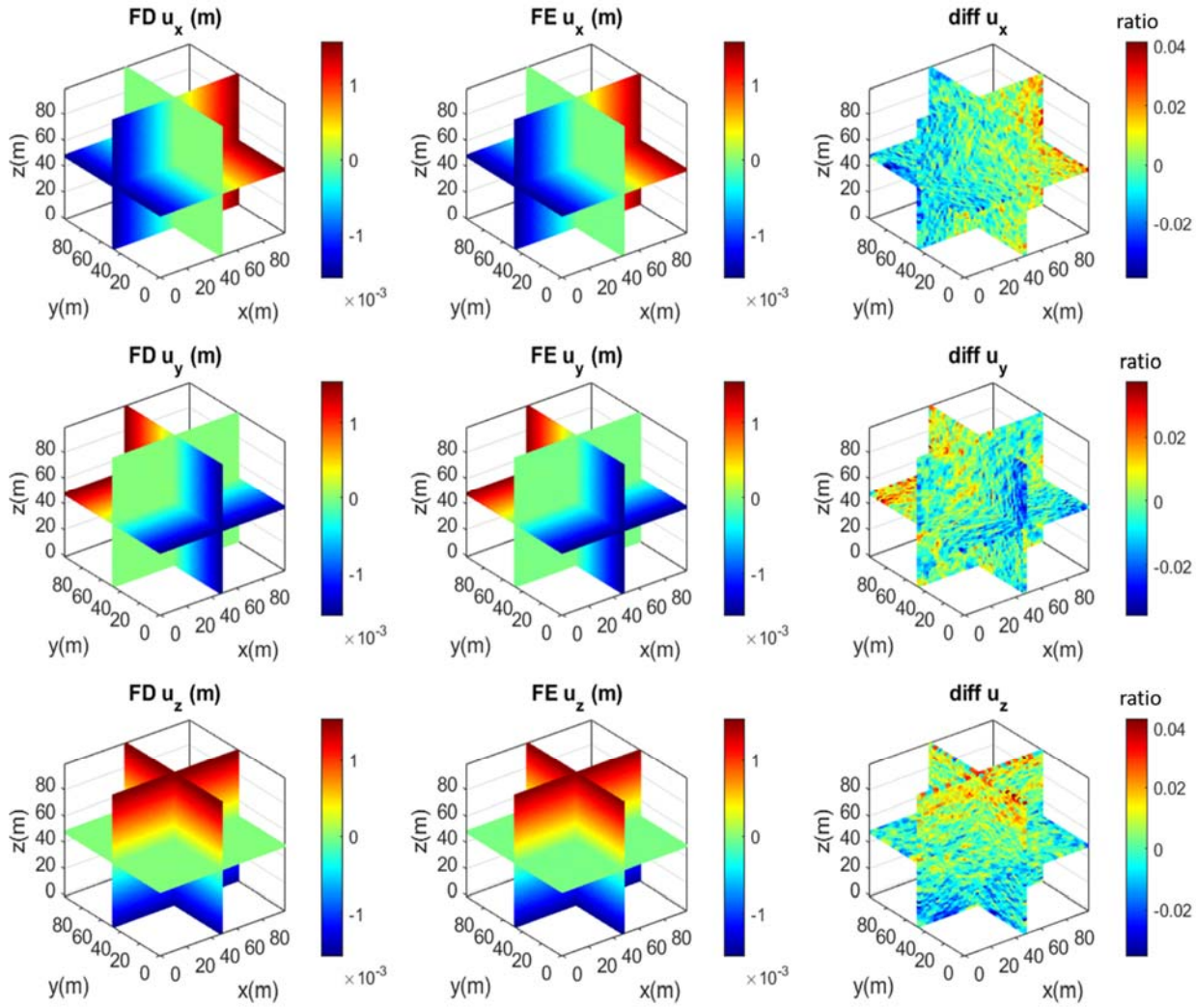

Figure 41. The displacement fields calculated from the damped finite difference (the left column) and the finite element methods (the middle column), for the model shown in Figure 31 with the first grid configuration of grid sampling step of 2 m in all dimensions. The relative difference is shown in the right column. The maximum difference is around 4%.

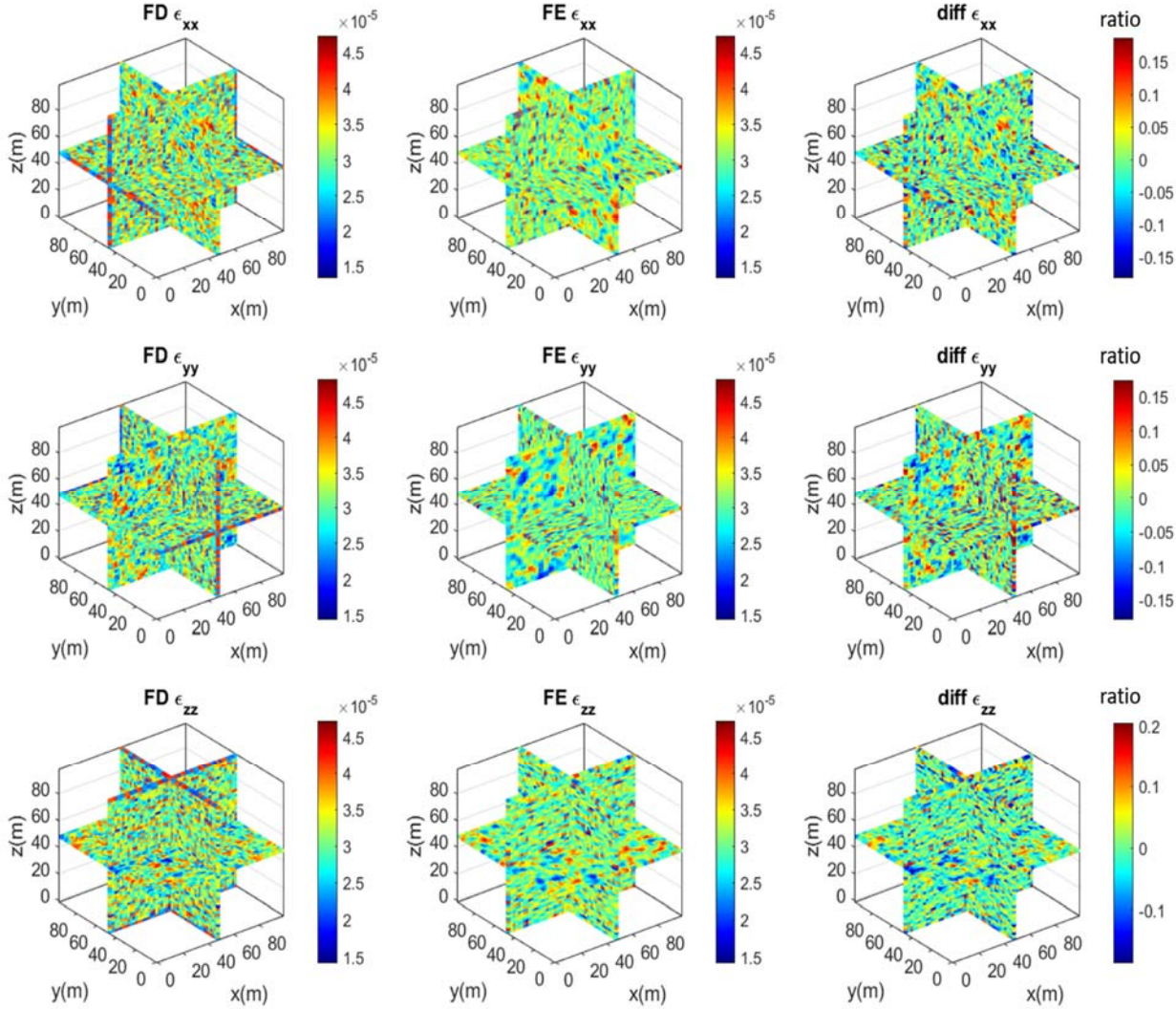

Figure 42. The strain fields calculated from the damped finite difference (the left column) and the finite element methods (the middle column), for the model shown in Figure 31 with the first grid configuration of grid sampling step of 2 m in all dimensions. The relative difference is shown in the right column.

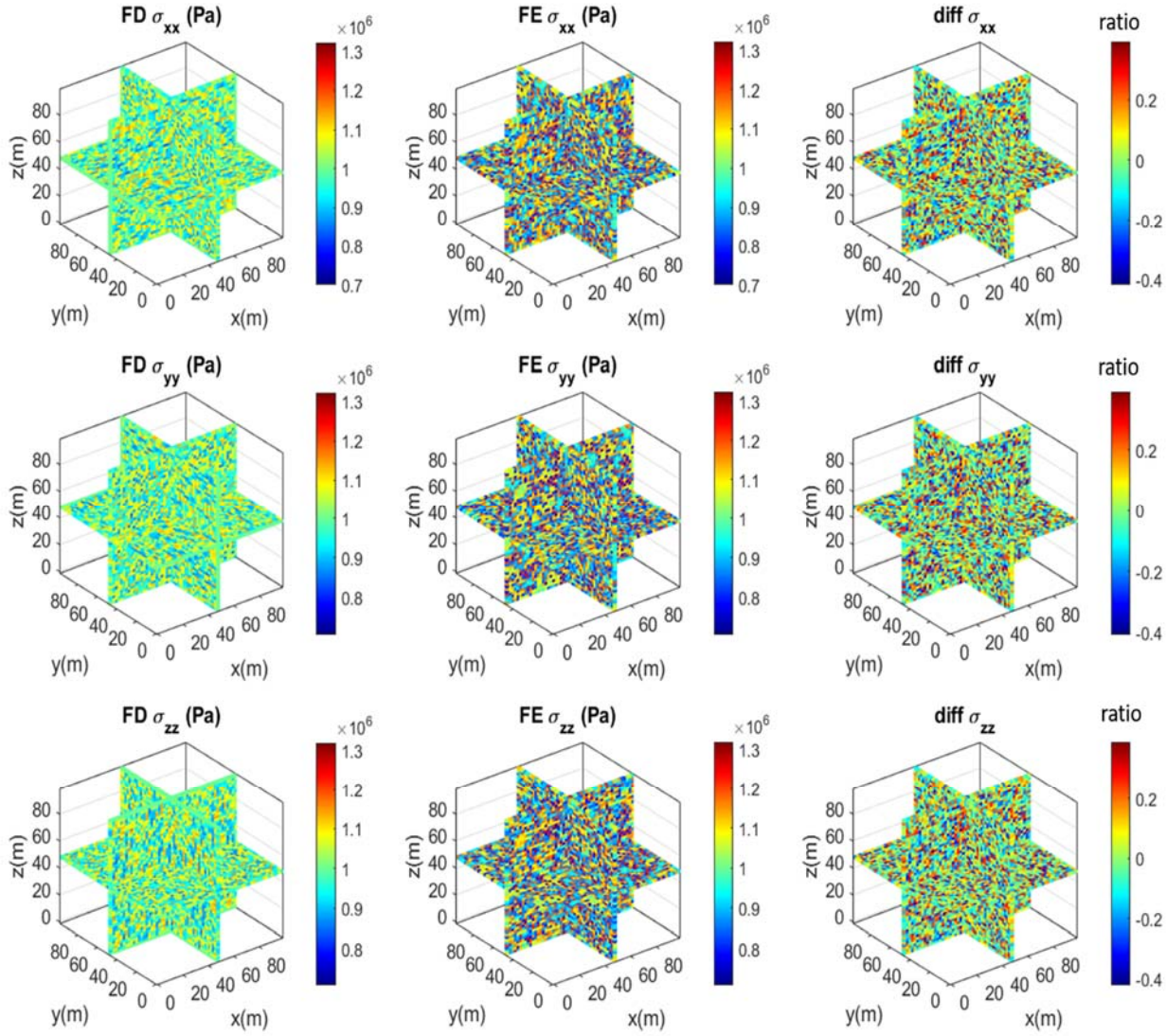

Figure 43. The stress fields calculated from the damped finite difference (the left column) and the finite element methods (the middle column), for the model shown in Figure 31 with the first grid configuration of grid sampling step of 2 m in all dimensions. The relative difference is shown in the right column.

With the spatial grid step of 2 m in each dimension, the relative differences among the displacement fields (Figure 41) from both methods were much smaller compared to those of the stress (Figure 42) and the strain (Figure 43) fields. In other words, both methods generated similar results at the large scale (since the displacement field is the spatial integration of the corresponding strain field), while due to the different handling of the material boundaries, they generate quite different results at the small scale.

To compare the accuracy of the two methods, the analytically calculated H-S value $K_{HS} = 10.700\ GPa$ from Equation (59) was calculated numerically again using results from both methods respectively. The closer to the analytical solution $K_{HS} = 10.700\ GPa$, the more accurate the numerical method is. It turned out the damped finite difference method was more accurate than the finite element method for the first grid configuration. For the surface-average incompressibility, the damped finite difference method computed $K_{Surf} = 10.689\ GPa$ was 0.1% smaller than the theoretical K_{HS} while the finite element method comptuted $K_{Surf} = 10.822\ GPa$ was 1.1% larger than the theoretical K_{HS}. Similarly, for the volume-average incompressibility, the damped finite difference method computed $K_{Vol} = 10.685\ GPa$ was 0.1% smaller than the theoretical K_{HS} while the finite element method computed $K_{Vol} = 10.828\ GPa$ was 1.2% larger than the theoretical K_{HS}.

Then, for the second grid configuration with spatial grid step of 0.5 m, the stress, strain, and displacement fields were computed using both methods (Figure 44 to Figure 46) and the corresponding surface-average and volume-average incompressibilities were calculated against

the theoretical K_{HS}. The results indicated a huge increment of accuracy for the finite element method while little effects on the damped finite difference method, as expected. For the surface-average incompressibility, the damped finite difference method computed $K_{Surf} = 10.691\ GPa$ was 0.1% smaller than the theoretical K_{HS} while the finite element method comptuted $K_{Surf} = 10.704\ GPa$ was 0.04% larger than the theoretical K_{HS}. Similarly, for the volume-average incompressibility, the damped finite difference method computed $K_{Vol} = 10.690\ GPa$ was 0.1% smaller than the theoretical K_{HS} while the finite element method computed $K_{Vol} = 10.705\ GPa$ was 0.05% larger than the theoretical K_{HS}.

Though the accuracy of the finite element method was a little higher than the damped finite difference method at the finer grid, to achieve such accuracy it took 64 times of the finite difference method's computation cost, in both time and memory use. My findings are consistent with the conclusion from Moczo et al., (2010) that, to achieve the same accuracy, the finite element method needs a much finer grid than the finite difference method. Overall, it shows that the damped finite difference method is a well-balanced method in terms of accuracy and performance when computing the static stress-strain solutions.

For the computational performance on this 3D model, it shows the same pattern as for the 2D model: the computation time from the finite difference and finite element method is similar, while the finite difference method consumed less memory than the finite element method. For the case of 50 cells × 50 cells × 50 cells), the finite element program took 1.2 $mins$, with the memory usage of 12 MB and the damped finite difference program took 1.3 $mins$, with the

memory usage of 9 MB. For the case of 200 cells $\times$ 200 cells $\times$ 200 cells, the finite element program took 3.94 hrs, with the memory usage of 765 MB and the damped finite difference program took 4.12 hrs, with the memory usage of 519 MB. For the damped finite difference program, I used the optimal damping parameter (based on Equation (26) and Equation (27)) of $D = 0.026$, and set the program to stop automatically when the model's overall kinetic energy reached below $10^{-5}\,J$, as in Figure 10.

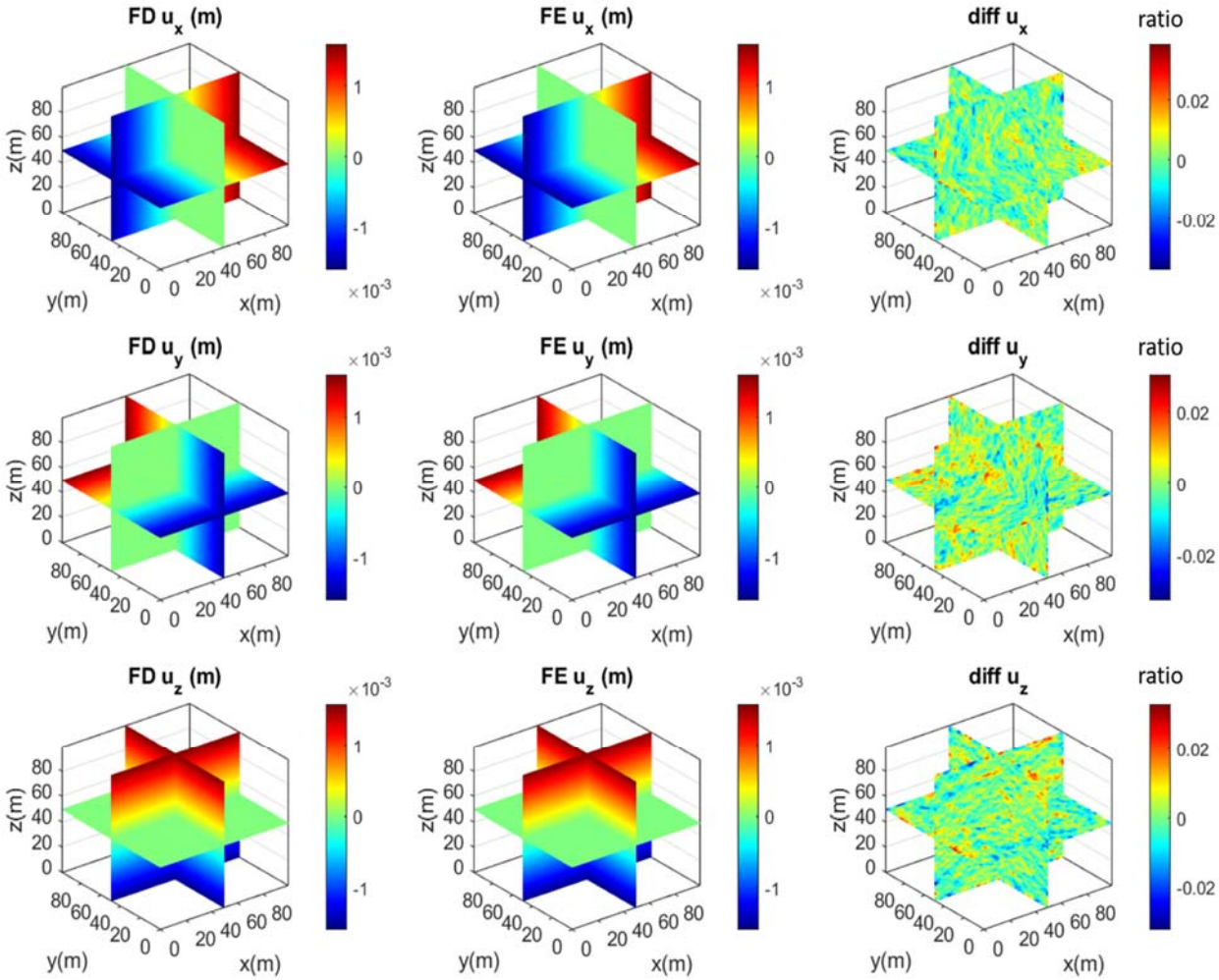

Figure 44. The displacement fields calculated from the damped finite difference (the left column) and the finite element methods (the middle column), for the model shown in Figure 31 with the second grid configuration of grid sampling step of 0.5 m in all dimensions. The relative difference is shown in the right column. The maximum difference is less than 4%.

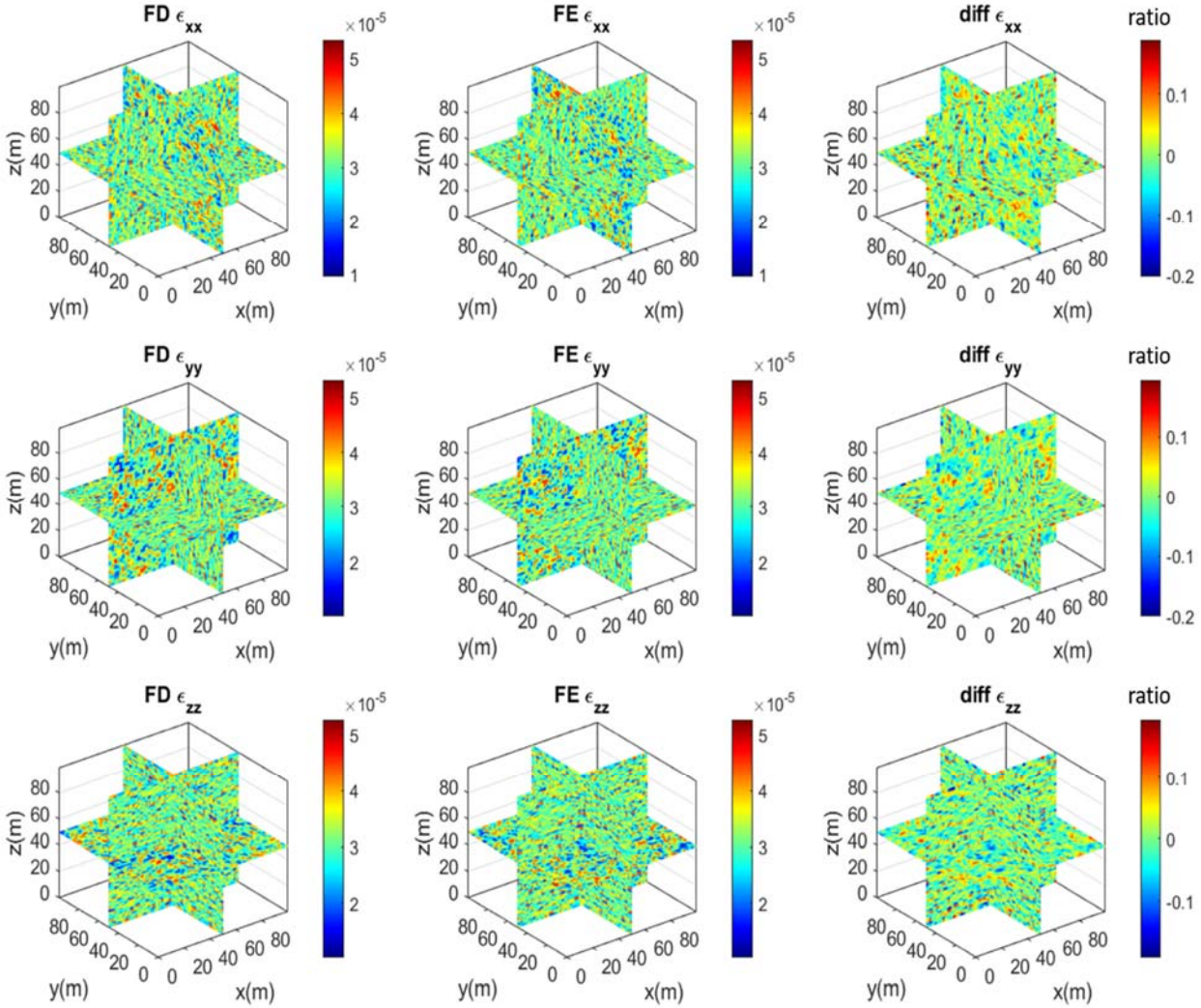

Figure 45. The strain fields calculated from the damped finite difference (the left column) and the finite element methods (the middle column), for the model shown in Figure 31 with the second grid configuration of grid sampling step of 0.5 m in all dimensions. The relative difference is shown in the right column.

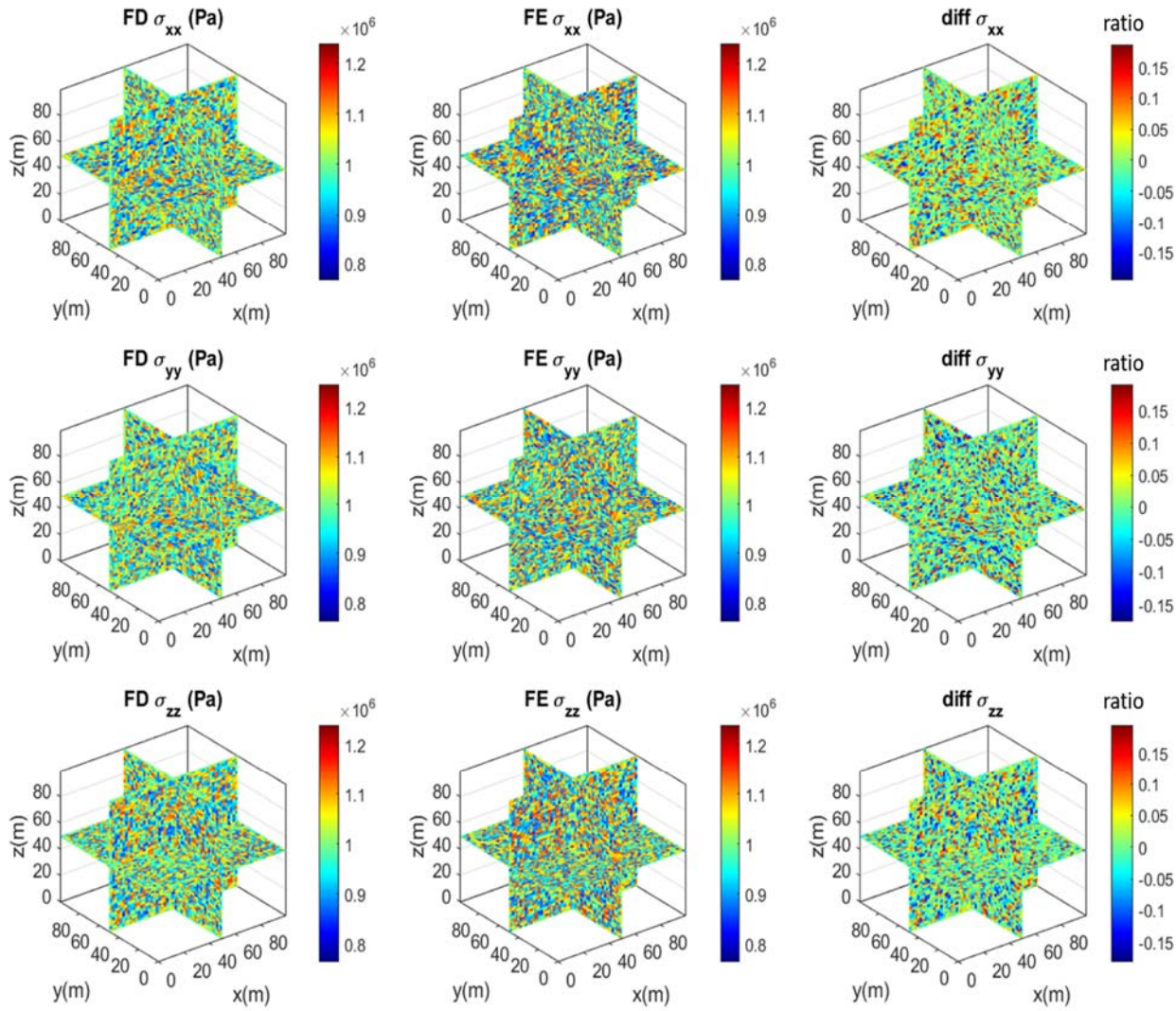

Figure 46. The stress fields calculated from the damped finite difference (the left column) and the finite element methods (the middle column), for the model shown in Figure 31 with the second grid configuration of grid sampling step of 0.5 m in all dimensions. The relative difference is shown in the right column.

CHAPTER 6 AN APPLICATION: STRONG ANISOTROPY IN SUBDUCTED SLABS AND ITS IMPLICATION IN DEEP CARBON CYCLE

In this chapter, I will show how my damped finite difference method can be used to understand a recent discovery of strong anisotropy in the subducted slabs. The cause of the strong anisotropy is not well understood yet and the reasons can be many. Here, I explored one of the potential causes for the observed strong anisotropy using an inclusion model. The results in this chapter depend on the assumption of the inclusion model. I used the damped finite difference method to show that the shear modulus of the inclusion must be less than one-tenth of the matrix shear modulus to achieve such strong anisotropy. I also constrained the volume of the inclusions and their aspect ratios. Such inclusions may be aligned fluids or carbonatite melts. I then discussed their possible link to the subducted carbon. If the inclusions are carbonatite melts, the results in this chapter can put bounds on the amount of subducted carbon at subduction zones.

6.1 Background

Deep-focus earthquakes, whose depths are greater than $300\ km$ can happen ubiquitously in subducting slabs. Li et al., (2018) studied the deep earthquakes near the subducting slab interface in Tonga (TG), Molucca (MO), and Mariana–Japan–Kuriles (MJK) and inverted for the in situ anisotropy using the earthquake moment tensors (Ekström et al., 2012) to explain the none-double-couple components of the deep earthquake radiation patterns.

From their inversion results, the anisotropy is from a tilted transversely isotropic (TTI) medium with symmetry axes either perpendicular or parallel to the slab interface. They obtained a strong shear anisotropy, with the Thomsen's shear anisotropy parameter γ (Thomsen, 1986) averaged around 0.3 for $300 - 670\ km$ depths (Figure 47).

Anisotropy can be from many origins. No consensus exists so far to explain the high anisotropy at this depth. However, Li et al., (2018) thought that the most likely cause for the highly anisotropic rock fabric that surrounds the hypocenters are aligned minerals or inclusions and their associated lithological layering. From the mineralogical point of view, olivine and pyroxene, two major minerals in the upper mantle, have strong anisotropy but their shear wave anisotropy values are not as high as the observed 0.3. For olivine, its maximum anisotropy of shear wave velocity is 0.18. For pyroxene, the orthopyroxene has a maximum shear wave anisotropy of 0.15 while the clinopyroxene has a maximum shear wave anisotropy of 0.24 (Mainprice et al., 2000). It seems the lattice preferred orientation (Karato et al., 2008) of minerals due to mantle flow cannot explain the observed strong anisotropy by Li et al. (2018).

It is widely believed that the polymorphic metastable olivine–wadsleyite phase transformation (At the 410 km depth, olivine transforms to wadsleyite under increasing pressure and temperature) is the cause for the deep-focus earthquakes (Green et al., 2010). However, in that case, the expected anisotropy for a rock containing spinel inclusions should be around 5% (Bina and Wood, 1987), not the 30% S-wave anisotropy observed.

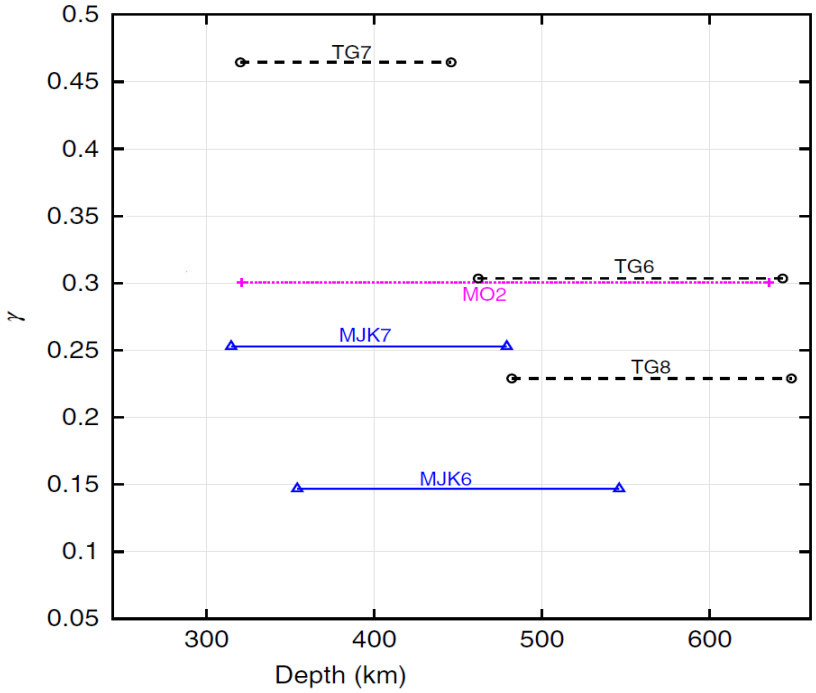

Figure 47. The shear anisotropy strength γ in the 6 studied deep earthquake regions. They are the Tonga earthquake groups 6-8 (TG6-TG8), Molucca earthquake group 2 (MO2), and Mariana–Japan–Kuriles earthquake groups 6-7 (MJK6 - MJK 7). The earthquake groups are based on their spatial proximity. All the earthquakes are located around the slab interface (distance less than 55 km). The horizontal lines represent the depth ranges of different earthquake groups. (Adapted from Li et al., 2018, Fig.3b).

Recent lab work showed that magnesite ($MgCO_3$) has a high shear anisotropy around 0.45 (Yang et al., 2014; Yao et al., 2018) and it is the major carbon host in subducting slabs (Dasgupta and Hirschmann, 2010). It can occur as veins in its host (Holyoke et al., 2014), which makes it qualified as laminated rock inclusion. Because of its weaker (orders of magnitude weaker) mechanical strength than the surrounding rocks, magnesite is considered to cause deep-focus earthquakes from ductile-brittle instabilities (Holyoke et al., 2014). All these properties make magnesite a potential rock fabric material to explain the strong anisotropy in the subducting slabs. Alternatively, as the carbonated oceanic crust approaches the solidus at the transition zone depths (Thomson et al., 2016), carbonatite melt can be present (Li et al., 2018). If the inclusion is the aligned carbonate solids or melts, studying deep earthquakes provides a means to constrain the amount of carbonate subducted.

In my work, I take the "inclusion model" as a working hypothesis and explore what type of inclusions can give rise to the high anisotropy. I found that carbonate melt is a possible candidate. The result has huge implications for the carbon cycle in the Earth. Carbon is cycled at a planetary scale from the atmosphere to the deep mantle and directly impacts the climate and habitability of the Earth (Gerbode and Dasgupta, 2010; Hayes and Waldbauer, 2006). Since the onset of plate tectonics, carbon has been transported from the surface to the interior of the Earth primarily through subduction zones(Shirey and Richardson, 2011; Stern et al., 2016; Xu et al., 2018). While many studies have focused on the chemical reactions and mass flux of the carbon cycle (e.g., Dasgupta and Hirschmann, 2010; Kelemen and Manning, 2015; Thomson et al., 2016), how much carbon is expelled from the oceanic crust to the ambient mantle remains an

open question. Here I adopted rock physics modeling to explore the implications of the inclusion model and to tentatively quantify the amount of carbon. I constructed the slab as an effective VTI medium with penny-shaped inclusions, which mimic the laminated rock fabric. From the modeling results, I investigated the rock material and phases that could result in the shear anisotropy around 0.3.

6.2 Method

I used horizontally aligned penny-shaped inclusions to simulate the laminated rock fabric (Figure 48). Although the lithological layering is also a possible rock physics model to simulate a VTI medium, I focus on the inclusions model to particularly explore the fluid-phase possibilities. The model is of size 200 cells $\times$ 200 cells $\times$ 200 cells, with grid spacing $\Delta x = \Delta y = \Delta z = 0.5\ m$. By controlling the inclusion material, inclusion volume fraction and the aspect ratio of the penny-shaped inclusion, one can build numerical rock models with varying degrees of anisotropy, measured volumetrically by the damped finite difference modeling method.

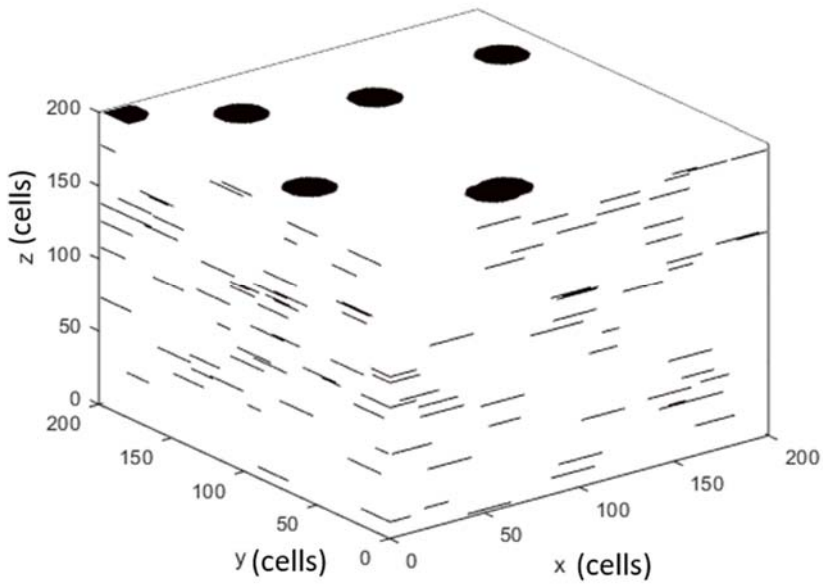

Figure 48. Rock model with thin penny-shaped inclusions embedded. The Black indicates inclusions and the white indicates the solid matrix.

The penny-shaped inclusion model is commonly referred as penny-shaped crack model in the rock physics literature. In this dissertation, we use "inclusion" instead of "crack" to avoid confusion of open cracks in the 500 km high-pressure depth. But we keep the terminology "crack density" to be consistent with the literature. Several theoretical expressions have been proposed for the elastic properties of aligned saturated cracks, including the Hudson model (Hudson, 1980), Eshelby-Cheng model (Cheng, 1993; Eshelby, 1957), and Thomsen's model (Thomsen, 1995). For example, Thomsen (1995) introduced the expressions of anisotropy for aligned circular cracks in a porous background. If the cracks are in zero equant porosity background, the anisotropy parameter gamma is:

$$\gamma = \left(\frac{8}{3}\right)\left(\frac{1 - v_s}{2 - v_s}\right)\eta_c, \tag{64}$$

where η_c is the *crack density* and v_s is Poisson's ratio of the matrix solid. The definition for the *crack density* is:

$$\eta_c = \frac{3\phi}{4\pi\alpha}, \tag{65}$$

where $\emptyset$ is the inclusion volume fraction, and α is the inclusion aspect ratio, which equals to the short axis length divided by the long axis length.

Though they all agreed that the *crack density* plays an important role in the overall anisotropy of the model, the mentioned theoretical expressions all have limitations of assuming low *crack density* (usually <0.1) and are unable to describe the geometric distribution of the cracks. Therefore, I used numerical modeling instead, attempting to generate more accurate results.

Since the *crack density* is a function of inclusion volume fraction and inclusion aspect ratio (Equation (65)), I therefore ran modelings with both inclusion volume fraction and inclusion aspect ratio as varying parameters to generate a series of results.

The numerical modeling outputs stress and strain fields for each model, which can then be used to calculate the effective elastic constants of the model based on Hooke's law (Equation (66)) to obtain the effective γ value from shear elastic constants (Equation (67)). Since I only focus on the shear anisotropy, I apply the boundary conditions of shear stresses only, with $\sigma_{xy} = \sigma_{yz} = \sigma_{xz} = 1\ MPa$.

$$\begin{bmatrix}\sigma_{xx}\\ \sigma_{yy}\\ \sigma_{zz}\\ \sigma_{yz}\\ \sigma_{xz}\\ \sigma_{xy}\end{bmatrix}=\begin{bmatrix}C_{11} & C_{12} & C_{13} & 0 & 0 & 0\\ C_{12} & C_{22} & C_{23} & 0 & 0 & 0\\ C_{13} & C_{23} & C_{33} & 0 & 0 & 0\\ 0 & 0 & 0 & C_{44} & 0 & 0\\ 0 & 0 & 0 & 0 & C_{44} & 0\\ 0 & 0 & 0 & 0 & 0 & C_{66}\end{bmatrix}\begin{bmatrix}\varepsilon_{xx}\\ \varepsilon_{yy}\\ \varepsilon_{zz}\\ \varepsilon_{yz}\\ \varepsilon_{xz}\\ \varepsilon_{xy}\end{bmatrix}, \tag{66}$$

$$\gamma = \frac{C_{66}-C_{44}}{2C_{44}}. \tag{67}$$

First, I assigned magnesite as the inclusion material for the shear anisotropy modeling. Yao et al., (2018) studied the properties of magnesite under different temperature and pressure conditions. They provided relationships of velocity, density, and elastic anisotropy of magnesite with depth along a normal mantle geotherm compared to the Preliminary Reference Earth Model (PREM) (Dziewonski and Anderson, 1981) (Figure 49). Since the average depth of the deep-focus earthquakes under my study is around $500\ km$, I assigned isotropic P-wave velocity $V_P = 9200\ m/s$, orthogonally polarized S-wave velocity $V_{S1} = 4900\ m/s$, $\rho = 3250\ kg/m^3$ and $A_s^{po} = 0.45$ to the magnesite, according to Yao et al., (2018). A_s^{po} is the polarization anisotropy factor for shear wave, which is defined as:

$$A_s^{po} = (V_{S1} - V_{S2})/V_S, \tag{68}$$

where V_{S1} and V_{S2} are two orthogonally polarized shear wave velocities, V_S is the aggregate shear velocity, which was approximated as the average of V_{S1} and V_{S2}.

Because magnesite is anisotropic, I can not use the elastodynamic equation for isotropic materials (Equation (22)) for numerical modeling. Instead, I used the following equations

$$
\begin{cases}
\frac{\partial v_x}{\partial t} + d v_x = b\left(\frac{\partial \sigma_{xx}}{\partial x} + \frac{\partial \sigma_{xz}}{\partial z} + \frac{\partial \sigma_{xy}}{\partial y}\right) \\
\frac{\partial v_z}{\partial t} + d v_z = b\left(\frac{\partial \sigma_{xz}}{\partial x} + \frac{\partial \sigma_{zz}}{\partial z} + \frac{\partial \sigma_{yz}}{\partial y}\right) \\
\frac{\partial v_y}{\partial t} + d v_y = b\left(\frac{\partial \sigma_{xy}}{\partial x} + \frac{\partial \sigma_{yz}}{\partial z} + \frac{\partial \sigma_{yy}}{\partial y}\right) \\
\frac{\partial \sigma_{xx}}{\partial t} = C_{11}\frac{\partial v_x}{\partial x} + C_{12}\frac{\partial v_y}{\partial y} + C_{13}\frac{\partial v_z}{\partial z} \\
\frac{\partial \sigma_{yy}}{\partial t} = C_{12}\frac{\partial v_x}{\partial x} + C_{22}\frac{\partial v_y}{\partial y} + C_{23}\frac{\partial v_z}{\partial z} \\
\frac{\partial \sigma_{zz}}{\partial t} = C_{13}\frac{\partial v_x}{\partial x} + C_{23}\frac{\partial v_y}{\partial y} + C_{33}\frac{\partial v_z}{\partial z} \\
\frac{\partial \sigma_{yz}}{\partial t} = C_{44}\left(\frac{\partial v_y}{\partial z} + \frac{\partial v_z}{\partial y}\right) \\
\frac{\partial \sigma_{xz}}{\partial t} = C_{44}\left(\frac{\partial v_x}{\partial z} + \frac{\partial v_z}{\partial x}\right) \\
\frac{\partial \sigma_{xy}}{\partial t} = C_{66}\left(\frac{\partial v_x}{\partial y} + \frac{\partial v_y}{\partial x}\right)
\end{cases}, \tag{69}
$$

where b is the reciprocal of density, v_x ,v_y and v_z represent velocity fields of the x ,y and z components, respectively, σ_{xx} , σ_{yy} and σ_{zz} are normal stresses and σ_{xz}, σ_{xy} and σ_{yz} are the shear stresses. d is the damping parameter. $\boldsymbol{C}$ is the stiffness tensor.

For the stiffness tensor, I used the elastic moduli for magnesite from Table 4 of Yao's 2018 paper (Yao et al., 2018).

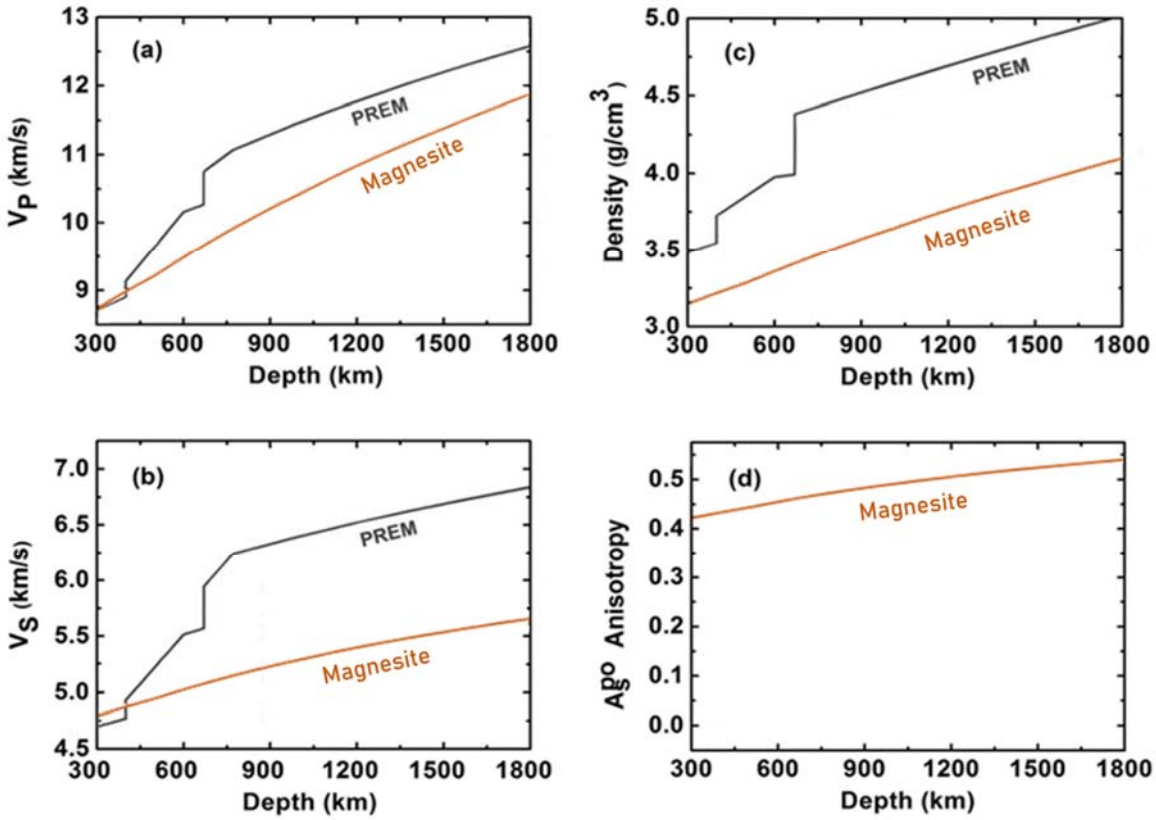

Figure 49. Plots of magnesite compared to the Preliminary Reference Earth Model (PREM). (a) P-wave velocity, (b) S-wave velocity, (c) density, (d) shear elastic anisotropy A_S^{po} of magnesite along a normal mantle geotherm were compared to Preliminary Reference Earth Model (PREM). (Adapted from Yao et al., 2018, Figure. 7).

I assumed that the background matrix is isotropic. Since the subducting slab is colder than the mantle of the same depth, I applied a 5% increase to the P-wave and S-wave velocities (Li et al, 2018) and a 2.5% increase to density(Ganguly et al., 2009) from the PREM model at 500 km depth (Table 3).

I performed 750 models in total, and all models are of the size $200 \times 200 \times 200$ cells with a spacial interval of $2\ m$. The horizontally aligned penny-shaped inclusions are randomly distributed in the models with varying aspect ratios from 0.032 to 0.084, resulting in inclusion volume fraction ranging from 0.018 to 0.1 (Figure 50). Also, the magnesite inclusion of volume fraction 0.1 in this model corresponds to a 4.4 $wt\%\ CO_2$, which is within the reasonable range of most carbon-melting experiments (Dasgupta et al., 2005; Dasgupta et al., 2004; Gerbode and Dasgupta, 2010; Hammouda, 2003; Kelley et al., 2003; Kiseeva et al., 2013; Thomson et al., 2016).

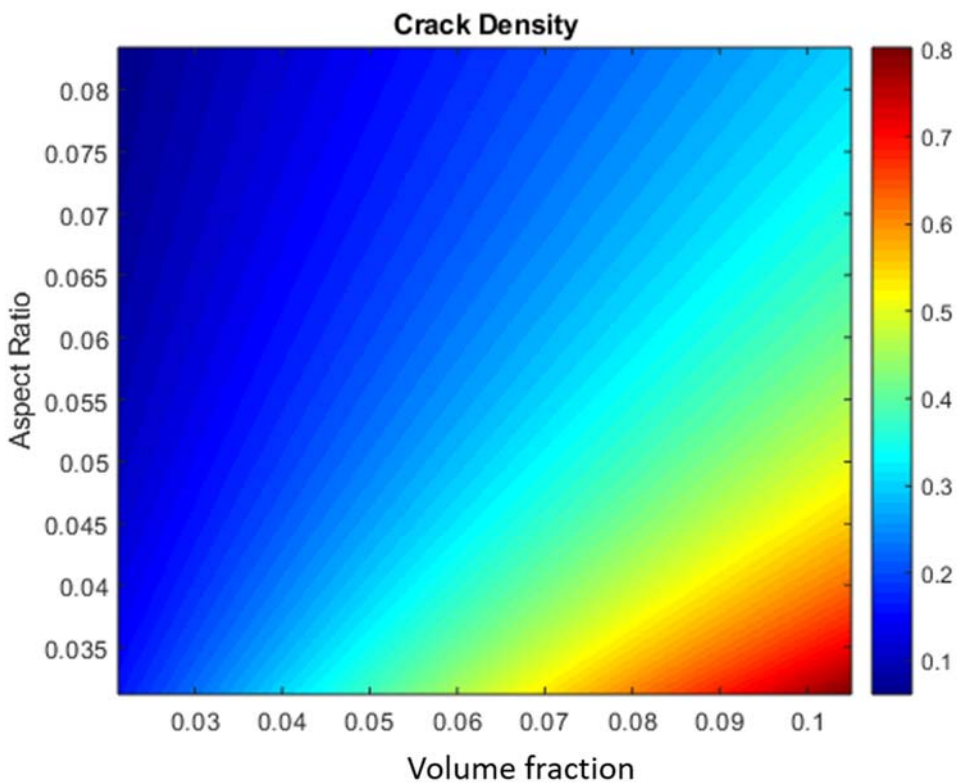

Figure 50. The *crack density* as a function of different volume fractions and aspect ratios of inclusions.

I then modeled carbonatite melt as the inclusion material in the shear anisotropy modeling. I assigned carbonatite melt with shear wave velocity $V_S = 0$ m/s. For the P-wave velocity and density, based on some lab measurements of carbonatite and carbonate melts (Jones, 2013; Andersson et al., 2013), I assumed carbonatite melts are of the P-wave velocity $V_P = 5500$ m/s and density $\rho = 2900$ kg/m^3 (Table 3).

Finally, without assuming any specific material, I varied the inclusion shear velocity to make its shear modulus a portion of 1%-81% of the matrix shear modulus while keeping the density and P-wave velocity the same with the matrix.

Material \ Property		V_P(m/s)	V_S(m/s)	ρ(kg/m3)	A_s^{po}
Matrix		10132.5	5481	3946.3	0
Inclusion	Magnesite	9200	4900	3250	0.45
	Carbonatite melt	5500	0	2900	0

Table 3. Properties for matrix and inclusions used in the modeling of effective γ for penny-shaped inclusion models.

6.3 Results

6.3.1 Modeling results for solid magnesite as inclusion

Figure 51(a)(b) show that for the given properties of magnesite and matrix, the γ value correlates primarily with the inclusion volume fraction, while the inclusion aspect ratio has little influence on the γ values. Even the inclusion volume fraction is as high as 0.1, the maximum γ value is only around 0.055 which is still far less than the strong anisotropy $\gamma = 0.3$ that was inverted from the deep earthquake moment tensors by Li et al., (2018).

Since this model shows an almost linear relationship between the inclusion volume fraction and the γ value (Figure 51(a)), extrapolating the linear trend one can estimate that to achieve a γ value of 0.3, the volume fraction of magnesite should be around 47%, which is not likely to happen in reality.

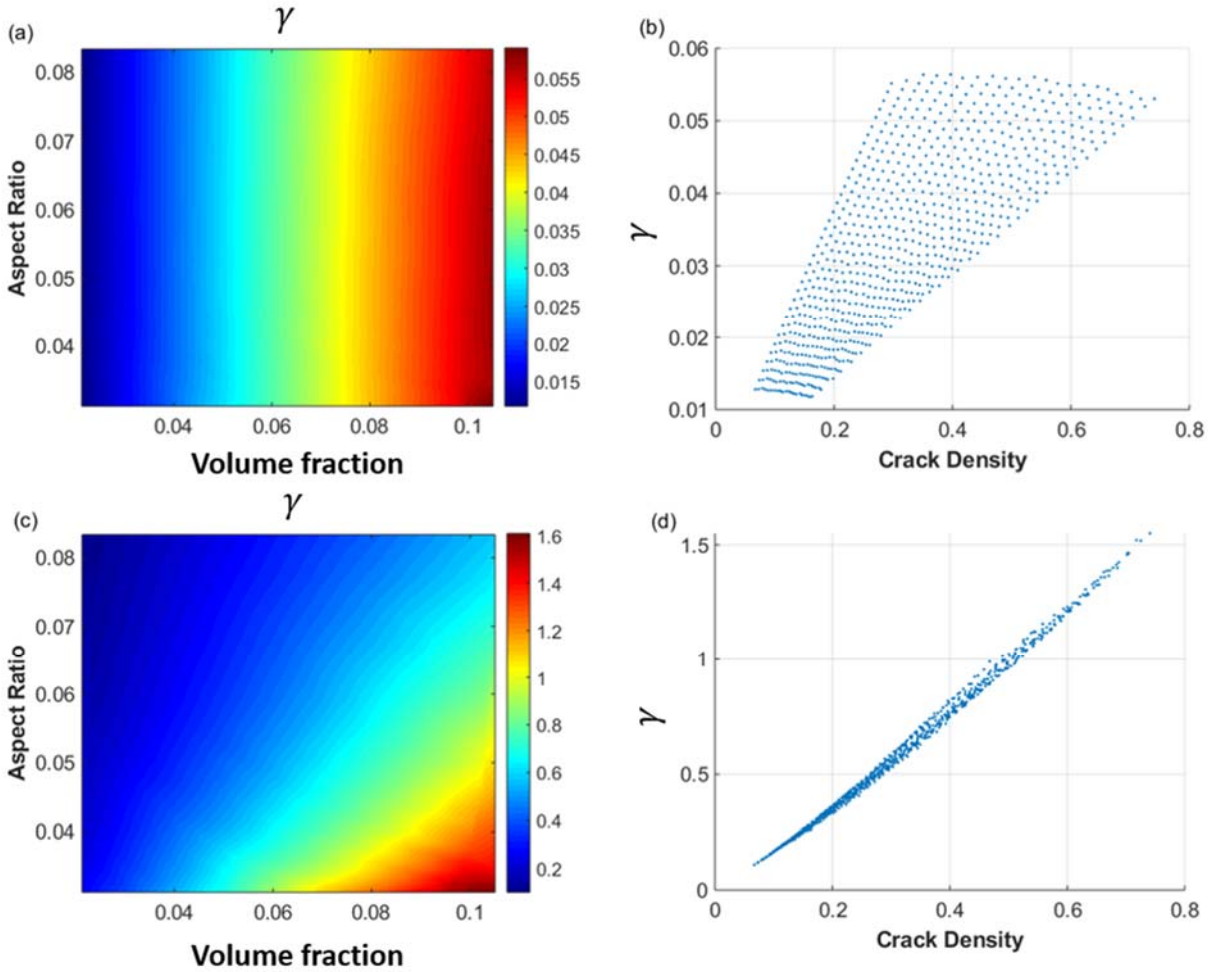

Figure 51. Modeling results for magnesite as inclusions and carbonatite melt as inclusions. (a) γ values for different inclusion volume fractions and inclusion aspect ratios for magnesite inclusion. (b) Scatter plot of γ and *crack density* for all 750 models for magnesite inclusion. (c) γ values for different inclusion volume fractions and inclusion aspect ratios for carbonatite melt inclusion. (d) Scatter plot of γ and *crack density* for all 750 models for carbonatite melt inclusion.

6.3.2 Modeling results for carbonatite melt as inclusion

Figure 51(c)(d) show that high γ values are easily achievable with carbonatite melt as inclusion. A *crack density* as small as 0.2 can result in a γ value of 0.3. Also, the relationship between *crack density* and γ value is almost linear (Figure 51(d)), making Figure 51(c) resemble Figure 50.

6.3.3 Modeling results for variable inclusion shear moduli

Figure 52 shows the relationship between effective γ of the model and *crack density* for different inclusion shear moduli, comparing with the cases when inclusion is magnesite and carbonatite melt, respectively.

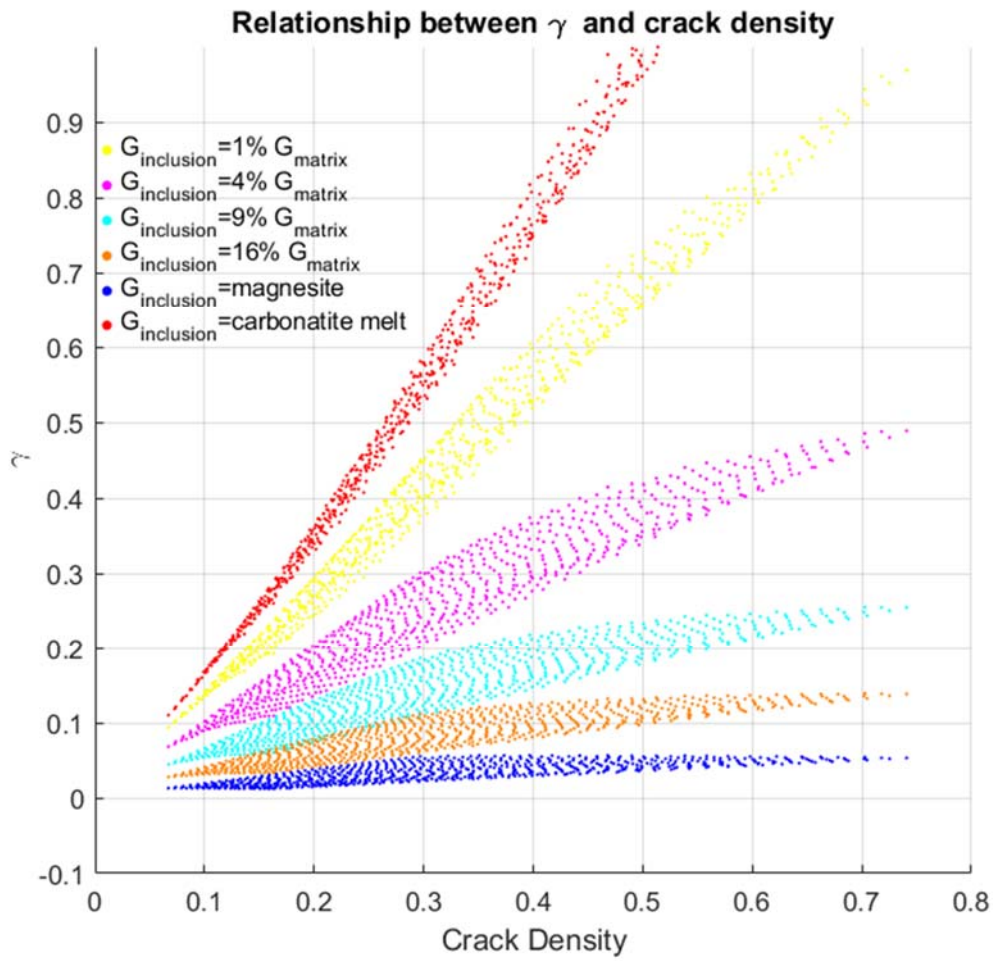

Figure 52. Relationship between effective γ of the model and *crack density*. The color dots represent different shear modulus of inclusions ($G_{inclusion}$), including special cases when inclusion is magnesite and carbonatite melt, respectively.

6.4 Discussions

6.4.1 What inclusion properties can give strong anisotropy?

According to Equation (67), shear anisotropy is purely a function of shear modulus. For the penny-shaped inclusion effective medium model, I kept the matrix property and varied the inclusion shear modulus to test when a γ of 0.3 is achievable. The modeling results are displayed in Figure 53 and Figure 54.

From the results, we can see that when the inclusion shear modulus is less than 9% of the matrix shear modulus, a γ of 0.3 is achievable. If we assume the inclusion is of the same density as the matrix, that means the shear wave velocity of the inclusion should be less than 30% of that of the matrix, i.e., the shear wave velocity of the inclusion should be less than 1644.3 m/s. Even if we consider the γ as a combined anisotropy of magnesite and other inclusions, the shear wave velocity of the inclusion should be quite small. The numerical modeling of the magnesite inclusion shows that it can only contribute up to 5.5% shear anisotropy with 10% volume fraction (Figure 51(a)). If the other inclusion material compensates for the rest 24.5%, it must have a shear modulus of less than around 12% of the matrix shear modulus (Figure 53 and Figure 54(c)(d)). That means, if the inclusion has about the same density as the matrix material, its shear velocity should be less than 35% of that of the matrix, in the situation of 500 km depth, it will be less than 1918.3 m/s. In both cases, the inclusion is most likely a fluid/melt phase.

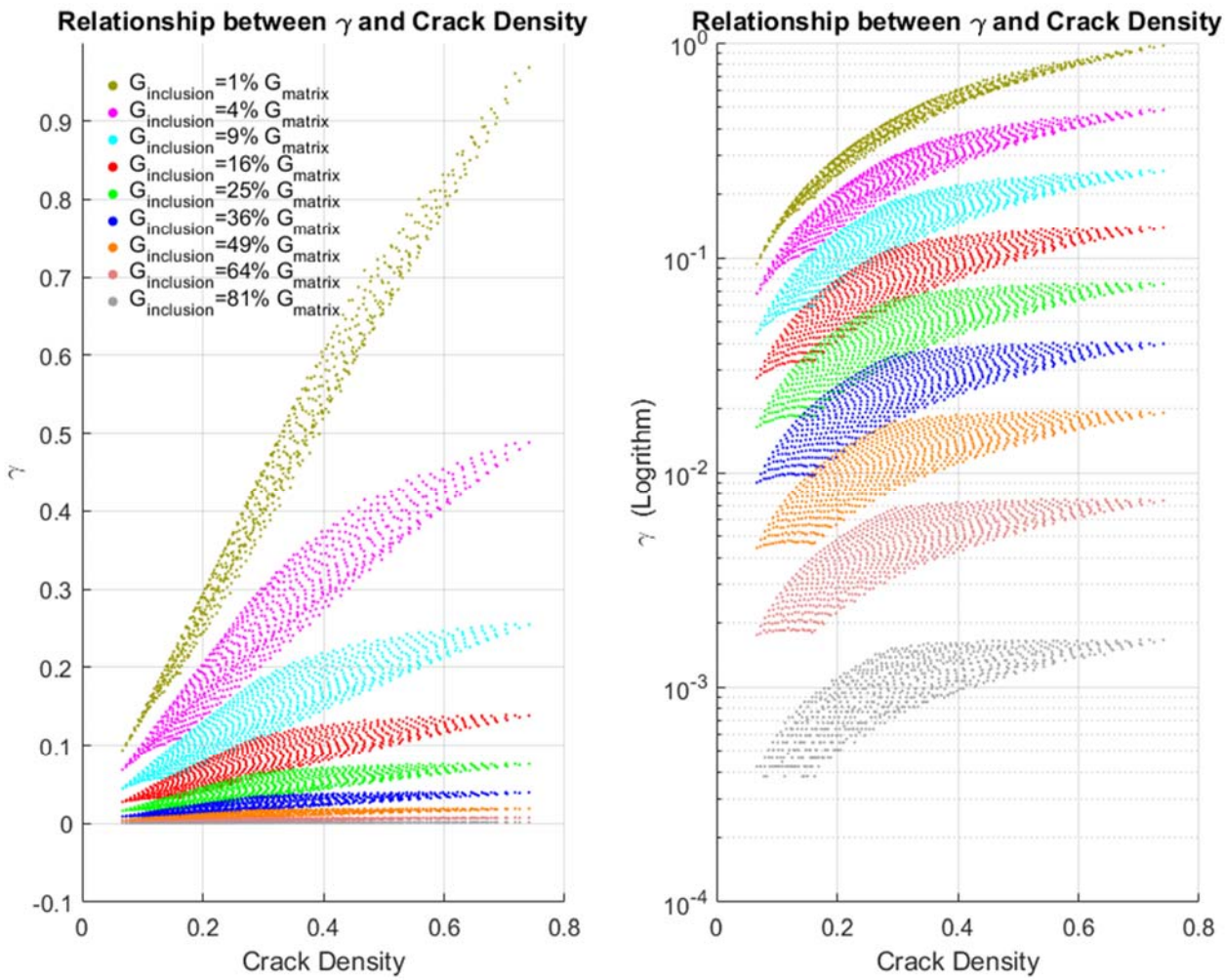

Figure 53. Plots of the γ values for different crack densities in normal (linear) and log scales. Different colors indicate different ratios of shear modulus of the inclusions ($G_{inclusion}$) to that of the matrix(G_{matrix}). (a) is of normal scale; (b) is of logarithmic scale to display the very low γ values.

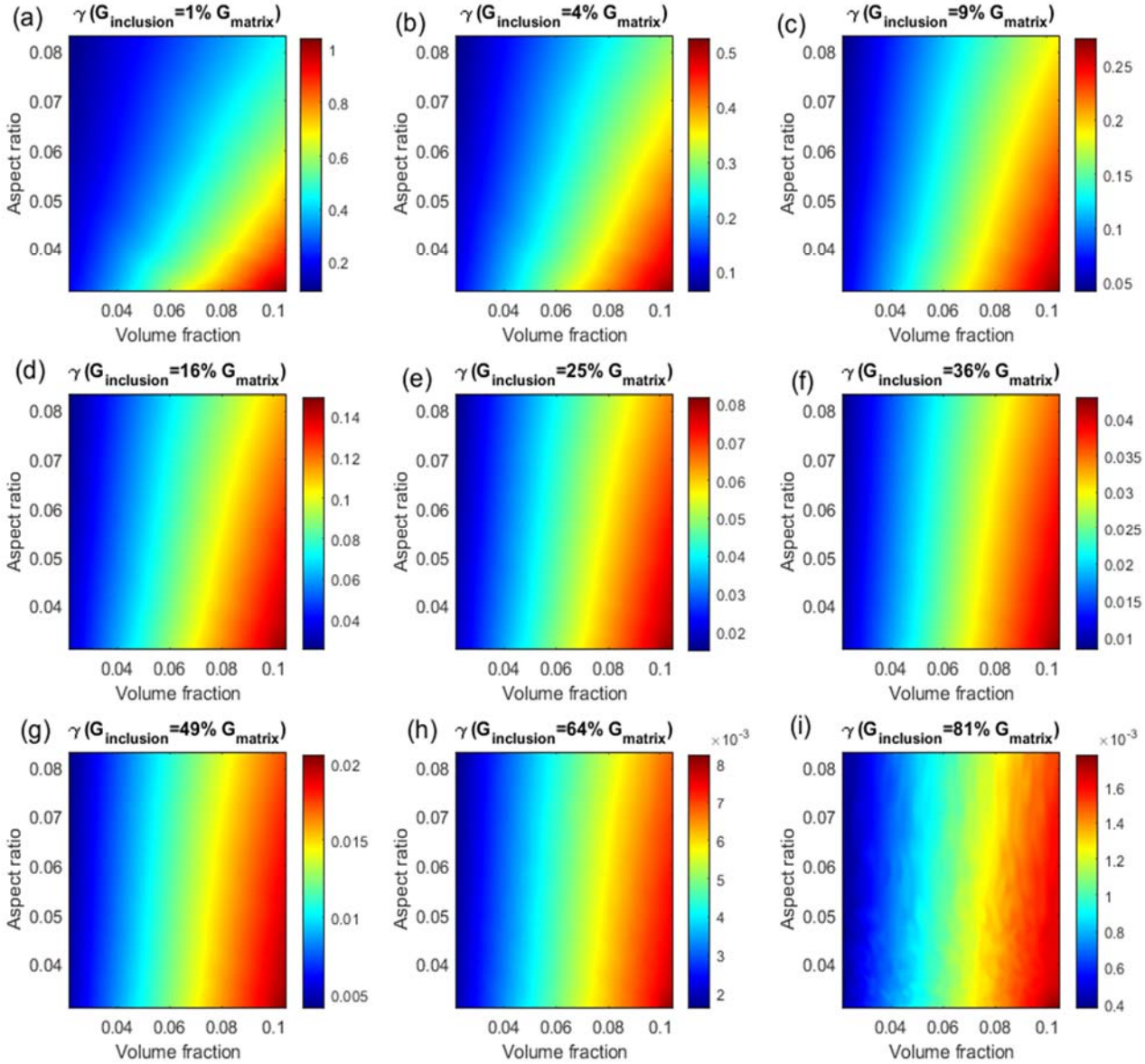

Figure 54. γ values as a function of inclusion volume fractions and aspect ratios. The nine plots correspond to the inclusion shear modulus ($G_{inclusion}$) from 1%~81% of the matrix shear modulus (G_{matrix}).

6.4.2 Can the carbonatite melt cause the anisotropy?

Carbonatite melts are possible inclusions to explain the low shear modulus in the inclusions. Carbonatite melts, or partial melts, are of both lower density and shear wave velocity than its solid phase. Solopova et al., (2015) experimentally studied the melting and decomposition of magnesite, showing that magnesite melt congruently within the studied pressure range 12–84 GPa at temperatures of 2,100–2,650 K. There is no enough evidence showing if these temperature and pressure ranges are achievable at the depth of $300 - 670\ km$ in the subduction zones of Tonga (TG), Molucca (MO) and Mariana–Japan–Kuriles (MJK) where the high shear anisotropy was observed. If these conditions are true for these study areas, it is possible that part of the magnesite is melted or partially melted as inclusions.

Thomson et al., (2016) provided a melting curve of carbonated subducting slabs. From their study, all subducting slabs, no matter cold or hot, enter the carbonatite melting zone at or near the transition zone depths. The carbonatite melt can be part of the inclusions to cause high shear anisotropy. That can explain why even an old and cold slab (Seton et al., 2012) as TG can have carbonatite melting on its surface and generate high shear anisotropy.

From Li et al., (2018) , the laminated rock fabric that caused the high shear anisotropy is either parallel or perpendicular to the slab surface. It implies that the driving force for the melting migration should possibly be shear stress, not buoyancy. The melts may not be fully connected with each other to form melt migration flux. They might be isolated and trapped locally due to the low permeability of the matrix rock.

6.5 Conclusions

From the numerical modeling, I derived the relationship between inclusion volume fraction, aspect ratio, shear modulus and the slab shear anisotropy γ, based on the penny-shaped inclusion model assumption. If the anisotropy is caused by the carbonatite melt, we can have some estimations about the carbon amount stored. To achieve the observed γ of 0.3, the inclusion shear modulus should be less than 10% of the matrix shear modulus (Figure 54 (a)(b)(c)). Roughly, the shear anisotropy γ linearly depends on the *crack density*, or the ratio ϕ / α (Figure 53). I can constrain the ratio but not the respective values of ϕ and α. For example, for an inclusion with shear modulus equals to 1% of the matrix shear modulus, the *crack density* should be around 0.2 (Figure 53). If the inclusion aspect ratio is 0.03, the carbonatite melt volume fraction should be ~2.5% (Figure 54(a)). If the aspect ratio is 0.01, we can extrapolate the trend to get a ~0.8% melt volume fraction. If the aspect ratio can be estimated through another independent method, based on the relationship I derived, one can put more constraints on the carbon amount stored in the subducting slab.

CHAPTER 7 IMPROVING SUBSALT SEDIMENT IMAGING AND HIGH ANGLE FAULTS USING SECONDARY SCATTERED SEISMIC WAVES

Steeply dipping faults, salt flanks, and subsalt sediments are important geological structures in energy exploration. Conventional seismic imaging in such areas is known to have challenges in imaging those features, due to poor illumination because of the use of singly scattered waves/primary reflections. In this chapter, I used multiply scattered waves, especially the secondary scattered waves, in the reverse time migration (RTM), to enhance the seismic illumination for imaging the steep faults and subsalt areas. I applied the method on two synthetic models, a trapezoidal model and the Sigsbee2B model. These two synthetic examples demonstrate that the new method achieves better imaging of steep faults and subsalt areas than the traditional RTM.

7.1 Methodology

In the secondary scattering method, the scatterers will serve as new wave-radiating sources activated by the incident wave. They emit waves to reach the “shadow zones”, then the secondary scattered waves can be recorded by the surface receivers. One typical “shadow zone” is the high angle fault (Figure 55). The secondary scattered waves can illuminate the high angle fault where primary scattered waves are not able to reach (Figure 55).

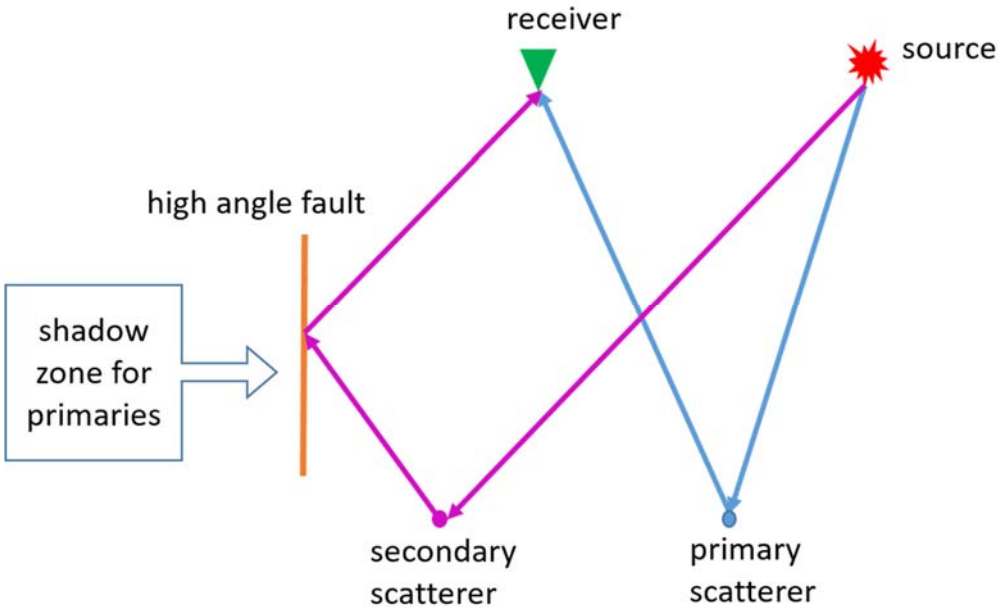

Figure 55. Raypaths of primary scattered waves (blue) and secondary scattered waves (magenta). The secondary scattered waves illuminate the high angle fault where primary scattered waves are not able to reach. In the primary reflection case, the wave from the source hits the "primary scatterer" and then directly goes to the receiver. In the secondary scattering path, the wave hits the scatterer first, then reflected by the high angel fault, and then goes to the receiver.

In seismic data processing, the migration velocity is usually a smoothed model, built using seismic tomography and possibly with other geologic and wellbore *a priori* information. Conventional RTM using a smoothed migration model is able to image using primary reflections (or called singly-scattered waves) and turning waves. (Reflection is the constructive interference of scattering. Suppose the obstacle is a plate, only when the radius of the plate is far smaller than the first Fresnel zone, it could be considered as a scatterer. Otherwise, it is a reflector.) The wave propagation in such a smoothed model usually cannot generate multiply scattered waves. Therefore, the conventional RTM image is an image produced by primary reflections. On the other hand, multiply scattered waves, especially secondary scattered waves usually interact with high-angle faults and subsalt structures and are indeed recorded by surface receivers. Because the multiples do not follow the primary-reflection paths, seismic migration using a smoothed model does not properly account for the kinematics of the multiples.

Hence I proposed the following imaging procedures to use recorded multiply scattered waves for imaging high-angle faults and subsalt areas where primary reflections can hardly illuminate. In this dissertation, I only discussed the acoustic wave RTM.

Firstly, I ran the conventional RTM. The conventional RTM of singly scattered waves with cross-correlation imaging condition could be expressed as

$$I_p(\boldsymbol{x}) = \sum_{\boldsymbol{x_s}} \int S(\boldsymbol{x_s}, \mathbf{v}, \boldsymbol{\rho}; \boldsymbol{x}, t) R(\boldsymbol{x_r}, \mathbf{v}, \boldsymbol{\rho}; \boldsymbol{x}, t) dt, \tag{70}$$

where $\boldsymbol{x}$ is the subsurface image point location; $\boldsymbol{x_s}$ and $\boldsymbol{x_r}$ are the source and receiver locations, respectively; t is time; S and R represent the forward propagated source wavefield and backward

propagated receiver wavefield, respectively; I_p is the image stacked from all shot gathers; $\mathbf{v}$ and $\boldsymbol{\rho}$ are the velocity and density models used in wave propagation, respectively. For the wavefield propagation (S and R), I used the staggered grid finite difference scheme to solve the full-wave acoustic wave equation (Virieux, 1986b).

Secondly, after I got the image, I identified the reflective features such as geological layer boundaries and discontinuities where potential point scatterers could be placed to illuminate the targeted structure. I put these artificial density scatterers to generate the forward propagated secondary scattered waves. These forward propagated scattered waves correlated with the receiver-side backward propagated waves at the high angle fault and salt flanks so that they could illuminate these areas (See Figure 55). In addition, the artificial density point scatterers would not change the traveltime of the primary wavefields and therefore would not reduce the spatial accuracy of the image. This procedure could be described by the following equation:

$$I_{pm}(\boldsymbol{x}) = \sum_{\boldsymbol{x_s}} \int S'(\boldsymbol{x_s}, \mathbf{v}, \boldsymbol{\rho}'; \boldsymbol{x}, t) R(\boldsymbol{x_r} \mathbf{v}, \boldsymbol{\rho}; \boldsymbol{x}, t) dt, \tag{71}$$

where I_{pm} is the image of primary reflections and multiply scattered waves; S' is the forward propagated source wavefield based on the migration velocity $\mathbf{v}$ and a new density model $\boldsymbol{\rho}'$. The new density model $\boldsymbol{\rho}'$ is built from the previous density model $\boldsymbol{\rho}$ by adding artificial positive density perturbations as secondary scatterers.

Thirdly, I extracted the image of multiply scattered waves I_m by subtracting the I_p from I_{pm}:

$$I_m(\boldsymbol{x}) = I_{pm}(\boldsymbol{x}) - I_p(\boldsymbol{x}). \tag{72}$$

The amplitude of I_m would be much smaller than I_p. One could enhance the amplitude of I_m using a scaling factor to match it with the amplitude of I_p and generate a new image I_{new}:

$$I_{new}(\boldsymbol{x}) = I_p(\boldsymbol{x}) - \alpha I_m(\boldsymbol{x}), \tag{73}$$

where α is a scaling factor that can be estimated from the ratio of maximums in I_p and I_m.

Consequently, the image I_{new} contained both the traditional RTM image due to primary reflections and the image of steep faults and subsalt areas due to the secondary scattering.

I summarized the workflow of my proposed method as:

1) Get the smoothed migration velocity model $\mathbf{v}$ and constant density model $\boldsymbol{\rho}$;

2) Perform the conventional RTM (Equation (70)) and obtain the image I_p;

3) Based on image I_p, identify possible locations for scatterers (e.g., layer interface, sharp topography, etc.) around the targeted structure;

4) Build a new density model $\boldsymbol{\rho}'$ by setting the artificial point scatterers as density perturbations;

5) Perform the RTM with the new density model $\boldsymbol{\rho}'$ for the source-side wavefield using Equation (71) and obtain I_{pm}; For computing the receiver-side wavefield, one could use the original density model;

6) Extract the image I_m of multiply scattered waves with Equation (72);

7) Calculated the scaling factor and generate the final image I_{new} with Equation (73).

7.2 Results

7.2.1 Trapezoidal model

A trapezoidal model (Figure 56(a)) was built to demonstrate the limitation of the conventional RTM and the effectiveness of the secondary scattering RTM. The true model was a 2D two-layered sedimentary model. Each layer was homogeneous and isotropic. A high velocity homogeneous and isotropic trapezoidal anomaly was embedded in the upper layer (Figure 56(a)). To measure the reflection seismic response of such model, 75 point sources with 6 Hz Ricker wavelet were evenly distributed at the surface from $0 - 7.4\ km$ with 100 m interval. Receivers were deployed on the surface from $0 - 10\ km$ with a $10\ m$ interval.

The conventional RTM with the smoothed velocity model uses mainly primary waves and is difficult to image the near-vertical salt flank. The 75 shot gathers were migrated using the smoothed migration velocity (Figure 56(b)) by the conventional RTM method. The migrated image (Figure 56(c)) shows the top and the left side low angle flank of the salt body, but the vertical salt flank to the right side was not imaged.

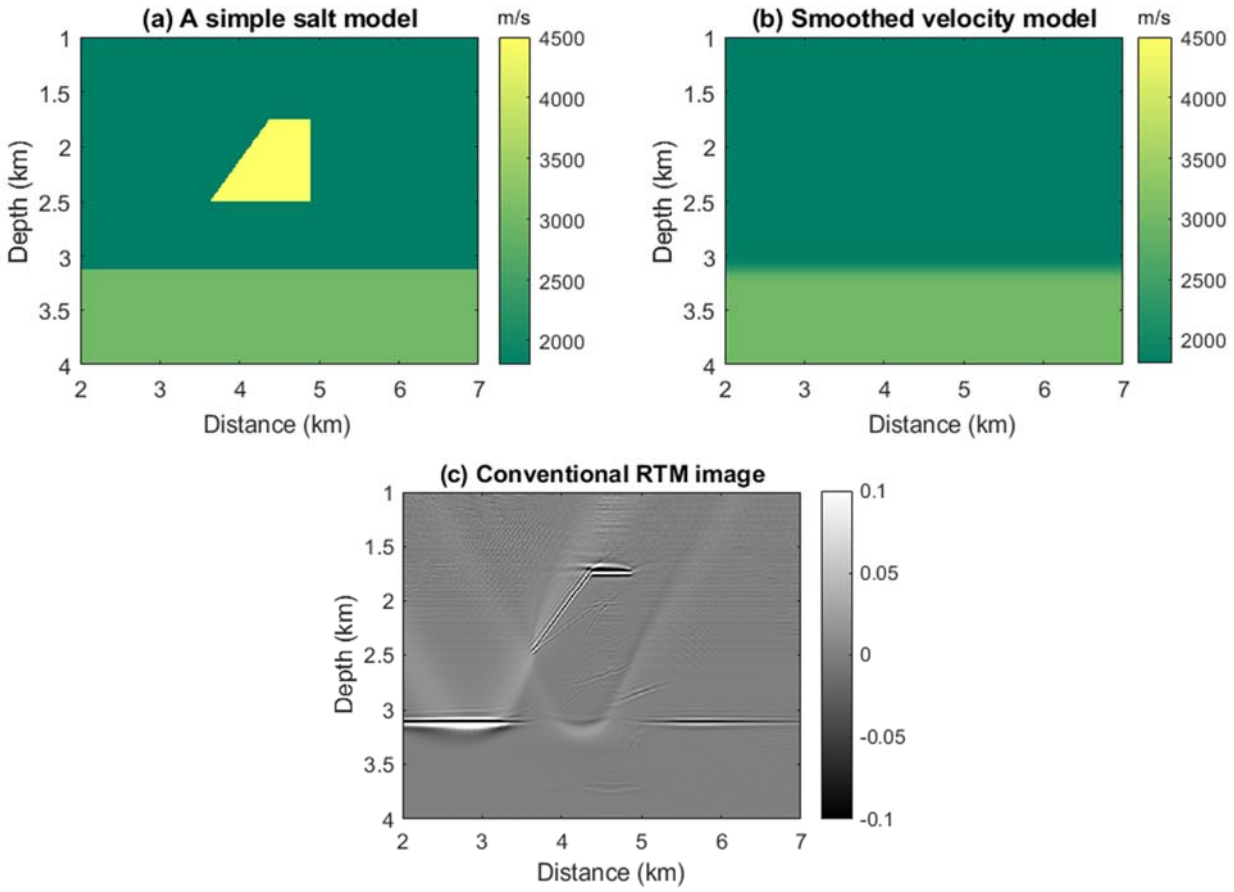

Figure 56. (a) The trapezoidal velocity model for the case study. (b) The smoothed migration velocity model without salt used in RTM. (c) Conventional RTM image.

Based on the migration image from the conventional RTM (Figure 56(c)), a density point scatterer whose density was 10 times of the constant background density was placed to the right side of the salt body on the interface of the two sediment layers (Figure 57(a)), where the secondary scattering might illuminate the right flank of the salt. The secondary scattering image (Figure 57(b)) was obtained by subtraction of the conventional RTM image (Figure 56(c)) from the RTM migration image with that one scatterer added. The single scatterer effectively illuminated the right vertical flank of the trapezoidal model. The final image (Figure 57(c)) was

obtained by linearly combining the primary reflection image and the secondary scattering image based on Equation (73).

The advantage of placing a small number of scatterers rather than a reflector surface is that scatterers emit waves in all directions, but a specular reflector reflects waves in certain directions. In addition, the density point scatterers will not distort the migrated images. A natural problem to investigate is what happens if one places the point scatterers randomly, not on an imaged boundary or some scattering features. I placed point scatterers inside the first layer instead of on the interface of the two layers (Figure 58(a)). Some minor image artifacts were introduced in the secondary scattering image (Figure 58(b)). However, the final image (Figure 58(c)) did not change much compared to the results obtained by placing the point scatterers on the layer boundary (Figure 57(c)). The vertical salt flank could still be interpreted (Figure 58(c)). If one put the scatterer to a wrong location, it will not generate a wrong image, because the source-side secondary scattering wavefield and the receiver-side wavefield will not coincide at the image location.

Both the conventional (Figure 56(c)) and secondary scattering RTM (Figure 57(c) and Figure 58(c)) cannot image the salt bottom clearly because I used the smoothed migration velocity model without salt. Therefore, the traveltime from the source side and the receiver side did not coincide at the bottom of the salt. To better image the bottom boundary of the salt, a progressive imaging process with salt flooding strategy is further needed but is out of the scope of this paper.

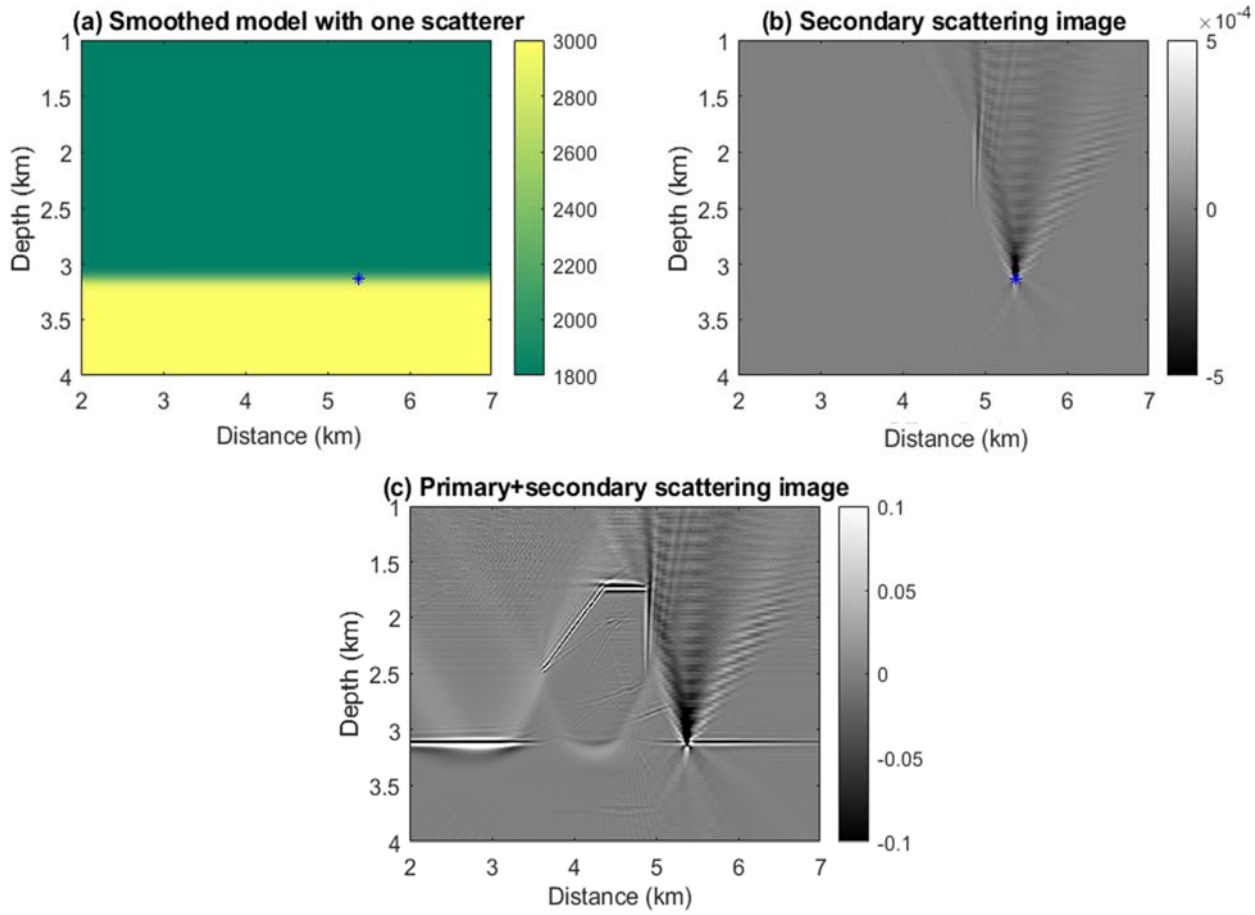

Figure 57. (a) The migration velocity model with a single density point scatterer (indicated by the blue star) for secondary scattering image generation. (b) The image of secondary scattering only, I_m (Equation (72)). (c) Linear combination of primary and secondary scattering image with a scaling factor of α=200 (Equation (73)) on the secondary scattering image.

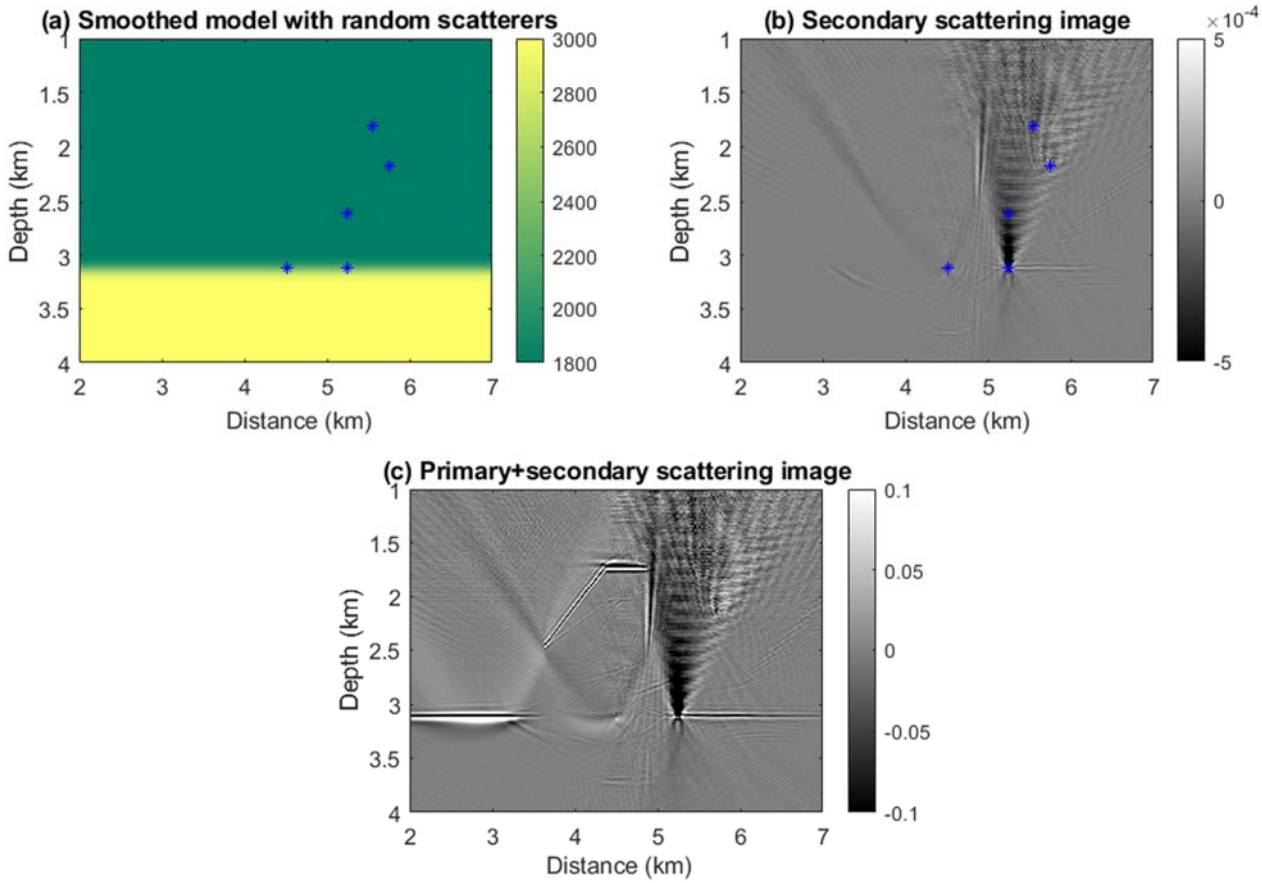

Figure 58. (a) Multiple density point scatterers (indicated by the blue stars) are placed in the smoothed migration velocity model. (b) The image of secondary scattering only, I_m (Equation (72)). (c) Linear combination of primary and secondary scattering image with a scaling factor of α=200 (Equation (73)) on the secondary scattering image.

7.2.2 Sigsbee2B model

I applied our proposed methodology on the Sigsbee2B model which is constructed to help understand the imaging issues observed subsalt (Paffenholz et al., 2002). The model (Figure 59(a)) had a $25\ ft$ grid spacing in both the horizontal and depth directions. The seismic survey had 500 shots, from distance $925\ ft$ to $75775\ ft$, with a shot interval of $150\ ft$. The maximum number of receivers per shot was 348, with a receiver interval of $75\ ft$. Both the sources and

receivers were at 25 ft depth. The recording length was 12 $seconds$ with a sampling rate of 8 $miliseconds$. The Sigsbee2B model is known for its illumination problems below the salt. Using a smoothed velocity model (Figure 59(b)), I obtained a conventional RTM image (Figure 60(a)) and its subsalt area (arrows in Figure 60(b)) could not be imaged clearly.

Two configurations of point scatterers (Figure 61(a) and Figure 62(a)) with density ratio 10:1 to the constant background density were placed around the subsalt sediments to improve the illumination of that area. The results (Figure 61(b) and Figure 62(b)) showed that the secondary scattering waves much better imaged the sediments right beneath the salt which were not imaged well on the conventional RTM image. I stacked the two images from the two sets of point scatterers to increase the signal to noise ratio (SNR) (Figure 63(a)). The sediment layers imaged by the secondary scattering correlated well with the reflectivity model of Sigsbee2B (Figure 63(b)).

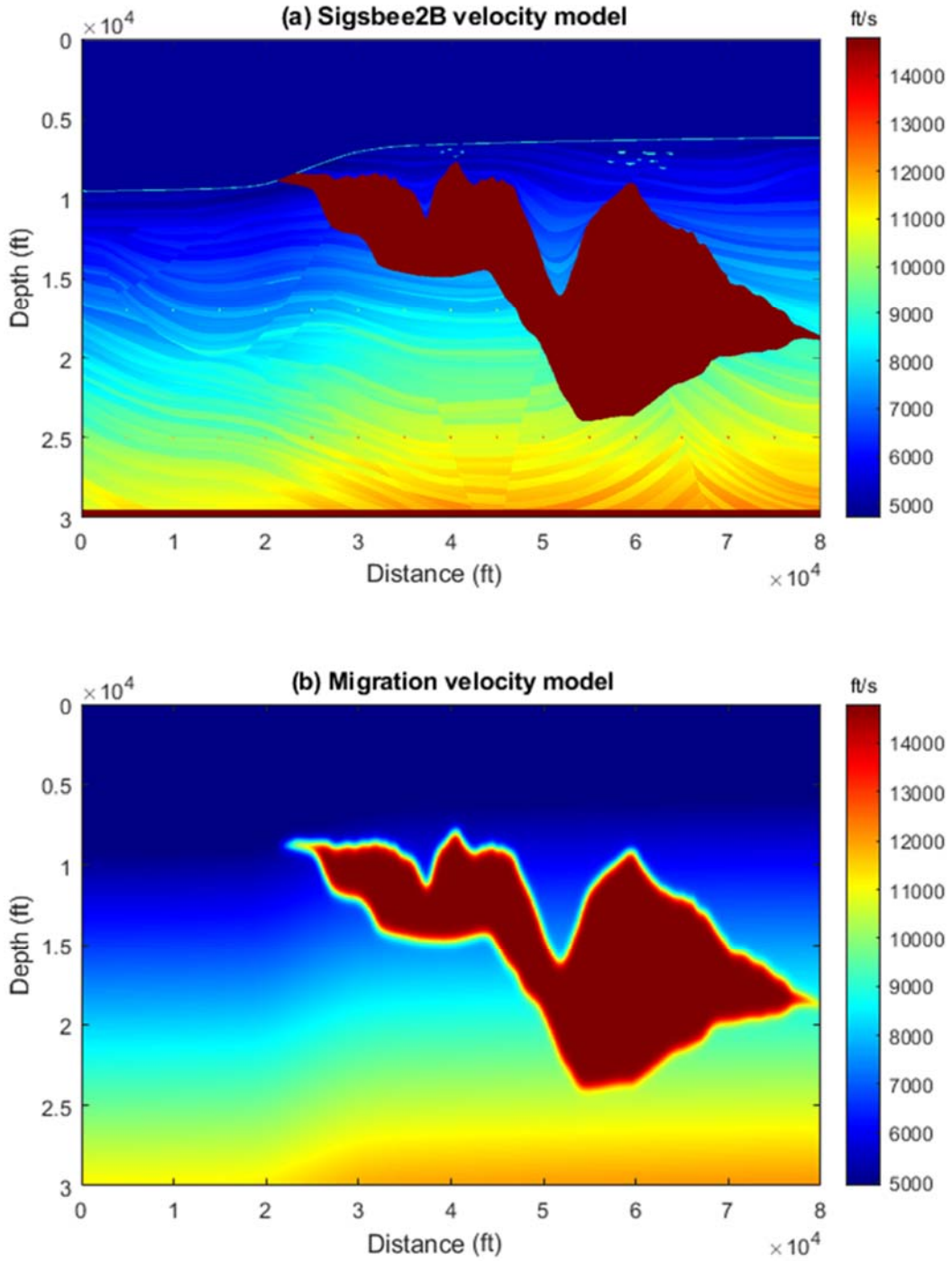

Figure 59. (a) Sigsbee2B velocity model. (b) The smoothed velocity model used in RTM.

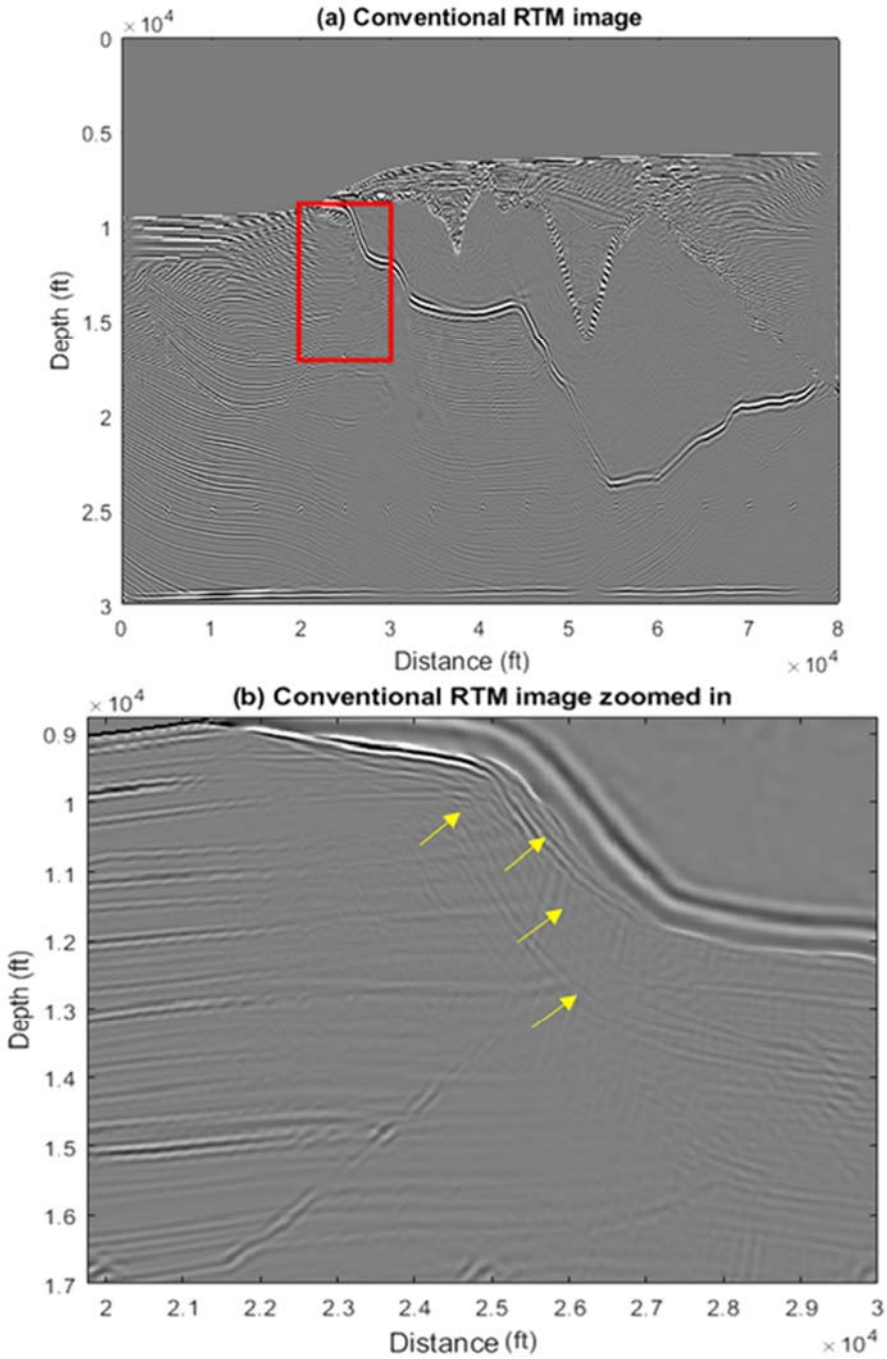

Figure 60. (a) Conventional RTM image. (b) Zoomed in the area from the red rectangle in (a) with arrows indicating poor illuminations in the subsalt area.

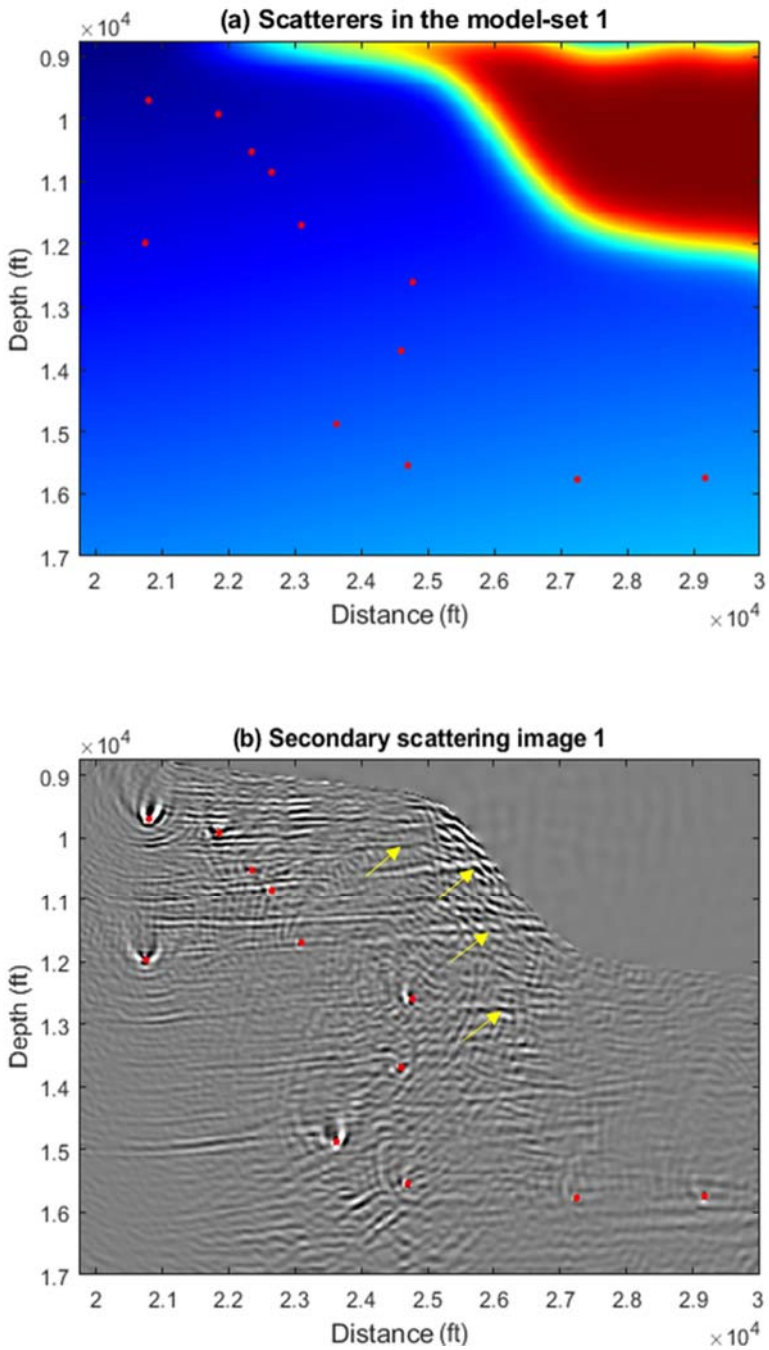

Figure 61. (a) The first set of scatterers (indicated by red dots) are placed at the subsalt area. (b) Secondary scattering image produced by scatterers in (a). Some of the improvements are marked by the yellow arrows.

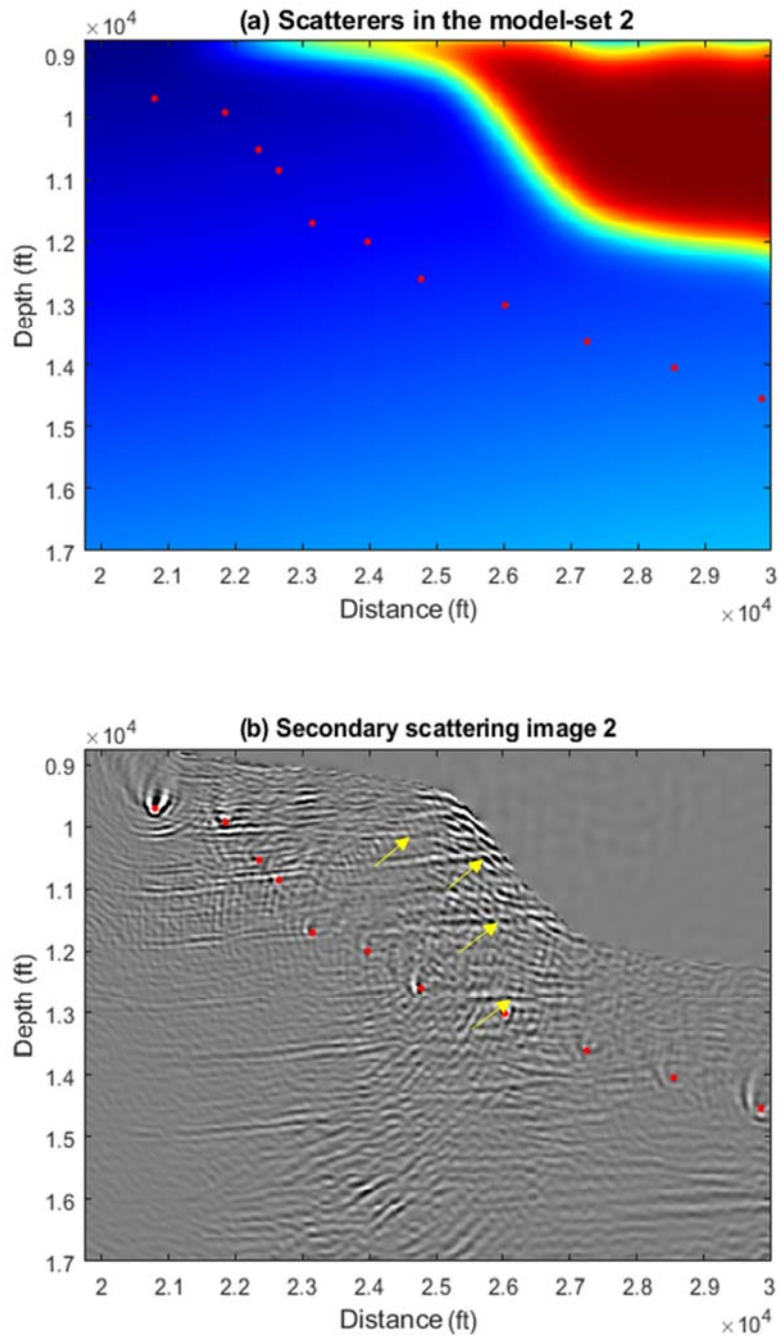

Figure 62. (a) The second set of scatterers (indicated by red dots) are placed at the subsalt area. (b) Secondary scattering image produced by scatterers in (a). Some of the improvements are marked by the yellow arrows.

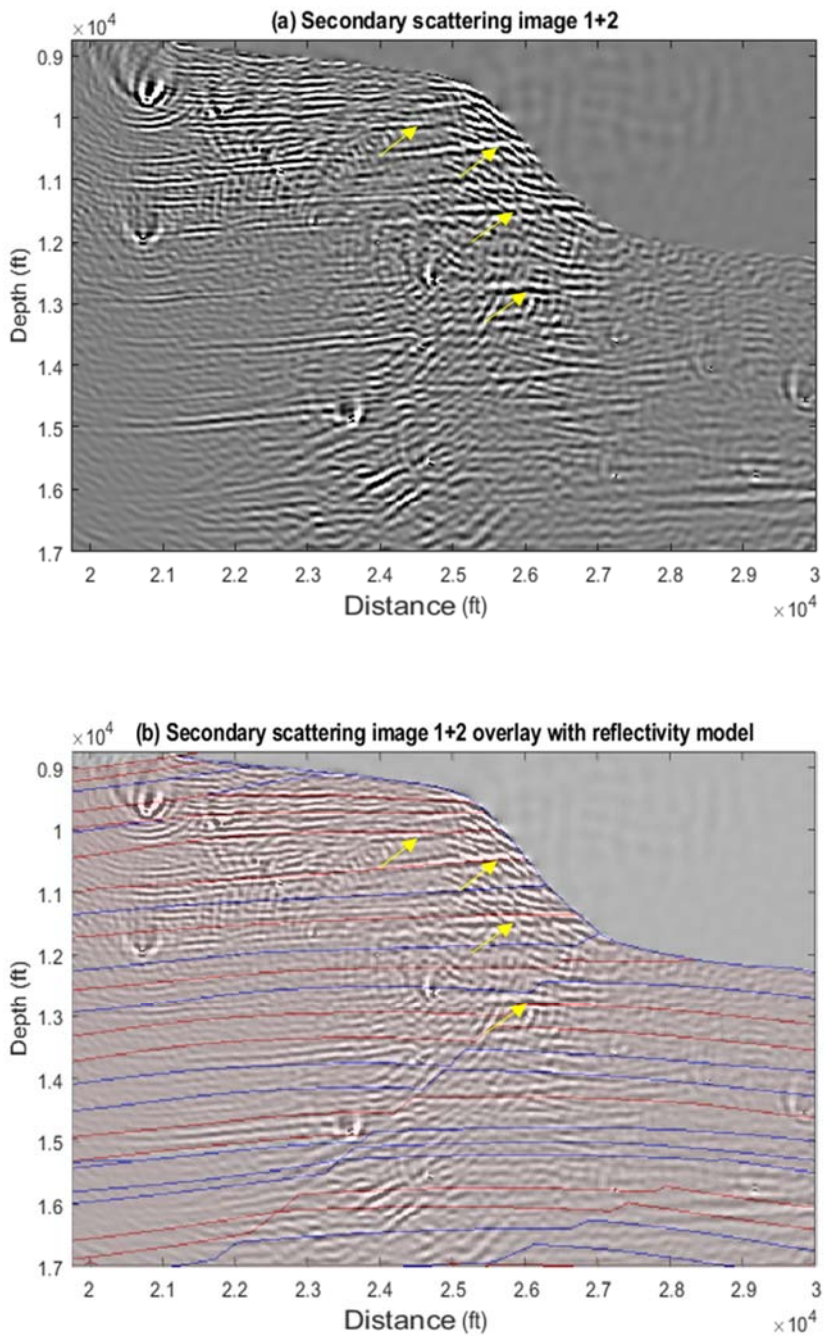

Figure 63. (a) The stacked image from Figure 61(b) and Figure 62(b). (b) The overlay of Sigsbee2B reflectivity model and (a). The blue and red lines represent the reflectors. The reflectors correlate well with the sediments imaged from the secondary scattering.

7.3 Conclusions

I modified the conventional RTM workflow to use secondary scattering waves to better image high angle faults, salt flanks, and subsalt sediments. The secondary scattering RTM workflow showed better imaging results at illumination shadow zones that cannot be reached by primary reflections. I verified the proposed methodology using a two-layered trapezoidal salt model with a vertical salt flank and the Sigsbee2B model. For the two-layered trapezoidal salt model, I showed that a single secondary source could illuminate/image the vertical flank. On the other hand, randomly placing several scatterers in the model did not deteriorate the image quality. For the Sigsbee2B model, the imaging challenge is in the subsalt where primary reflections cannot reach. My methodology showed a great improvement on the subsalt image so that interpreters can properly identify the relationship between the salt intrusion and the sedimentary layers.

BIBLIOGRAPHY

Aki, K., and P. G. Richards, 1980, Quantitative seismology : theory and methods. 2 vols, Series of books in geology: W. H. Freeman.

Backus, G. E., 1962, Long-Wave Elastic Anisotropy Produced by Horizontal Layering: Journal of Geophysical Research, **67**, no. 11, 4427-4440.

Baysal, E., D. D. Kosloff, and J. W. C. Sherwood, 1983, Reverse Time Migration: Geophysics, **48**, no. 11, 1514-1524.

Bina, C. R., and B. J. Wood, 1987, Olivine‐spinel transitions: Experimental and thermodynamic constraints and implications for the nature of the 400‐km seismic discontinuity: Journal of Geophysical Research: Solid Earth, **92**, no. B6, 4853-4866.

Blackstock, D. T., 2000, Fundamentals of physical acoustics: Wiley.

Cheng, C., 1993, Crack models for a transversely isotropic medium: Journal of Geophysical Research: Solid Earth, **98**, no. B1, 675-684.

Dai, W., and G. T. Schuster, 2013, Reverse time migration of prism waves for salt flank delineation, SEG Technical Program Expanded Abstracts 2013, 3861-3865.

Dasgupta, R., and M. M. Hirschmann, 2010, The deep carbon cycle and melting in Earth's interior: Earth and Planetary Science Letters, **298**, no. 1-2, 1-13.

Dasgupta, R., M. M. Hirschmann, and A. C. Withers, 2004, Deep global cycling of carbon constrained by the solidus of anhydrous, carbonated eclogite under upper mantle conditions: Earth and Planetary Science Letters, **227**, no. 1-2, 73-85.

Dasgupta, R., M. M. Hirschmann, and N. Dellas, 2005, The effect of bulk composition on the solidus of carbonated eclogite from partial melting experiments at 3 GPa: Contributions to Mineralogy Petrology, **149**, no. 3, 288-305.

Ding, Y., Y. Zheng, and H.-w. Zhou, 2019, An asymmetrical reverse time migration (asym-RTM) scheme to image high-angle faults, SEG Technical Program Expanded Abstracts 2019, 4720-4724.

Dziewonski, A. M., and D. L. Anderson, 1981, Preliminary reference Earth model: Physics of the earth planetary interiors, **25**, no. 4, 297-356.

Ekström, G., M. Nettles, and A. Dziewoński, 2012, The global CMT project 2004–2010: Centroid-moment tensors for 13,017 earthquakes: Physics of the earth planetary interiors, **200**, 1-9.

Eshelby, J. D., 1957, The determination of the elastic field of an ellipsoidal inclusion, and related problems: Proceedings of the royal society of London. Series A. Mathematical physical sciences, **241**, no. 1226, 376-396.

Fang, X. D., M. C. Fehler, and A. Cheng, 2014, Simulation of the effect of stress-induced anisotropy on borehole compressional wave propagation: Geophysics, **79**, no. 4, D205-D216.

Farmer, P. A., I. F. Jones, H. Zhou, R. I. Bloor, and M. C. J. F. B. Goodwin, 2006, Application of reverse time migration to complex imaging problems, **24**, no. 9.

Fjaer, E., 2008, Petroleum related rock mechanics. 2nd ed, Developments in petroleum science: Elsevier.

Ganguly, J., A. M. Freed, and S. K. Saxena, 2009, Density profiles of oceanic slabs and surrounding mantle: Integrated thermodynamic and thermal modeling, and implications for the fate of slabs at the 660 km discontinuity: Physics of the earth planetary interiors, **172**, no. 3-4, 257-267.

Garboczi, E. J. 1998, Finite element and finite difference programs for computing the linear electric and elastic properties of digital images of random materials.

Gerbode, C., and R. Dasgupta, 2010, Carbonate-fluxed melting of MORB-like pyroxenite at 2· 9 GPa and genesis of HIMU ocean island basalts: Journal of Petrology, **51**, no. 10, 2067-2088.

Green, H. W., W.-P. Chen, and M. R. Brudzinski, 2010, Seismic evidence of negligible water carried below 400-km depth in subducting lithosphere: Nature, **467**, no. 7317, 828-831.

Gregory, R. D., 2006, Classical mechanics : an undergraduate text: Cambridge University.

Hammouda, T., 2003, High-pressure melting of carbonated eclogite and experimental constraints on carbon recycling and storage in the mantle: Earth Planetary Science Letters, **214**, no. 1-2, 357-368.

Hashin, Z., and S. Shtrikman, 1961, Note on a Variational Approach to the Theory of Composite Elastic Materials: Journal of the Franklin Institute-Engineering and Applied Mathematics, **271**, no. 4, 336-&.

Hayes, J. M., and J. R. Waldbauer, 2006, The carbon cycle and associated redox processes through time: Philosophical Transactions of the Royal Society B: Biological Sciences, **361**, no. 1470, 931-950.

He, Y., and R. S. Wu, 2009, Subsalt imaging using secondary scattered waves, SEG Technical Program Expanded Abstracts 2009, 1657-1661.

Holyoke, C. W., A. K. Kronenberg, J. Newman, and C. Ulrich, 2014, Rheology of magnesite: Journal of Geophysical Research: Solid Earth, **119**, no. 8, 6534-6557.

Hudson, J. 1980, Overall properties of a cracked solid. Paper read at Mathematical Proceedings of the Cambridge Philosophical Society.

Jaeger, J. C., N. G. Cook, and R. Zimmerman, 2009, Fundamentals of rock mechanics: John Wiley & Sons.

Jin, S., S. Xu, and D. Walraven, 2006, One-return wave equation migration: Imaging of duplex waves, SEG Technical Program Expanded Abstracts 2006: Society of Exploration Geophysicists, 2338-2342.

Karato, S., H. Jung, I. Katayama, and P. Skemer, 2008, Geodynamic significance of seismic anisotropy of the upper mantle: New insights from laboratory studies: Annual Review of Earth and Planetary Sciences, **36**, 59-95.

Kelemen, P. B., and C. E. Manning, 2015, Reevaluating carbon fluxes in subduction zones, what goes down, mostly comes up: Proceedings of the National Academy of Sciences, **112**, no. 30, E3997-E4006.

Kelley, K. A., T. Plank, J. Ludden, and H. Staudigel, 2003, Composition of altered oceanic crust at ODP Sites 801 and 1149: Geochemistry, Geophysics, Geosystems, **4**, no. 6.

Kelly, K. R., R. W. Ward, S. Treitel, and R. M. Alford, 1976, Synthetic seismograms: A finite-difference approach: Geophysics, **41**, no. 1, 2-27.

Kiseeva, E. S., K. D. Litasov, G. M. Yaxley, E. Ohtani, and V. S. Kamenetsky, 2013, Melting and phase relations of carbonated eclogite at 9–21 GPa and the petrogenesis of alkali-rich melts in the deep mantle: Journal of Petrology, **54**, no. 8, 1555-1583.

Kryvohuz, M., and H. Kuehl, 2019, Least-squares reverse time migration with prism waves, SEG Technical Program Expanded Abstracts 2019: Society of Exploration Geophysicists, 4575-4579.

Levander, A. R., 1988, Fourth-order finite-difference P-SV seismograms: Geophysics, **53**, no. 11, 1425-1436.

Li, J., Y. Zheng, L. Thomsen, T. J. Lapen, and X. Fang, 2018, Deep earthquakes in subducting slabs hosted in highly anisotropic rock fabric: Nature Geoscience, **11**, no. 9, 696-700.

Lin, R., and L. Thomsen, 2019, Validation of Digital Rock Physics Algorithms: Minerals, **9**, no. 11, 669.

Lin, R., X. Fang, Y. Gan, and Y. Zheng, 2019, A damped dynamic finite difference approach for modeling static stress–strain fields: Pure and Applied Geophysics, **176**, no. 9, 3851-3865.

Liner, C. L., 2012, Elements of seismic dispersion: A somewhat practical guide to frequency-dependent phenomena: Society of Exploration Geophysicists.

Liu, H.-P., D. L. Anderson, and H. Kanamori, 1976, Velocity dispersion due to anelasticity; implications for seismology and mantle composition: Geophysical Journal International, **47**, no. 1, 41-58.

Liu, Q., S. Tian, G. Li, M. Sheng, X. Li, T. Wang, and Z. Shen, 2018, An analytical model for fracture initiation from radial lateral borehole: Journal of Petroleum Science Engineering, **164**, 206-218.

Liu, Y., X. Chang, D. Jin, R. He, H. Sun, and Y. Zheng, 2011, Reverse time migration of multiples for subsalt imaging: Geophysics, **76**, no. 5, WB209-WB216.

Liu, Y., X. Liu, A. Osen, Y. Shao, H. Hu, and Y. Zheng, 2016, Least-squares reverse time migration using controlled-order multiple reflections: Geophysics, **81**, no. 5, S347-S357.

Liu, Y. K., H. Hu, X. B. Xie, Y. C. Zheng, and P. Li, 2015, Reverse time migration of internal multiples for subsalt imaging: Geophysics, **80**, no. 5, S175-S185.

Love, A. E. H., 2013, A treatise on the mathematical theory of elasticity: Cambridge university press.

Lu, S., D. N. Whitmore, A. A. Valenciano, and N. Chemingui, 2015, Separated-wavefield imaging using primary and multiple energy: The Leading Edge, **34**, no. 7, 770-778.

Mainprice, D., G. Barruol, and W. B. Ismaïl. 2000, The seismic anisotropy of the Earth's mantle: from single crystal to polycrystal. American Geophysical Union.

Malcolm, A. E., B. Ursin, and M. V. de Hoop, 2009, Seismic imaging and illumination with internal multiples: Geophysical Journal International, **176**, no. 3, 847-864.

Malcolm, A. E., M. V. D. Hoop, and B. Ursin, 2011, Recursive imaging with multiply scattered waves using partial image regularization: A North Sea case study: Geophysics, **76**, no. 2, B33-B42.

Mavko, G., T. Mukerji, and J. Dvorkin, 2020, The rock physics handbook: Cambridge university press.

Mcmechan, G. A., 1983, Migration by Extrapolation of Time-Dependent Boundary-Values: Geophysical Prospecting, **31**, no. 3, 413-420.

Meng, C., 2017, Benchmarking Defmod, an open source FEM code for modeling episodic fault rupture: Computers Geosciences, **100**, 10-26.

Meng, C., and H. Wang, 2018, A finite element and finite difference mixed approach for modeling fault rupture and ground motion: Computers Geosciences, **113**, 54-69.

Moczo, P., J. Kristek, M. Galis, and P. Pazak, 2010, On accuracy of the finite-difference and finite-element schemes with respect to P-wave to S-wave speed ratio: Geophysical Journal International, **182**, no. 1, 493-510.

Morse, P. M., and H. Feshbach, 1954, Methods of theoretical physics: American Journal of Physics, **22**, no. 6, 410-413.

Oristaglio, M., 2016, SEAM update: Integrated reservoir and geophysical modeling: SEAM Time Lapse and SEAM Life of Field: The Leading Edge, **35**, no. 10, 912-915.

Paffenholz, J., B. McLain, J. Zaske, and P. J. Keliher, 2002, Subsalt multiple attenuation and imaging: Observations from the Sigsbee2B synthetic dataset, SEG Technical Program Expanded Abstracts 2002: Society of Exploration Geophysicists, 2122-2125.

Raymer, L., E. Hunt, and J. S. Gardner. 1980, An improved sonic transit time-to-porosity transform. Paper read at SPWLA 21st annual logging symposium.

Reddy, J., 2004, An introduction to the finite element method. Vol. 1221: McGraw-Hill New York.

Saenger, E., S. Shapiro, and Y. Keehm, 2005, Seismic effects of viscous Biot - coupling: Finite difference simulations on micro - scale: Geophysical Research Letters, **32**, no. 14.

Saenger, E. H., N. Gold, and S. A. Shapiro, 2000, Modeling the propagation of elastic waves using a modified finite-difference grid: Wave motion, **31**, no. 1, 77-92.

Saenger, E. H., O. S. Krüger, and S. A. Shapiro, 2006, Effective Elastic Properties of Fractured Rocks: Dynamic vs. Static Considerations: International Journal of Fracture, **139**, no. 3-4, 569-576.

Saxena, N., and G. Mavko, 2016, Estimating elastic moduli of rocks from thin sections: Digital rock study of 3D properties from 2D images: Computers Geosciences, **88**, 9-21.

Schuster, G. T., 2017, Seismic inversion: Society of Exploration Geophysicists.

Seton, M., R. Müller, S. Zahirovic, C. Gaina, T. Torsvik, G. Shephard, A. Talsma, M. Gurnis, M. Turner, and S. Maus, 2012, Global continental and ocean basin reconstructions since 200 Ma: Earth-Science Reviews, **113**, no. 3-4, 212-270.

Shirey, S. B., and S. H. Richardson, 2011, Start of the Wilson cycle at 3 Ga shown by diamonds from subcontinental mantle: Science, **333**, no. 6041, 434-436.

Solopova, N. A., L. Dubrovinsky, A. V. Spivak, Y. A. Litvin, and N. Dubrovinskaia, 2015, Melting and decomposition of MgCO3 at pressures up to 84 GPa: Physics and Chemistry of Minerals, **42**, 73.

Stern, R. J., M. I. Leybourne, and T. Tsujimori, 2016, Kimberlites and the start of plate tectonics: Geology, **44**, no. 10, 799-802.

Tan, S. R., and L. J. Huang, 2014, Least-squares reverse-time migration with a wavefield-separation imaging condition and updated source wavefields: Geophysics, **79**, no. 5, S195-S205.

Thomsen, L., 1986, Weak elastic anisotropy: Geophysics, **51**, no. 10, 1954-1966.

Thomsen, L., 1995, Elastic anisotropy due to aligned cracks in porous rock1: Geophysical Prospecting, **43**, no. 6, 805-829.

Thomson, A. R., M. J. Walter, S. C. Kohn, and R. A. Brooker, 2016, Slab melting as a barrier to deep carbon subduction: Nature, **529**, 76.

Udias, A., and E. Buforn, 2017, Principles of seismology: Cambridge University Press.

Virieux, J., 1984, SH-wave propagation in heterogeneous media: Velocity-stress finite-difference method: Geophysics, **49**, no. 11, 1933-1942.

Virieux, J., 1986a, P-SV wave propagation in heterogeneous media: Velocity-stress finite-difference method: Geophysics, **51**, no. 4, 889-901.

Virieux, J., 1986b, P-SV-WAVE PROPAGATION IN HETEROGENEOUS MEDIA - VELOCITY-STRESS FINITE-DIFFERENCE METHOD: Geophysics, **51**, no. 4, 889-901.

Whitmore, N. D., 1984, Iterative Depth Migration by Backward Time Propagation: Geophysics, **49**, no. 5, 640-640.

Xu, C., J. Kynický, W. Song, R. Tao, Z. Lü, Y. Li, Y. Yang, M. Pohanka, M. V. Galiova, L. Zhang, and Y. Fei, 2018, Cold deep subduction recorded by remnants of a Paleoproterozoic carbonated slab: Nature Communications, **9**, 2790.

Yang, J., Z. Mao, J.-F. Lin, and V. B. Prakapenka, 2014, Single-crystal elasticity of the deep-mantle magnesite at high pressure and temperature: Earth and Planetary Science Letters, **392**, 292-299.

Yao, C., Z. Wu, F. Zou, and W. Sun, 2018, Thermodynamic and Elastic Properties of Magnesite at Mantle Conditions: First-Principles Calculations: Geochemistry, Geophysics, Geosystems, **19**, 2719.